ABSTRACT

KENT, LAURA MICHELLE. Multi-Year Analysis of Ice Streamers within Coastal Northeast US Winter Storms. (Under the direction of Dr. Sandra Yuter).

Many radar observational studies have examined 1-3 km scale convectively-overturning generating cells in winter storms which yield locally higher snowfall rates. But previous work has not quantified their frequency occurrence or diurnal cycle. Recent idealized modeling studies suggest that the primary forcing mechanism for generating cell maintenance is cloud-top destabilization from radiative instability which implies that generating cells will be more common during the night than during the day. As a proxy for generating cells, we use precipitation radar detectable ice streamers (ice trails from generating cells) which are sometimes referred to as fall streaks.

This study utilizes vertically-pointing radar data from a 24.1 GHz Micro Rain Radar in Stony Brook, NY to characterize the prevalence of ice streamers. This coastal northeast U.S. data set spans nearly 15,000 hours of radar echo obtained over 10 winter seasons (November - March from 2007-2018). We developed an image processing algorithm which identifies ice streamers as vertically continuous features of locally higher reflectivity compared to a smoothed background reflectivity. Ice streamers occur about 80% of the time in winter storms at Stony Brook, NY. Since the Micro Rain Radar detects precipitation particles but not cloud particles, the estimated average ice streamer occurrence of 80% is likely an underestimate.

We tested whether a diurnal cycle was present in the hourly frequency of occurrence of ice streamers using Monte Carlo 95th percentile significance tests on several metrics of the time series, harmonic fits and the differences between 6-hour averages. There was weak evidence for a diurnal cycle peaking in the hours spanning sunrise. However, the small amplitude of the diurnal cycle is sufficiently low to likely be of marginal practical significance and its timing is inconsistent with what one would expect from an overnight radiative instability.

Multi-Year Analysis of Ice Streamers within Coastal Northeast US Winter Storms

by
Laura Michelle Kent

A thesis submitted to the Graduate Faculty of
North Carolina State University
in partial fulfillment of the
requirements for the Degree of
Master of Science

Marine, Earth, and Atmospheric Science

Raleigh, North Carolina
2021

APPROVED BY:

Dr. Matthew Parker

Dr. L. Baker Perry

Dr. Sandra Yuter
Chair of Advisory Committee

ACKNOWLEDGEMENTS

I would like to thank my advisor, Dr. Sandra Yuter for the endless support and motivation she has given me the past two years. Her mentorship has been invaluable, especially during the remote work scenario we suddenly found ourselves within. Thank you as well to my committee members: Dr. Matthew Parker and Dr. L. Baker Perry for their feedback and discussions regarding my thesis. Thank you to Laura Tomkins and Dr. Matthew Miller for providing constructive discussion and helpful comments from the very beginning of this project. Thank you to my research group members for technical support and being amazing people to work with. I would like to also thank my friends and family for their support. Lastly, I would like to thank my dog for always listening when I talked through code problems.

TABLE OF CONTENTS

LIST OF TABLES

LIST OF FIGURES

CHAPTER

1

INTRODUCTION

The northeastern United States usually experiences several large winter storms each year which have severe impacts on densely populated metropolitan areas. Significant snowfall can shut down airports and roadways. FEMA declared 520 emergency declarations from 1955 to 2020 and of those 165 were for winter related hazards (Federal Emergency Management Agency 2021). Snowfall rates can vary widely within winter storms (e.g. Rasmussen et al. 2003). The physical processes and associated environments responsible for locally heavy snowfall are not fully understood, and hence accurate snow accumulations are difficult to forecast.

Northeast US winter storms are extratropical cyclones with well-studied synoptic and mesoscale processes that yield and modulate precipitation (e.g. Schultz et al. 2019). Superimposed on these larger-scale processes, convective-scale overturning cells near cloud top have localized upward motions which are conducive to ice growth (Houze et al. 1981; Matejka et al. 1980; Herzegh and Hobbs 1980; Crosier et al. 2014; Evans et al. 2005; Plummer et al. 2014). Previous work disagrees on the most important sources of the instability that are responsible for cellular motions near cloud top and the resulting locally higher snowfall at the surface. The processes and environments that initiate and sustain cloud top convective cells within winter storms are one piece in the puzzle in understanding and eventually improving forecasting of these storms. This study focuses on multi-year radar observations of the convective cells near cloud top and associated ice streamers from a vertically-pointing radar located in Stony Brook, NY on Long Island.

1.1 Definitions

The AMS Glossary defines a *generating cell* as follows.

> "In radar, a small region of locally high reflectivity from which a trail of hydrometeors originates. It is postulated that snow crystals are formed and grow in the generating cells and that the cells are maintained by convection induced by the release of latent heat accompanying the crystal growth. The shape of the snow trail below a generating cell depends on the fall speed of the snow and the vertical profile of the horizontal wind."

Trails of higher reflectivities that originate in the upper or middle portions of snow echo and descend within storms are often referred to as *fallstreaks* (Marshall 1953; Gunn et al. 1954; Douglas et al. 1957; Rauber et al. 2014; Rosenow et al. 2014; Plummer et al. 2015; Keeler et al. 2016b). However, in addition to this historical use of fallstreak it is also used as a synonym for virga, liquid or solid precipitation that does not reach the ground (American Meteorological Society 2021). To reduce ambiguity, in this paper, we use the term *ice streamer* following Wexler (1955) and Wexler and Atlas (1959). We use the modifier *ice* to distinguish from streamers in rain. The AMS Glossary indicates that *streamers*

> "emerge from a layer of convective instability that often exists in the middle or upper troposphere in widespread storms. Small convective cells developing within this layer produce the ice crystals that then fall to lower altitudes. The base of the convectively unstable layer is called the snow-generating level. The shape and vertical extent of the streamers depend on the vertical profiles of wind and relative humidity in the layer through which the precipitation falls."

Generating cells yield precipitation-sized ice particles for a finite time. As the precipitation particles fall out of the generating cells they are advected by winds within the storm (Fig. 1.1). The top of the ice streamer is within the generating cell. Differences in wind direction and wind speed among layers of the storm bend the trail of falling particles such that the geographic location where the particles reach the surface is offset from the location of the generating cell. In winter storms, wind speeds usually increase with increasing height and wind direction can abruptly change with height. As a result of wind shear within the storm, ice streamers are often three-dimensional.

For example, Figure 1.2 , illustrates a RHI vertical cross-section through a winter storm at 0509 UTC on 1 February 2021 scanned by a research radar operated by Stony Brook University. The wind direction changes abruptly at 3.5 km altitude and 2 km altitude. The ice streamer shape bends as particles are advected by the wind in different layers as the particles fall. Earlier in the same storm, the upper portions of the ice streamers are distinct but lower portions are more smeared out across several layers with different wind directions (Fig. 1.3)

Time-height data from surface-based vertically-pointing radar effectively samples along a streamline based on the mean storm motion relative to the radar's location adding a further complication to the visual appearance of ice streamers compared to vertical cross-sections from scanning radar RHIs and airborne radar data. Figure 1.4 shows the location of Stony Brook, NY relative to the cyclone low pressure center for over a dozen storms. The MRR has insufficient sensitivity to observe non-precipitating portions of the cloud. The upper portions of the overturning circulation that is part of the generating cell may or may not contain precipitation-sized ice. Hence, the MRR will typically underestimate the vertical extent of the generating cell portion of the ice streamer. Given that precipitation ice fall speeds are usually ~1 m/s and echo tops at Stony Brook are rarely higher than 8 km altitude, it would be unusual for an ice streamer to have duration in time-height data longer than 2 hours.

1.2 Previous Work

1.2.1 Characteristics of Generating Cells and Ice Streamers

Marshall (1953) first discussed generating cells based on observations of scanning X-Band radar data. Using scanned radar RHIs, he identified the generating cell level as the altitude in which precipitation develops, and described "mares tails" appearing below that level. The pattern of precipitation trails that he describes is shown in Fig. 1.5. Further radar studies during the 1950s described the basic structures and evolution of generating cells and the environment in which they develop (Gunn et al. 1954; Wexler 1955; Langleben 1956; Douglas et al. 1957; Wexler and Atlas 1959). The radar-observed structure of generating cells transitions from cells without trails, cells with trails, and finally trails without heads. These early investigators focused on two key sources of instability responsible for formation of generating cells near cloud top: advection of dry air aloft (potential instability) and cloud-top radiative cooling.

Subsequent research has expanded and refined these early findings. Multiple radar studies concur that generating cells are typically 1-3 km in the vertical and horizontal extent and contain updrafts of 1-2 m s^{-1}. (e.g. Gunn et al. 1954; Langleben 1956; Wexler and Atlas 1959; Syrett et al. 1995; Evans et al. 2005; Kumjian et al. 2014; Plummer et al. 2014; Rosenow et al. 2014; Rauber et al. 2015). Kumjian et al. (2014) examined high spatial and time resolution radar data from winter storms in the Colorado Front Range and found that individual generating cells had a lifetime of about 10 minutes.

The observation of locally higher radar reflectivity defines generating cells from the surrounding lower reflectivity background. Reflectivity values alone are insufficient to determine mode of ice growth since reflectivity in snow is a function of the size distribution, density distribution, and number concentration of particles within a volume of air. The clearest evidence for the nature of ice growth within generating cells comes from the aircraft data analysis of Plummer et al. (2014) which sorted data obtained within and between generating cells observed in the comma head of 11 continental winter cyclones (Fig. 1.6). In contrast to previous work, Plummer et al. (2014) used particle probes designed to reduce ice particle shattering and accounted for residual particle shattering in their analysis. At a given temperature, similar ice crystal habits were observed within and between generating cells. Riming and aggregation were observed within and and between generating cells. While there was considerable overlap between the particle characteristic distributions obtained within and between generating cells (Fig. 1.7), there was a consistent signature of higher values within generating cells for temperatures less than -18°C. The higher values of ice water contents are primarily a result of increased number concentration of particles > 500 μm which were on average between 1.7 and 3.3 times higher inside as compared to outside of generating cells. Supercooled water was directly observed in 26% of observations within generating cells as compared to 18% between generating cells. As expected, overall smaller number concentrations and particle diameters were present at lower air temperatures and overall higher turbulence within the generating cell layer lessened the differences within and between generating cells.

In summary, a generating cell is an overturning circulation initiated by an instability near cloud top. The upward branch of the circulation yields a localized increase in RH which will result in ice mass increases when RH_{ice} > 100%. If the ice crystals within the generating cell grow enough to reach precipitation-size and fall, the resulting stream of particles sedimenting below the overturning circulation is observable by radar.

1.2.2 Different Sources of Instability within the Generating Cell Layer

The relative importance of various sources of instability to the overturning circulations within generating cells has been debated in the literature since the 1950s. Early work found that generating cells were often associated with sounding-observed potential instability, especially along boundaries from moist to dry air which require only small vertical motions for instability to be released (Wexler and Atlas 1959). Other early observational work demonstrated that generating cells could form in stable layers and yielded an alternate theory that diabatic heating from latent heat release during depositional growth was sufficient to maintain instability (Douglas et al. 1957; Gunn et al. 1954). More recently, observational analysis by Kumjian et al. (2014) consistently found potential instability near cloud top when generating cells were present (Fig. 1.8). They speculated that a combination of diabatic heating and cloud-top radiation instability yielded the potential instability in the layer with generating cells and played a role in maintaining generating cells in addition to the advection of lower θ_e (dryer and/or cooler) air above the cloud layer. Kumjian et al. (2014) were unable to unravel the relative roles of these sources of instability since observational studies cannot simply turn on and off physical processes.

Modeling is required to test the sensitivity of generating cell characteristics to radiative forcing and diabatic heating in the context of a range of stability and shear conditions. A comprehensive set of idealized mesoscale model simulations of a region within the comma-head of an extratropical cyclone are described in a three-part series of papers by Keeler et al. (Keeler et al. 2016a,b, 2017). They simplified the environment of a storm on 14-15 February 2010 which had aircraft radar observed generating cells near cloud top (Rauber et al. 2014; Rosenow et al. 2014; Plummer et al. 2014, 2015). They examined the influences of radiation (nighttime-longwave only, daytime longwave + shortwave, and no radiation) (Keeler et al. 2016a), stability (potential instability, neutral, and stable) (Keeler et al. 2016b) and wind shear within the generating cell layer (Keeler et al. 2017) on generating cell organization, vertical velocities and ice water contents. Their idealized WRF simulations used a 50.1 x 50.1 x 15 km^3 grid with horizontal grid spacing of 100 m and vertical spacing near 50 m at the generating cell level of 6-8 km altitude. Figure 1.9 shows vertical cross-sections of precipitation ice mixing ratio and vertical air motion through generating cells from their nighttime radiation simulation with strong potential instability and moderate wind shear (4 ms^{-1} km^{-1}). As expected, generating cells developed within the simulation in the presence of near cloud-top potential instability. Generating cells did not develop in neutral and stable conditions when longwave cooling was not present. Generating cells persisted through the day in the simulations with radiation as shortwave warming was not sufficient to fully offset longwave cooling. Daytime shortwave warming did decrease the range of vertical air motions within the generating cells compared to at night. Contradicting the AMS Glossary definition of generating cells in Section 1.1, they found that latent heat release related to depositional growth of ice crystals was not sufficient to *maintain* generating cells near cloud top in the absence of radiative forcing. As wind shear increased from no wind shear, to moderate (4 m s^{-1} km^{-1}), to strong wind shear (10 m s^{-1} km^{-1}), the horizontal pattern of generating cells changed from cellular to linear streets to less coherent linear structures (Fig. 1.10 and 1.11).

Comparison of the nighttime and daytime radiation runs showed that generating cell updrafts were stronger and ice precipitation mixing ratios were higher in nighttime-longwave only simulations as compared to daytime longwave+shortwave simulations (Fig. 1.10 and 1.11). Simulation steady state values for median vertical air motions within generating cells were 1.64 m/s with night-longwave only radiation compared to 1.19 m/s with day-longwave+shortware radiation (Keeler et al. 2017). Within generating cells, ice precipitation mixing ratios were often > 0.15 g kg^{-1} both day and night. There were higher maxima in mixing ratios at night (∼0.3 g kg^{-1}) as compared to during the day (∼0.2 g kg^{-1}) (Keeler et al. 2016a). These higher values at night are related to the stronger destabilization of cloud top by longwave cooling (negative buoyancy) as compared to during the day when it is partially offset by shortwave warming. The role of longwave cooling yielding negatively buoyant parcels that trigger a layer of overturning convection is roughly analogous to liquid-phase cloud-top convection which yields drizzle cells in marine stratocumulus (Wood et al. 2011).

1.3 Research Goals

A key implication from the Keeler et al. papers is that generating cells with higher vertical velocity values yielding high ice water contents will be more frequent at night. These characteristics are expected to manifest as higher frequencies of radar reflectivity detectable ice streamers overnight compared to during the day. There is a non-linear relationship between mixing ratio and reflectivity making higher mixing ratios much easier to detect with weather radar data. Radar reflectivity in snow is roughly proportional to $\log_{10}(\text{precipitation ice mixing ratio})^3$ (Matrosov 2007). Synoptic storm structures and environmental stability conditions are not expected to have a diurnal cycle over a large sample size of winter storms.

Despite the many observational studies over the decades, no one to date has systematically quantified the overall occurrence of generating cells within winter storms or if there is a diurnal cycle in their frequency. We use 10 winter seasons of vertically-pointing radar data from Stony Brook, NY to identify ice streamers and analyze their frequency occurrence relative to time of day. These data correspond to 14,877 hours with radar echo which is the equivalent of almost 620 days. Previous observational work related to winter storm generating cells used data sets from short term field projects and storm sample sizes less than 20.

The testable hypothesis that was stated in the NSF grant proposal that funded this work is as follows:

> Convective scale generating cells (with active overturning circulations) within 500 m of cloud top are 2x more common at night when a cloud top radiative cooling instability is present than during the day.

In this analysis, we use ice streamer counts per hour as a proxy for generating cells. The longer duration of ice streamers as compared to the source generating cells makes them easier to observe in vertically-pointing radar data. Hence the original testable hypothesis for this analysis was rephrased as:

> Ice streamers observed by vertically-pointing radar data are 2x more common at night than during the day.

This hypothesis assumes that ice streamers have a low enough prevalence that a 2x frequency during the night compared to day is possible (i.e. that daytime frequency of occurrence of ice streamers was less than 50%). As the analysis proceeded, it turned out that the average prevalence of ice streamers was close to 70%, much higher than was thought when the proposal was written. We ended up modifying the testable hypothesis for this thesis to look for a diurnal cycle of practical significance. Chapter 2 describes the radar data set, how ice streamers are detected and characterized, and the methods used to determine if there is a practically significant variation in ice streamer frequency by time of day. Chapter 3 presents the information on the sensitivity of the detection method and analysis results, and Chapter 4 summarizes the findings and discusses future work.

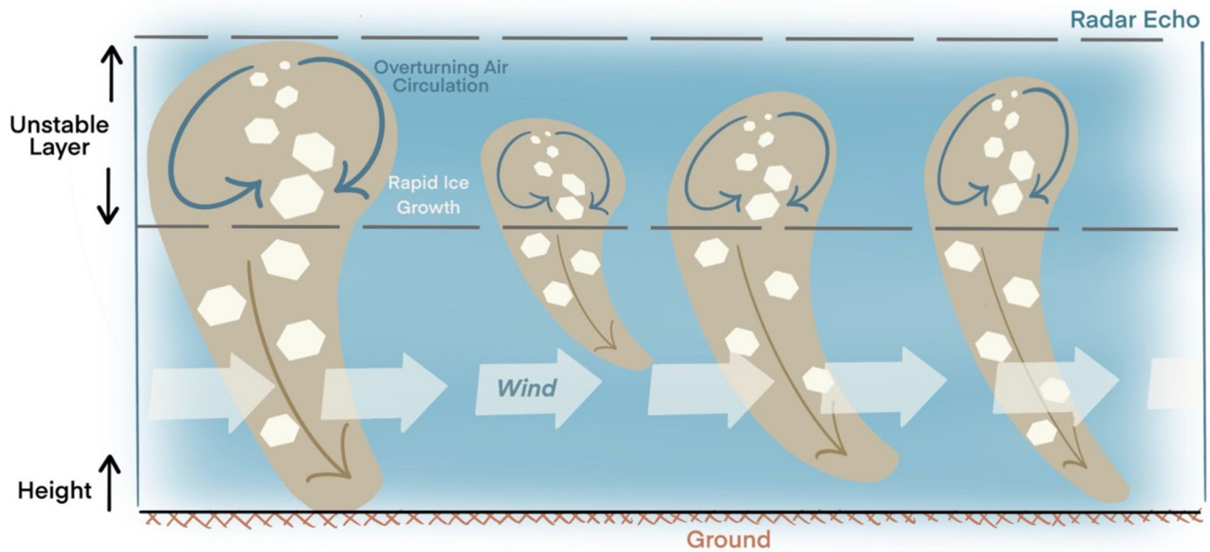

Figure 1.1: Idealized depiction of ice streamers in a time height plot. The brown ice streamers have an increased size in the unstable layer where the overturning air circulations promote ice crystal growth, white hexagons. As the ice crystals fall below the unstable layer they are advected with the wind which results in the ice streamers having the skewed appearance.

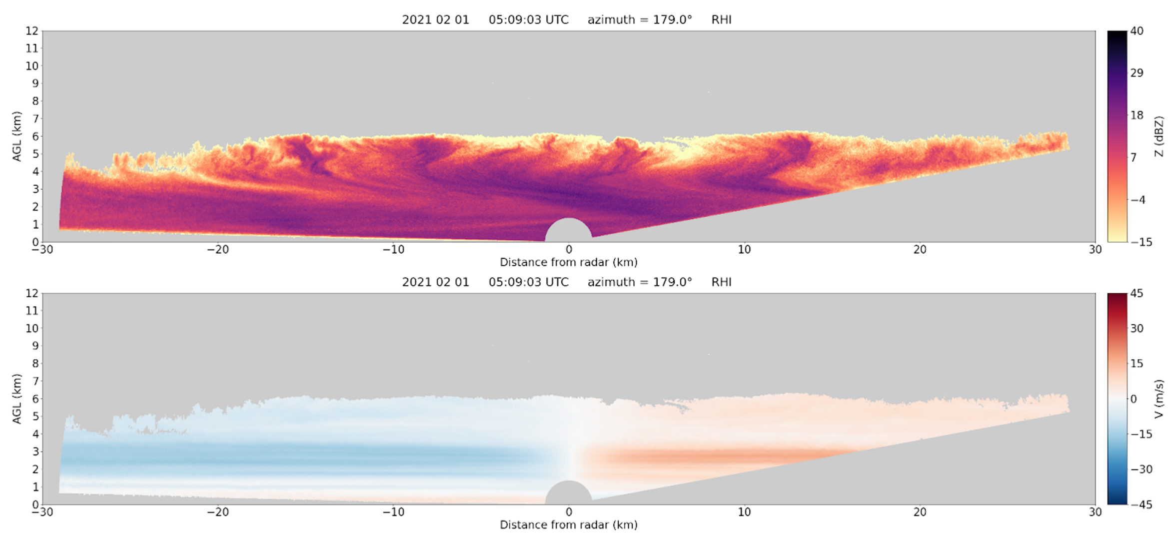

Figure 1.2: A vertical RHI cross-section from 01 February 2021 from KASPR research radar at Stony Brook University. The ice streamers in this image have a sharp bend at 3.5 km and 2 km where there is a sharp wind change and the advected particles abruptly change direction as well.

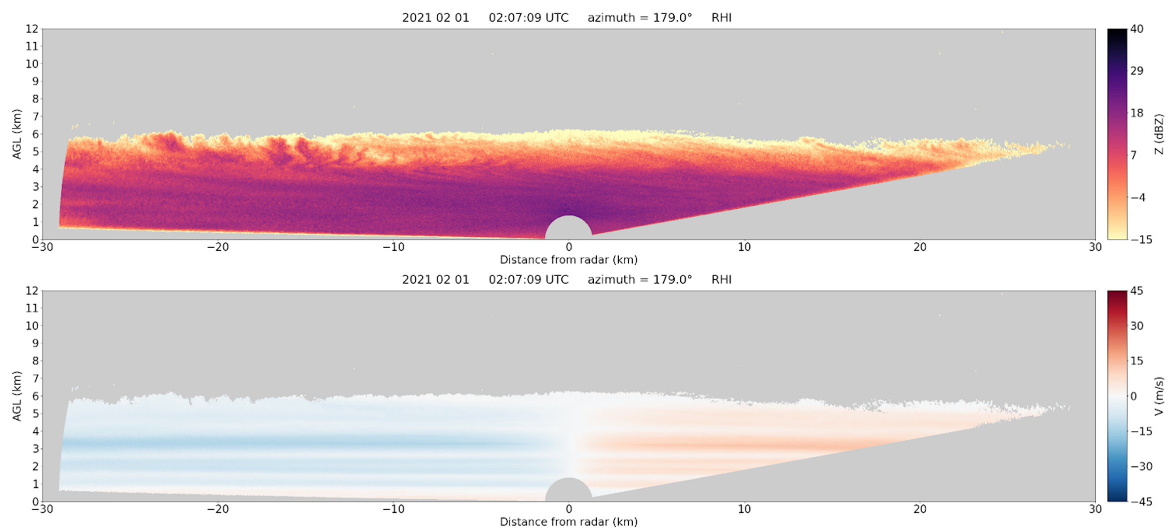

Figure 1.3: A vertical RHI cross-section from 01 February 2021 from KASPR research radar at Stony Brook University. The ice streamers in this image are distinct above 4 km, but the particles become smeared across several layers as the wind direction become less distinct in the lower levels.

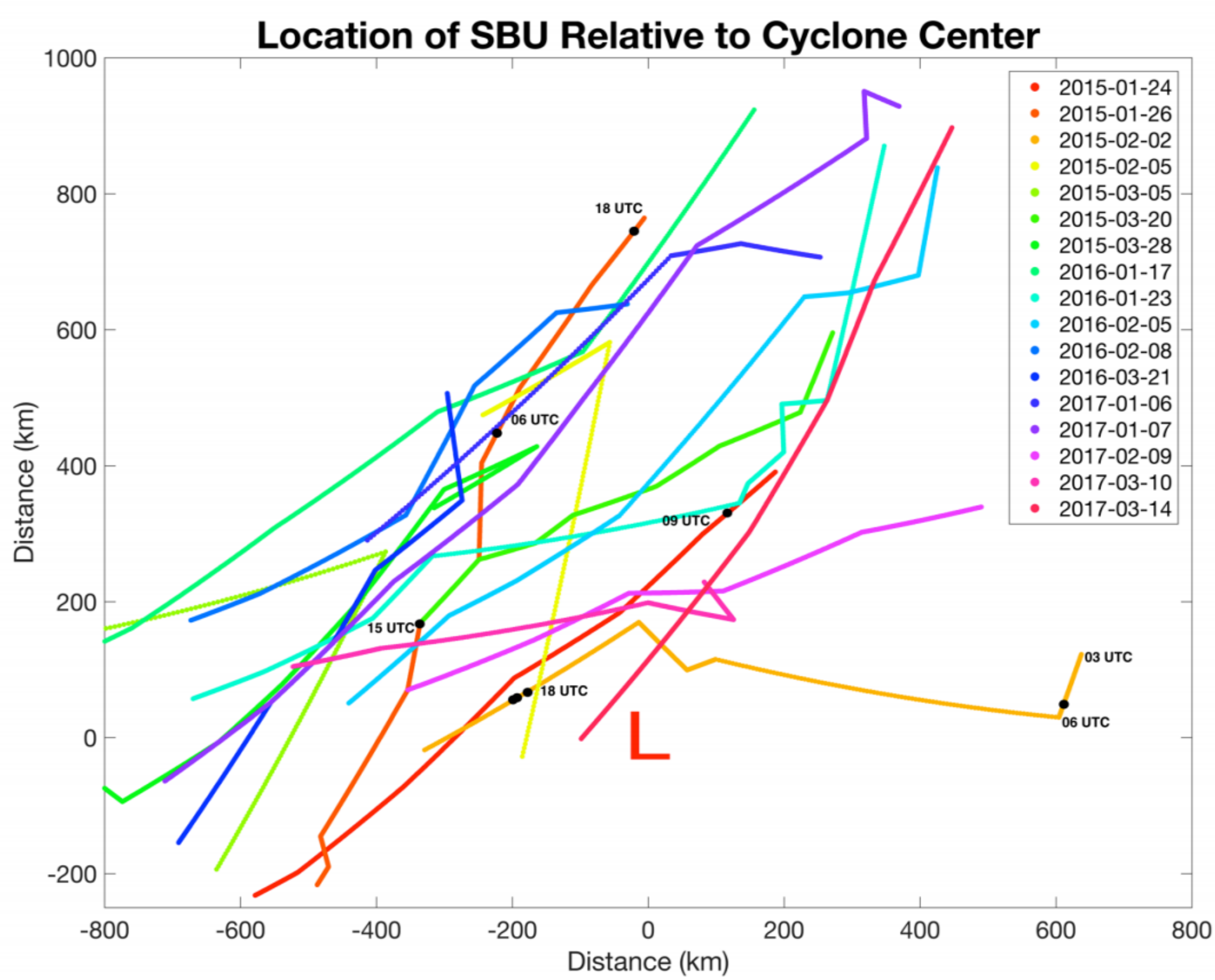

Figure 1.4: Locations of measurements at Stony Brook University relative to the low pressure for 17 storms. UTC hour represents nearest 3-hourly time. Figure courtesy of Levi Lovell.

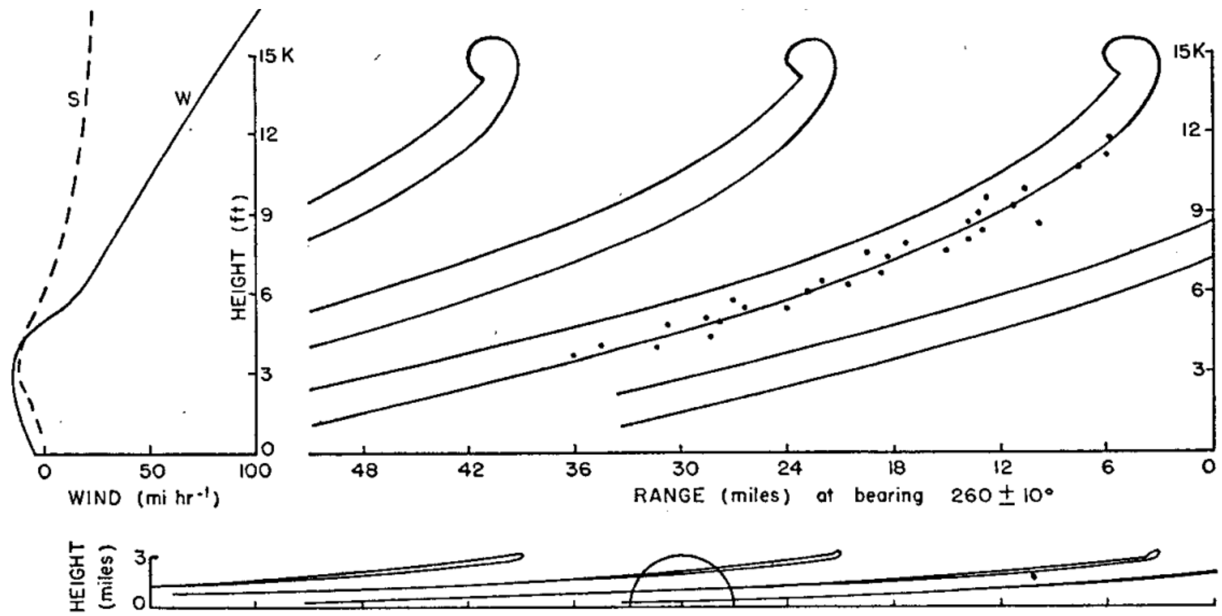

Figure 1.5: Height/range data from 6 ice streamers from a single generating cell are plotted on the main diagram. At the bottom of the figure, ice streamers are shown against equal vertical and horizontal scales. Figure 3 from Marshall (1953)

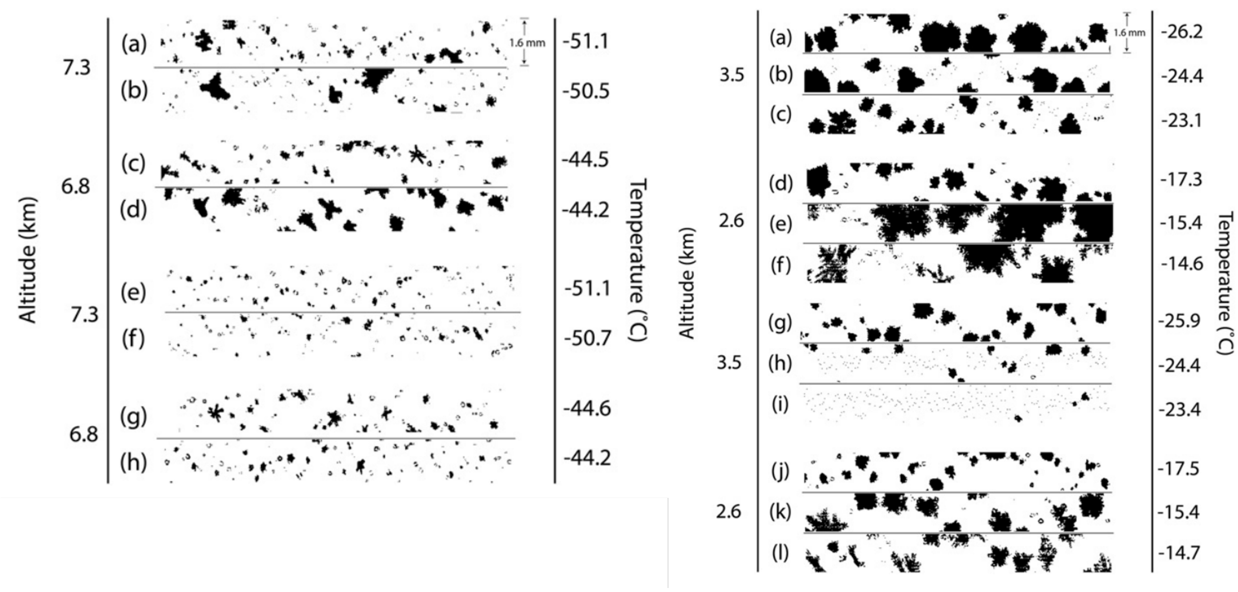

Figure 1.6: Shown are 2D-C shadow images from generating cell regions sampled during a 15 February 2010 research flight, relative to altitude and air temperature. Left and right image taken along different flight segments. Left image (a)-(d) Measurements within generating cell cores and (e)-(h) measurements at Z_e minima between generating cells. Right image (a)-(f) Measurements within generating cell cores and (g)-(l) measurements at Z_e minima between generating cells. Figs 7 and 10 from Plummer et al. (2014)

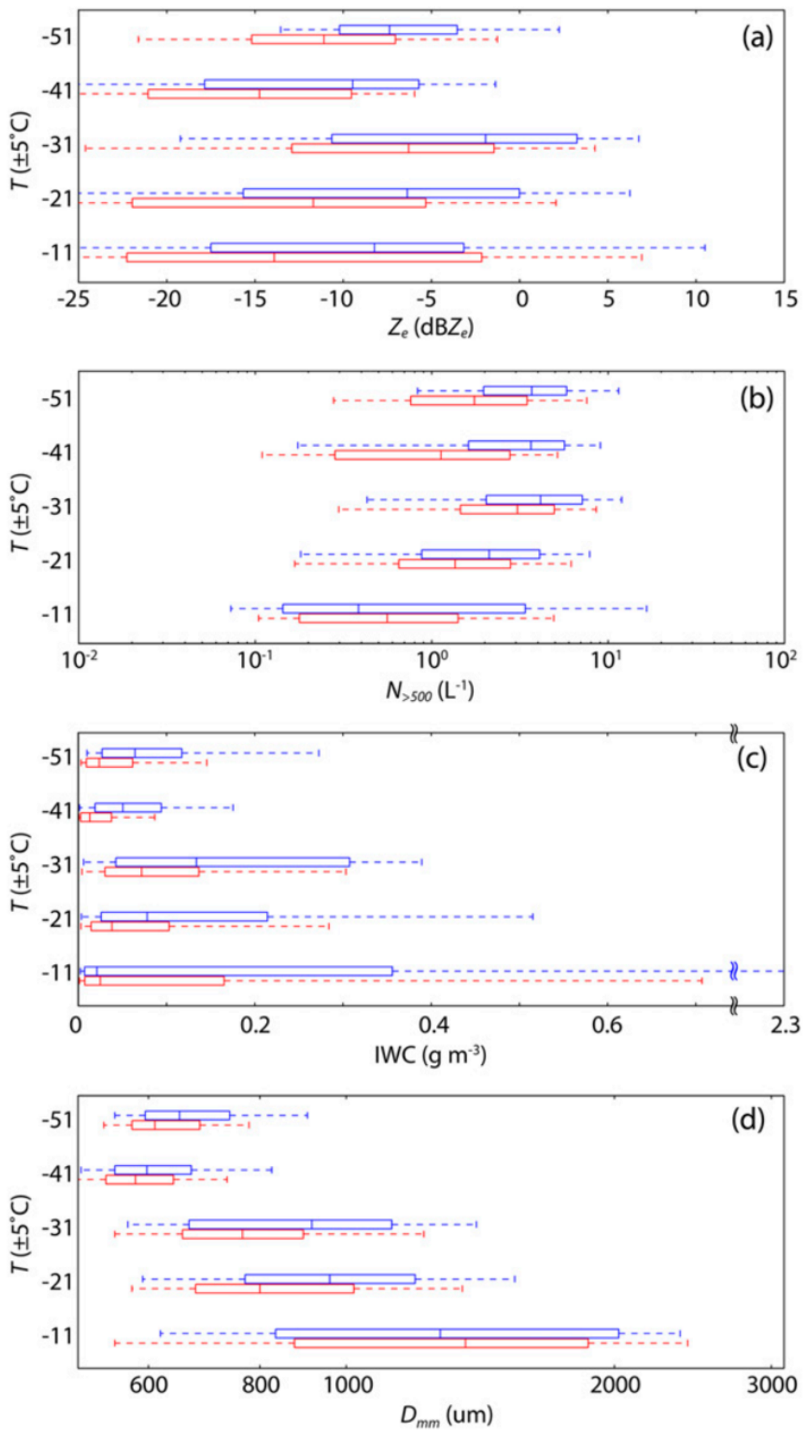

Figure 1.7: Median and 5^{th}, 25^{th}, 75^{th}, and 95^{th} percentiles for (a) Z_e (b) $N_{>500}$ (c) ICWC, and (d) D_{mm} in 10° C intervals.Measurements from a research flight completed on 15 February 2010 at flight legs 7.3, 6.8, 3.5, and 2.6 km altitude. Measurements within generating cell cores are in blue, red represents measurements between generating cells. from Plummer et al. (2014)

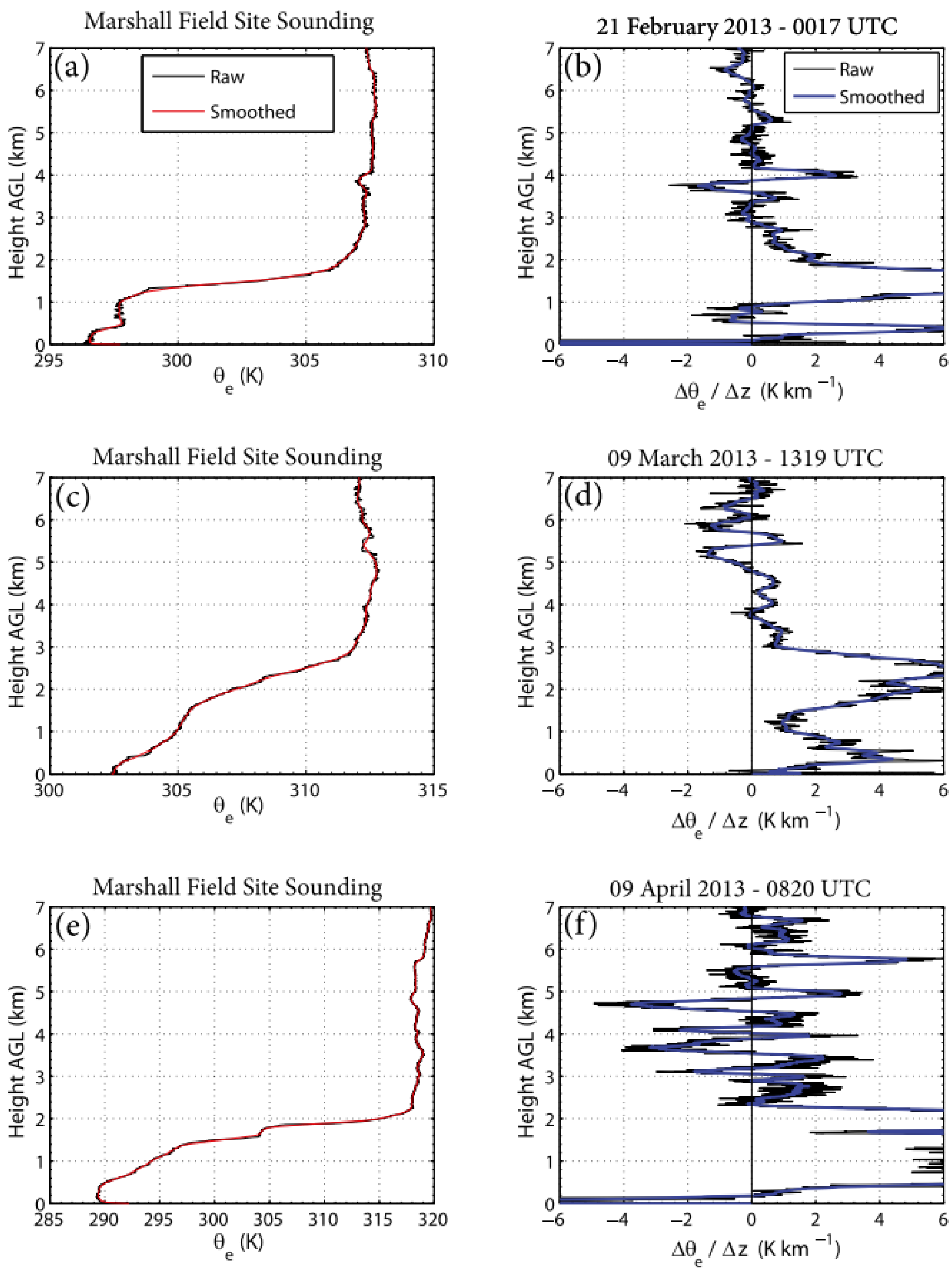

Figure 1.8: (left) Raw (black lines) and smoothed (red lines) vertical profiles of θ_e and (right) raw (black lines) and smoothed (blue lines) vertical profiles of the vertical gradient of θ_e for three soundings at Marshall Field Site in Colorado (a),(b) 0017 UTC 21 Feb 2013, (c),(d) 1319 UTC 9 Mar 2013 and (e),(f) 0820 UTC 9 Apr 2013 from Kumjian et al. (2014)

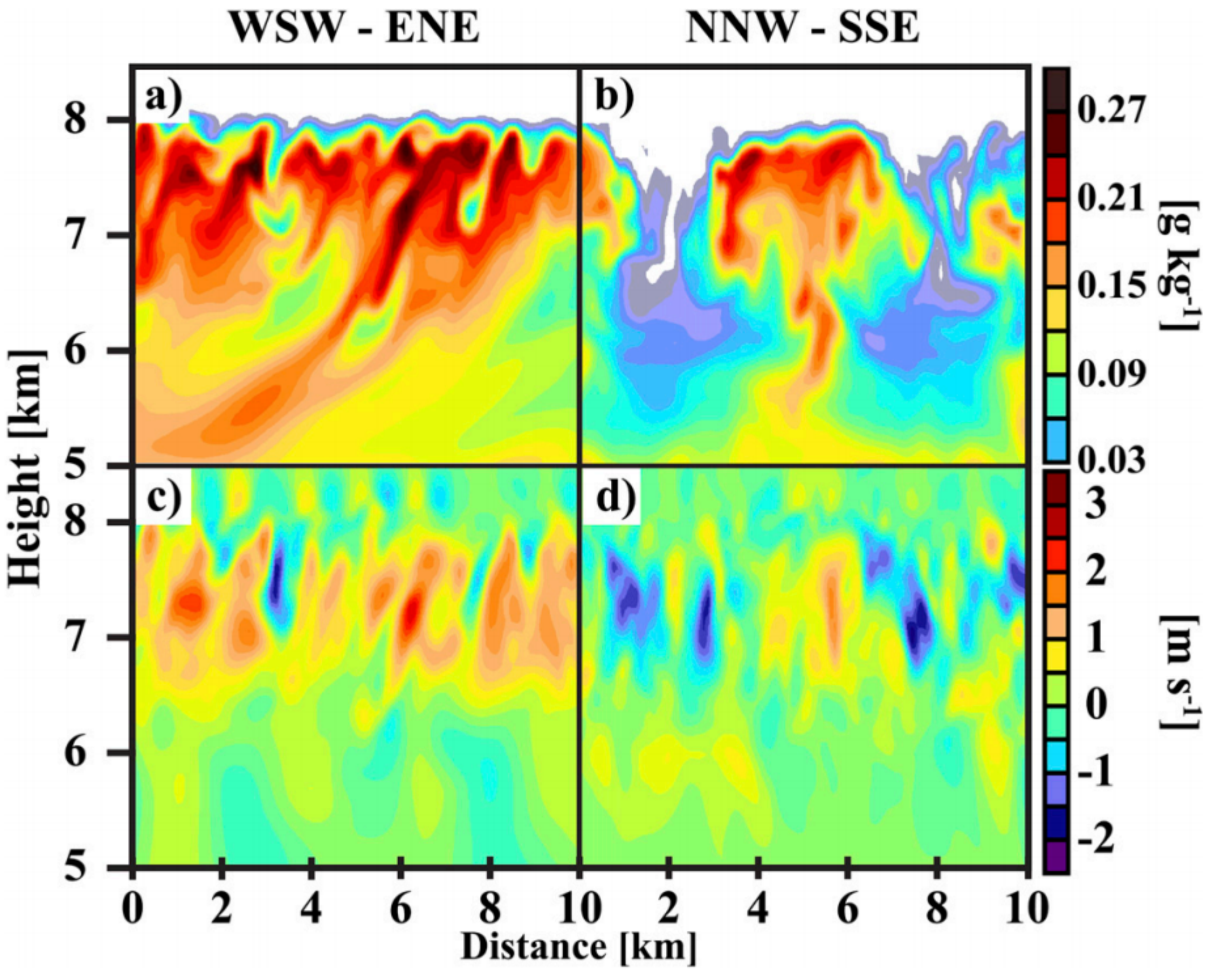

Figure 1.9: Perpendicular cross-sections of (a),(b)precipitation ice mixing ratio and (c),(d) vertical air motion through generating cells from their nighttime radiation simulation with strong potential instability and moderate wind shear (4 ms^{-1} km^{-1}) from Keeler et al. (2017)

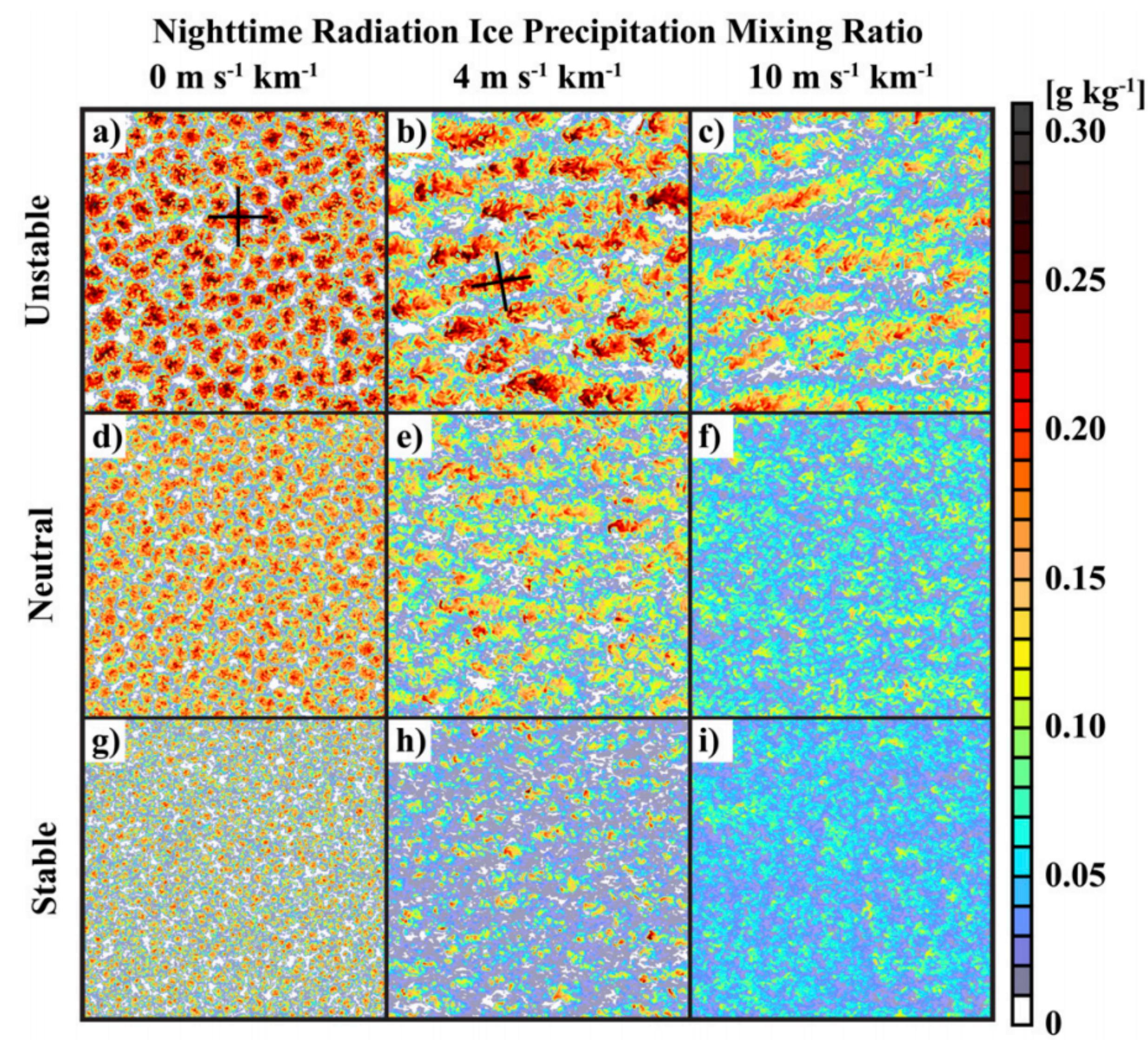

Figure 1.10: Ice precipitation mixing ratio at 7.5 km at t=180 min in the nighttime radiation simulations for the total horizontal extent of their model domain. Rows correspond to stability profiles and columns to the u shear. Figure from Keeler et al. (2017)

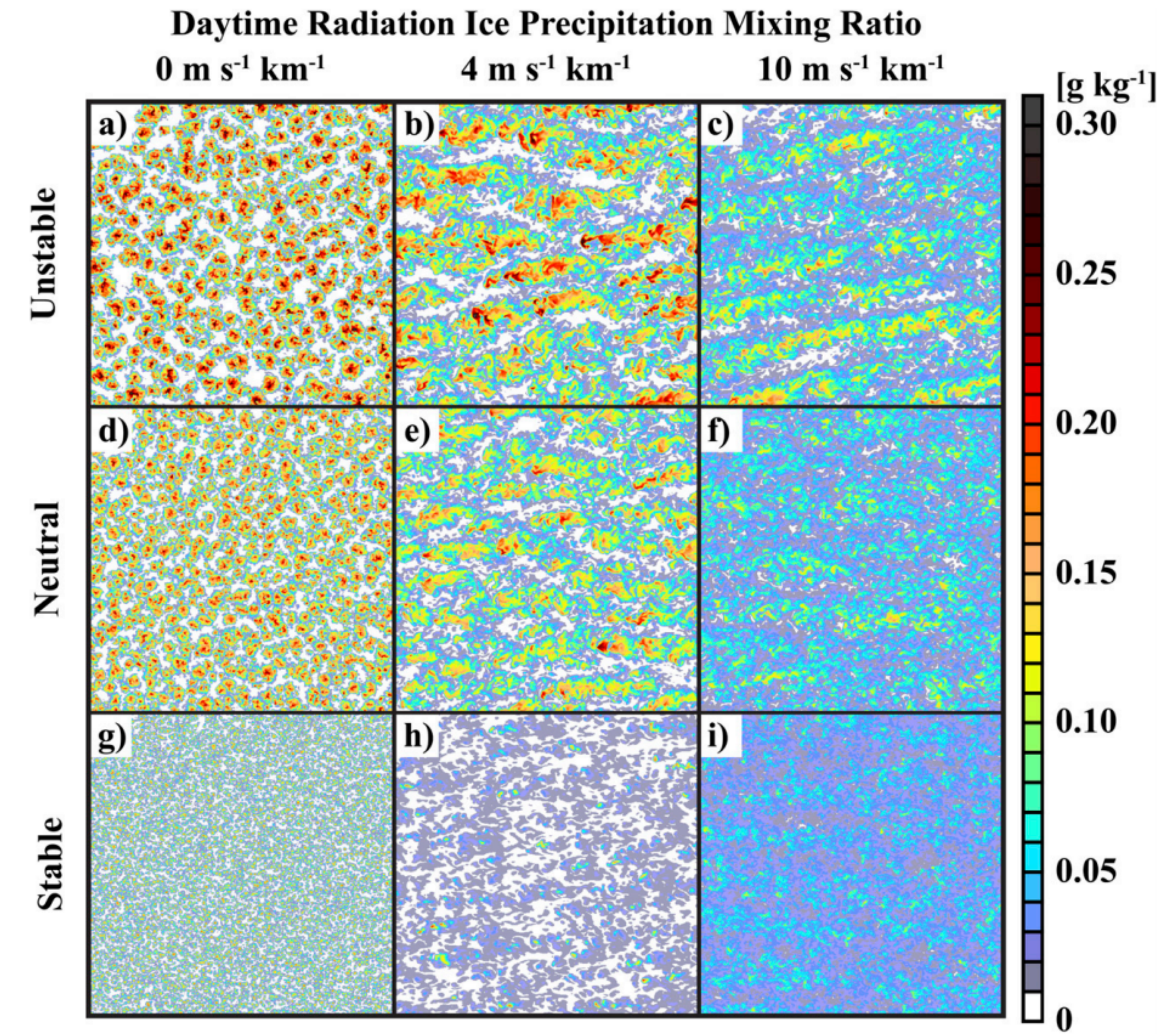

Figure 1.11: Ice precipitation mixing ratio at 7.5 km at t=180 min in the daytime radiation simulations for the total horizontal extent of their model domain. Rows correspond to stability profiles and columns to the u shear (weak, moderate and strong). Figure from Keeler et al. (2017)

CHAPTER

2

DATA AND METHODS

2.1 Data Sets

2.1.1 Vertically-Pointing Radar

Reflectivity and Doppler velocity data from a vertically-pointing K-band Micro Rain Radar (MRR-2) with a 2° beamwidth offset antenna (Peters et al. 2005) located at Stony Brook, NY on Long Island are used to identify ice streamers within winter storms. Data from a vertically-pointing radar is in a time-height format. The plots with time on the x-axis and height on the y-axis represent a collection of samples in a column over the radar at regularly spaced intervals in time.

The MRR has a sensitivity of approximately -2 dBZ at 1 km altitude (METEK 2017) $\sim$1 dBZ at 6 km altitude and can observe precipitation-sized particles (>0.2 mm diameter). This radar has insufficient sensitivity to observe cloud droplets or cloud ice. The K-band wavelength attenuates in moderate and heavy rain, so data within snow layers above deep rain layers are unreliable.

Stony Brook, NY does occasionally receive wet snow which can sit on the MRR antenna and attenuate the radar signal. This type of attenuation is usually fairly obvious in the time-height graphs as the lower level reflectivities are strong and the echo top becomes very jagged. The ten year data set was visually examined for frequency of attenuation of MRR signal, and it appeared infrequently at 3 times in a winter month. The majority of attenuation cases have a clear melting layer or have a deep rain layer and are excluded from analysis. Some of the wet snow periods will be removed as part of quality control checks if there is a clear melting layer or the echo height is < 1 km. Additionally, if more than 75% of echo in block average is missing it is not calculated and that time period skipped for the ice streamer counts. Hence, attenuation is more likely to yield a missed ice streamer detection. We assume that wet snow does not preferentially occur at a given time of day so the impact of these data problems not artificially enhance a diurnal cycle.

The Doppler fall velocity for a radar resolution volume is defined as:

$$V_D = V_F + V_A$$

where V_D is the radar-observed Doppler velocity, V_F is the mean fall velocity of the hydrometeors within the volume, and V_A is the mean velocity of the air within the volume. By convention for the MRR, V_D is positive for downward motions and negative for upward motions. As long as some signal is returned from the radar resolution volume, the Doppler velocity value is not affected by attenuation.

This analysis uses data obtained during the winter season from November to March from 2007-2018 consisting of 14,877 hours with radar echo which is the equivalent of almost 620 days. In terms of echo duration in a given calendar day, there are 1002 days with at least 6 hours of echo and 560 days with at least 12 hours of echo. In some winters the radar was down for part of the time. The radar settings varied slightly from season to season. The MRR-2 was set to have a time step of 30 s or 60 s and a gate spacing of 150, 200 or 250 m. It was shown in Section 1.2.1 that generating cells are on the scales of 1-3 km in the vertical and horizontal, so even the coarsest gate spacing would resolve an ice streamer in the vertical. The lifespan was typically 10 minutes, which would be resolved at either a 30 s or 60 s time step. These data are post-processed using the IMProToo toolkit of Maahn and Kollias (2012) to remove noise and dealias the Doppler velocities. Maahn and Kollias (2012) removes noise based on the most significant peak in the data and has a dynamic dealiasing routine which allows for observations even if the Nyquist velocity range was exceeded.

2.2 Methods

The MRR reflectivity and Doppler velocity time and height information are used as inputs to a set of image processing steps to identify ice streamer features. Echos with short duration and within the melting layer and rain are removed from further analysis. The remaining echo in ice is examined to identify vertically-connected points with enhanced reflectivity compared to the background reflectivity value. These points are then further filtered and combined into a single feature to yield number of ice streamers per hour and ice streamer characteristics such as vertical extent and duration.

The reflectivity data are converted from the observed dBZ values to linear Z (mm^6/m^3) for all calculations (Warren and Protat 2019). When dBZ values are displayed in figures these are converted from linear Z as a last step.

2.2.1 MRR Data Cleaning Filters

Hours with Echo

Each hour of MRR reflectivity data is examined to assess the temporal continuity of radar echo. Short duration echos which are less than 30 minutes (black box in Fig. 2.1a,b,c) are filtered out. Since one of the key metrics of the analysis are counts of ice streamers per hour, we determined that if an hour had less than 30 minutes of continuous echo it would not be sufficiently comparable to hours that contained 30 minutes or more of echo. Additionally, if the total height of a column was less than 1000 m the entire column was removed from analysis.

The total hours of observations that were recorded during the study period will be larger than the hours with echo that are examined for ice streamers. The observation time period contains periods of precipitation, times with no precipitation, and so no echo, and times with very short duration that can not be examined. The number of Micro Rain Radar observations per hour and hours with echo for the entire time period from Stony Brook are plotted in Fig. 2.2. There are over 1300 observations for each hour. Once the filtering methods described in this Section are completed on the reflectivity data, the hours with echo that are examined for ice streamers become about 600 per hour. The variations shown are less than 50 hours of echo from maximum to minimum counts per hour. Precipitating winter storms at Stony Brook occur during both day and night and there is no appreciable preference for time of day. There are a total of 14,877 hours of Micro Rain Radar data with $\geq$ 30 min of echo.

Melting Layer and Rain Regions

Non-ice portions of the radar echo including the melting layer and the rain region below the melting layer, are removed from the analysis. The melting layer is identified using downward gradients in reflectivity and Doppler velocity following Endries et al. (2018) which is based on principles from Austin and Bemis (1950). The bottom of the melting layer is identified as the location of the steepest gradient in velocity and the top of the melting layer is the steepest gradient in reflectivity.

Melting layer pixels are checked for consistency and plausibility in height. Adjacent points need to be within 400 m altitude of each other. Melting layers above 4250 m altitude are excluded, as a melting layer higher than 4250 m altitude is implausible for winter in New York. Any time there is a one minute or less gap between two times identified as melting, the time is considered to also be melting. When a set of melting layer points is $\geq$ 15 minute duration, the echo from the top of the melting layer to the surface is removed from analysis (Fig. 2.1 (d)).

2.2.2 Identification of Ice Streamers

We examined idealized time-height data sets designed to address a range of plausible ice streamer configurations as well as MRR-2 time-height data from 22 example storms at Stony Brook exhibiting a range of structures to develop and refine methods and to determine specific parameters to distinguish ice streamers within radar echo (Appendix A Figs. A.1 - A.19).

Distinction Between Pixel and Background

Since ice streamers are locally enhanced reflectivity, potential ice streamer pixels are identified using a relative difference from the background reflectivity. Relative differences often work in a wider range of storm structures as compared absolute reflectivity thresholds and are the basis of well-tested convective-stratiform identification algorithms and convective storm tracking algorithms (Yuter et al. 2005; Kober and Tafferner 2009; Dixon and Wiener 1993). Other studies have used relative thresholds to identify hail in radar images (Skripniková and Řezáčová 2014; Mallafré et al. 2009; Ni et al. 2017)

The background reflectivity in the time-height array is the average reflectivity within a box centered on the pixel that is 40 min in length and 1000 m in height (Fig. 2.1 (e),(f)). If the pixel is near an edge of the observed echo, then the background average is calculated from the subset of the 40 min by 1000 m box with echo. If more than 75% of the points within the 40 min by 1000 m box do not have echo the background reflectivity will not be calculated and that point is excluded from analysis. Calculations for the block average for hours 0000 to 2359 UTC each day were made using 26 hour blocks spanning from 23 UTC the previous day to 01 UTC the next day. Utilizing information from the day before and day after prevented biases from truncation of the data at 0000 and 2359 UTC.

For ice streamer pixel identification, and the relative difference between the pixel's reflectivity (Z_{pixel}) and background reflectivity is determined by

$$Z_{distinction} = b\cos\left(\frac{\pi Z_{bg}}{15000}\right) \tag{2.1}$$

where Z_{bg} is the average background reflectivity in the 40 min by 1000 m box, $Z_{distinction}$ is the threshold relative difference between the pixel's Z and Z_{bg}, and the coefficient b is a tuning parameter. The scaling parameter of 15000 m^6 m^{-3} corresponds to 41.7 dBZ. This equation yields larger $Z_{distinction}$ values for lower Z_{bg} values (Fig. 2.3) and is only applied for $Z_{bg} \leq 38$ dBZ. High background reflectivity values above the melting layer altitude are usually associated with deep convective cores and we do not attempt to identify ice streamers in those conditions.

Since it is difficult to determine perfect values for tuning parameters, we bound our best estimate for b with a value that will yield a realistic undercount and overcount of ice streamers. The subsequent analysis utilizes all three b values to demonstrate that the results are not very sensitive to small variations in the definition of $Z_{distinction}$. Based on idealized data sets designed to address a range of conditions as well as MRR-2 data from 22 example storms at Stony Brook, the best estimate of $b = 2.5$, lower bound $b = 4.5$ and upper bound $b = 1.5$. The lower bound yields an undercount of ice streamers and the upper bound yields an overcount of ice streamers.

The histogram of background reflectivity values (Fig. 2.4) computed using a 40-min by 1-km moving average method has a peak at 12-14 dBZ. These background values represent smoothed reflectivity values in the echo data set.

Ice Streamer Feature Identification and Filtering

We focus on detecting generating cells and associated ice streamers near echo top. Potential ice streamer pixels are consolidated into individual ice streamer features by aggregating the points which are continuously connected using an 8-connected definition (MATLAB Regionprops function 2020).A pixel identified as an ice streamer is 8-connected when that pixel is adjacent to at least one other pixel identified as an ice streamer on either an edge or diagonal (i.e. any of the 8 pixels surrounding the center pixel). The identified ice streamers from the 8-connected definition are labeled in Figure 2.5. Ice streamer features that are less than 500 m in total vertical extent, or 2 min in width are removed (Fig. 2.6). The typical gate spacing was 250 m, so in order to ensure that an ice streamer was truly a representative area of vertically continuous high reflectivity it was restricted to longer than 1000 m in the vertical. As a filter to further restrict the reflectivity structures composed of falling particles, we compare the times of the highest and lowest altitudes within the ice streamer and remove any ice streamer features where the lowest altitude ice streamer pixel is more than 5 minutes earlier than the highest altitude pixel.

2.2.3 Ice Streamer and Radar Echo Characteristics

Depth of Snow Echo

As part of the analysis, the depth of the snow portion of the echo is tabulated. For each time, the top of the snow echo is the highest altitude Z value. The bottom of the snow echo is identified as either the top of the melting layer or if there is no melting layer at that time, the lowest altitude Z value. The lowest altitude Z value would be the lower extent of virga or the bottom of the observed column if it is snowing at the surface.

Ice Streamer Count and Frequency

Ice streamer features are counted for each UTC hour. If at least 60% of the ice streamer is in a given hour then that hour is counted as containing the full ice streamer (Fig. 2.7). If the ice streamer crosses over to the next hour, but at least 41% of the ice streamer is within either hour, 0.5 ice streamers are added to the count for each of the two adjoining hours (Fig. 2.8). Accounting for partial ice streamers avoids over counting the same ice streamer in two adjacent hours.

The entire data set is used to determine ice streamer frequency for each UTC hour to assess the diurnal cycle of occurrence of ice streamers. The ice streamer counts are normalized for each hour 0 to 23 UTC by dividing the number of ice streamers by the number of times echo is observed during that hour (Fig. 2.2 Section 2.2.1).

Since the ice streamers are analyzed and counted by files, rather than by start and end time a second check is put in place to avoid over counting at the edges of the files. Any ice streamers who start at the beginning of a file and are within one hour of the end of an ice streamer from the file for the previous day are analyzed with the same 60/41 method mentioned above. The counts are then adjusted to accommodate these changes.

2.3 Ice Streamer Detection Sensitivity on Idealized Radar Data

We analyzed idealized cases constructed from synthetic data to test the sensitivity of the ice streamer detection algorithm to specific values. We constructed several test cases using time-height arrays featuring either a constant or linearly varying background reflectivity with respect to time and constant or linearly varying dBZ values for the idealized ice streamers. Figures 2.9, 2.10, 2.11) illustrate tests where the background was held constant at 10 dBZ and the synthetic ice streamers varied by 0.5 dB with the initial value of 33 dBZ. Tests with varying background (not shown) yielded consistent results.

The ice streamers geometries examined included tilting to the left (decreasing altitude with time), straight, and tilting to right (increasing altitude with time) (Figs. 2.9, 2.10, 2.11) The algorithm identified ice streamers with a significant tilt, as was expected as long as there was a point that was connected at one of the 8-connected pixels as described in Section 2.2.2.

From these test cases it is shown how sensitive the algorithm is to the b value in equation 2.1 that is used to determine the low, high, and best counts. The distinction function is used to decide how different the reflectivity values in the connected feature have to be from the background reflectivity to be counted as an ice streamer. In effect, over count method looks for a difference of 0.5 dB, best 0.75 dB, and under count 1 dB.

2.3.1 Monte Carlo Significance Testing

We use harmonic fits and comparisons between 6-hours means to determine if a potential diurnal cycle is present in the average frequency of ice streamers per hour. A Monte Carlo test assess whether the amplitude of the diurnal cycle is the result of random variation. Monte Carlo significance tests do not assume that the data have a particular distribution shape and hence are more general than Student-t and Chi-squared significance tests (BIPM et al. 2020). A Monte Carlo test is limited by computational power and the quality of the inputs to the model. The number of iterations constraints the precision, and the confidence limits. With 10,000 iterations the Monte Carlo test can only be used at 95th percentile (Lerche and Mudford 2005). Our tests of 10,000 iterations took about 4 hours to complete. The time scales with the number of iterations so 100,000 iterations would take 40 hours to compute.

The Monte Carlo test takes an input of a one dimensional vector and randomly shuffles the original ordered sequence into a new sequence. The new sequence is used to compute the harmonic fits for one iteration of the shuffle. This process is repeated for *M* iterations. We define T_i as one instance of shuffled data, where *i* goes from 1 to *M*, and here *M*=10,000. *N* is the number of days in the actual data set (N=2485). For example, for the first day (*N*=1) in T_1 the original data order of 0 to 23 could get shuffled to 14, 22, 20, 21, 12, 5, 2, 16, 15, 17, 3, 18, 13, 19, 9, 4, 7, 10, 8, 1, 23, 11, 6, 0. For day *N*=2, the 0 to 23 would get shuffled into a different order. We use the amplitude of the harmonic fits as the key metric in the Monte Carlo significance testing.

For our analysis, an instance of shuffled data T_i is constructed as follows:

1. For each day's data the hours with echo are shuffled by hour to yield a shuffled day. The daily shuffling is done for each of the N days. A different random number is used for each day so that individual days are shuffled differently. In effect, this preserves the actual time period of each storm and just shuffles the number of ice streamers in each hour during the storm. Two metrics are computed from each iteration T_i to determine if a diurnal variation is present:

2. Metric 1 (harmonic fits): A new average ice streamer frequency for each UTC hour 0 to 23 is calculated for the set of N days and are input to a harmonic analysis test. The phase and amplitude for the first and second harmonics are recorded.

3. Metric 2 (comparison of 6-hour means): The average ice streamer frequencies for two sets of contrasting 6 hour periods are calculated. The difference between the two values is recorded.

Steps 1) - 3) are repeated for each instance T_i for a total of 10,000 iterations. There are over 10^{23} permutations of 24 numbers so we do not expect any exact repeats among the 10,000 iterations. Finally, the set 10,000 shuffled amplitudes and the set of shuffled differences between day and night means are sorted to determine the 95^{th} percentile. If the actual data have an amplitude > 95^{th} percentile of the 10,000 shuffled values, then there is a 1 in 20 chance that the actual datas' value is the result of a random process.

The harmonic fits are computed using the MATLAB *Harmfit* function (Beauducel 2021), a MATLAB file exchange function, which outputs the amplitude and phase of the first four harmonics of the input one dimensional vector. The time series corresponding to hours 0 to 23 UTC is rescaled to 0 to 2π prior to input to *Harmfit*. The ice streamer frequencies are rescaled to a mean of 0 prior to input into *Harmfit*. Figures 2.12 and 2.13 show idealized example 24 hour time series and the resulting four harmonic fits as well as the amplitude and phase of each fit.

We tested the harmonic fit and Monte Carlo statistical analysis code using idealized data sets of counts per hour designed to have a clear diurnal cycle. The idealized counts were created based on a sine wave with an amplitude of 1 that is centered at 12 UTC shown as the black dashed line in Figure 2.14. N daily instances are created by assigning each hour a value based on a Gaussian distribution (with standard deviation of 1) around the value for that hour in the simple sine wave. Figure 2.14 shows 5 example days and illustrates that the mean of each daily instance closely matches the mean of the simple sine curve. The N x 24 array of counts represents an idealized version of the radar-derived counts. The average frequencies are determined and the phase and amplitude of the first four harmonics computed from these simulated data sets (Fig. 2.12). For testing we varied N and the mean amplitude A. The N days of counts are then shuffled using the Monte Carlo process described above. Figure 2.15 shows the maximum phase and amplitudes for the shuffled data as compared to the idealized test data for N = 1300 and sine curve amplitude A = 1. For the first harmonic, the maximum amplitude of the test data is > 95th percentile of the shuffled data. The results for the second harmonic are shown in Figure 2.16. If the data passes the 95th percentile test (equivalent to p-value of 0.05), then there is still a 1/20 chance that the result is random but there is a 19/20 chance that it is not. For our work, the null hypothesis is that there is no diurnal cycle. While we cannot tell if something is 100% not due to a random process, it is generally accepted that 1/20 is sufficient evidence to reject the null hypothesis and in our case to yield evidence for a diurnal cycle. Based on Figure 2.15, the maximum amplitude of the real data is > 95th percentile for the first harmonic yielding evidence of a diurnal cycle. Based on Figure 2.16, the real data's amplitude is < 95th percentile for the second harmonic, so there is no compelling evidence of a semi-diurnal cycle.

Additionally, we calculated the p-values by using equation 2.2,

$$p = \frac{r}{n} \tag{2.2}$$

where r is the number of simulations which are greater than the 95th percentile of the observed data and n is the number of simulations. For this study r varied for each counting method and n is 10,000 (North et al. 2002).

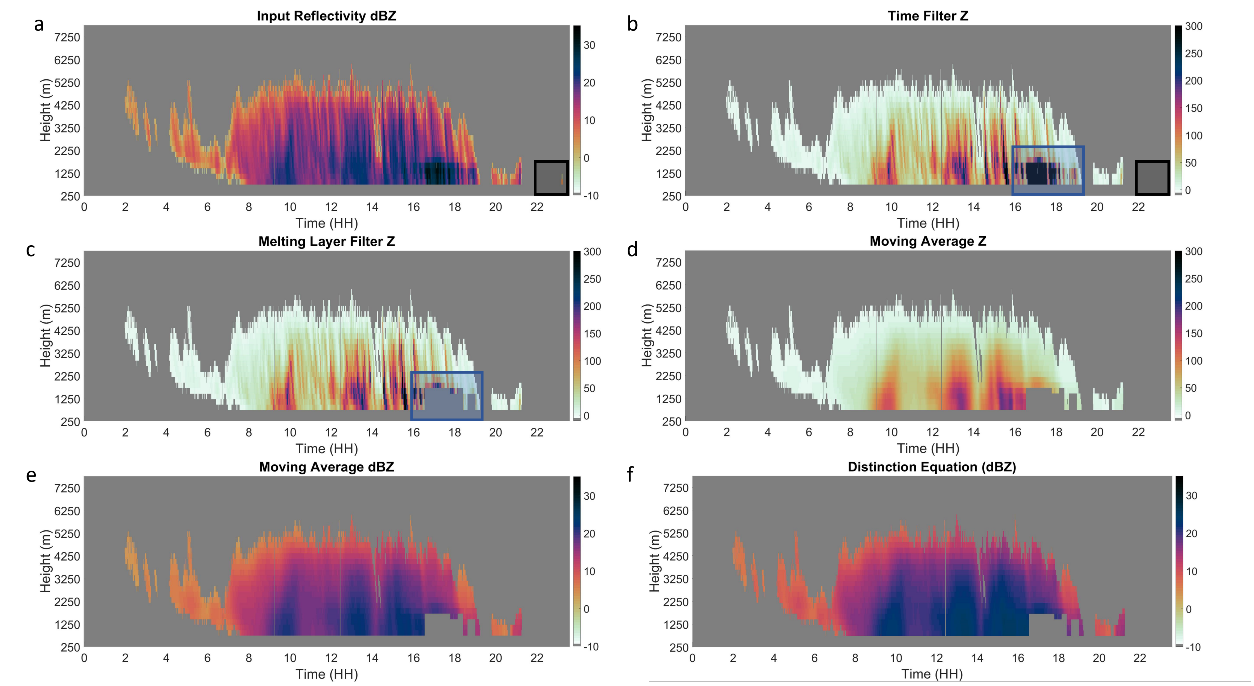

Figure 2.1: (a) The reflectivity that is read in from the MRR preprocessed netCDF file is converted from dBZ to Z and then (b) periods of echo that are less than 30 minutes in a 60 minute period are removed. The black box in (a) shows a location of echo less than 30 minutes and the black box in (b) shows where it was removed. The final step is, (c) areas identified as melting have been removed. The light blue box in (b) shows an area of melting and the same light blue box in (c) shows where it was removed. (d) shows the background average that is calculated.(e) shows the background averages + the distinction for that point

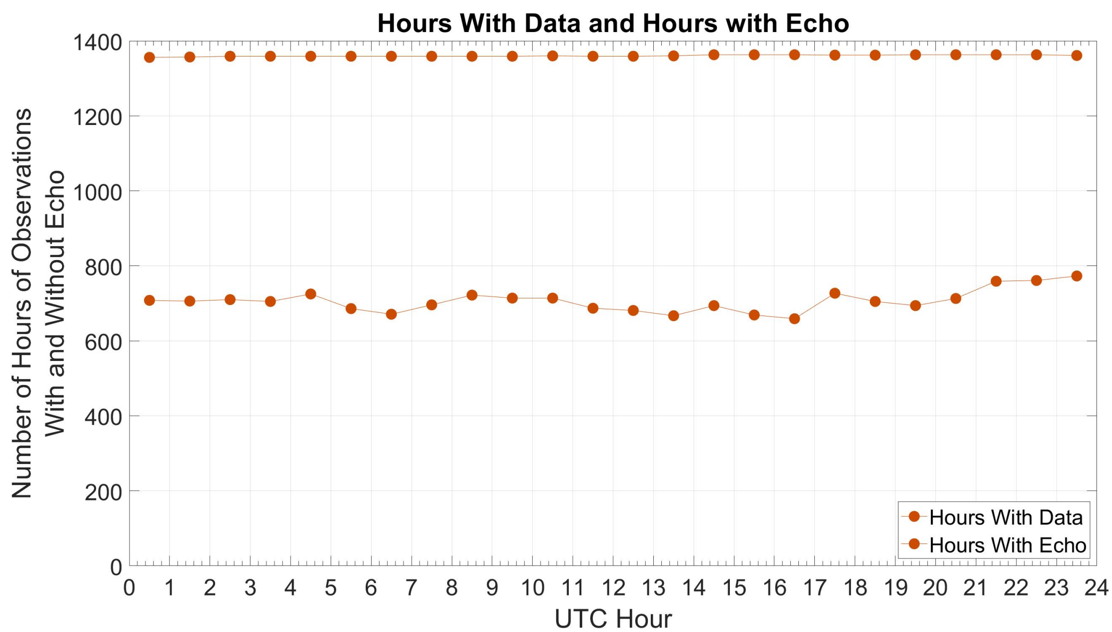

Figure 2.2: Sample sizes of observations per hour (circles) and hours with echo (diamonds) that are analyzed in this study.

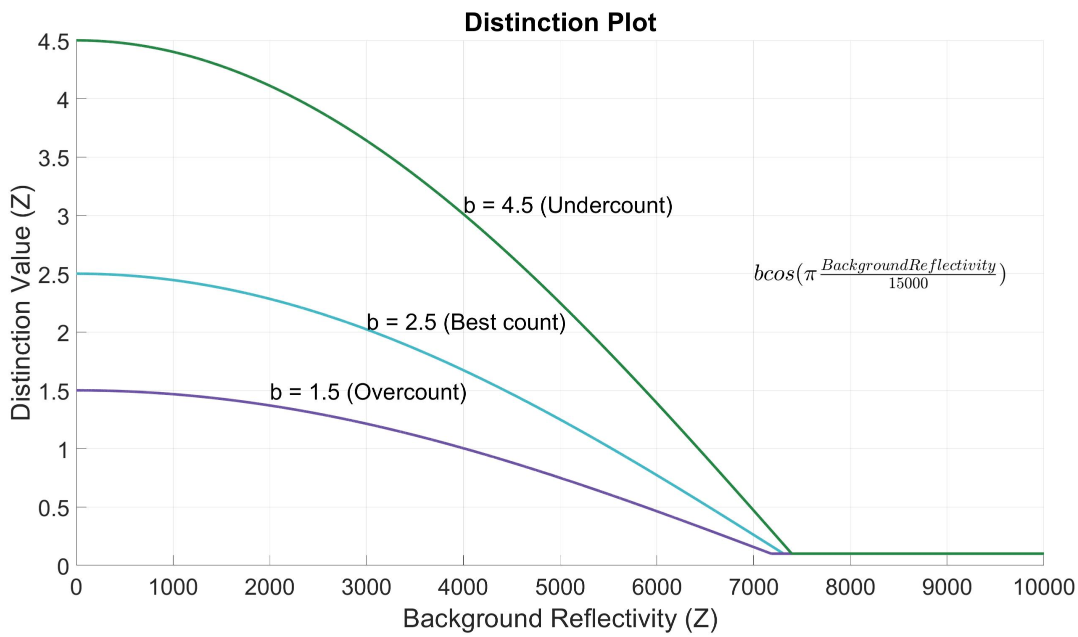

Figure 2.3: The curves showing the distinction equation value for each background Z value in mm^6/m^3. The three curves show the distinction values for an overcount of ice streamers where b = 1.5 (purple line), best guess where b = 2.5 (blue line), and the under count where b = 4.5 (green line).

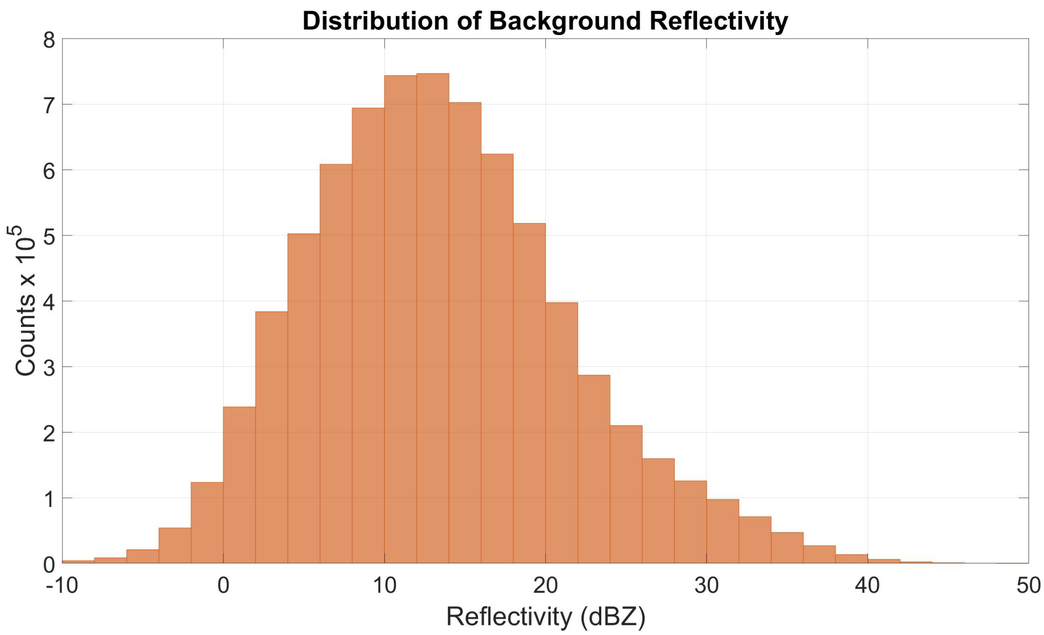

Figure 2.4: Histogram of the background reflectivity values from the entire data set after the filtering methods have been applied.

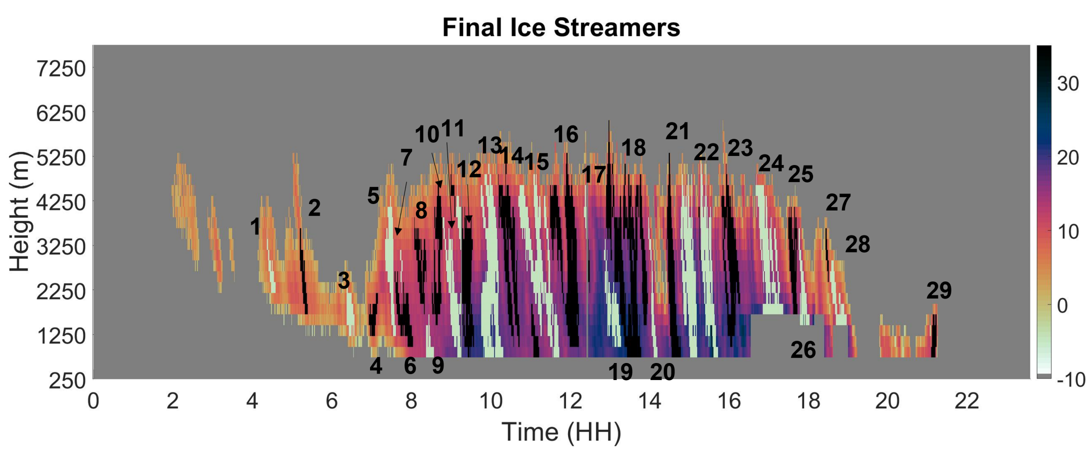

Figure 2.5: Ice streamers are alternated colors grey and black. Each ice streamer is assigned a number. The 8-connected points cause ice streamer 10, 13, and 19 to be counted as a single ice streamer.

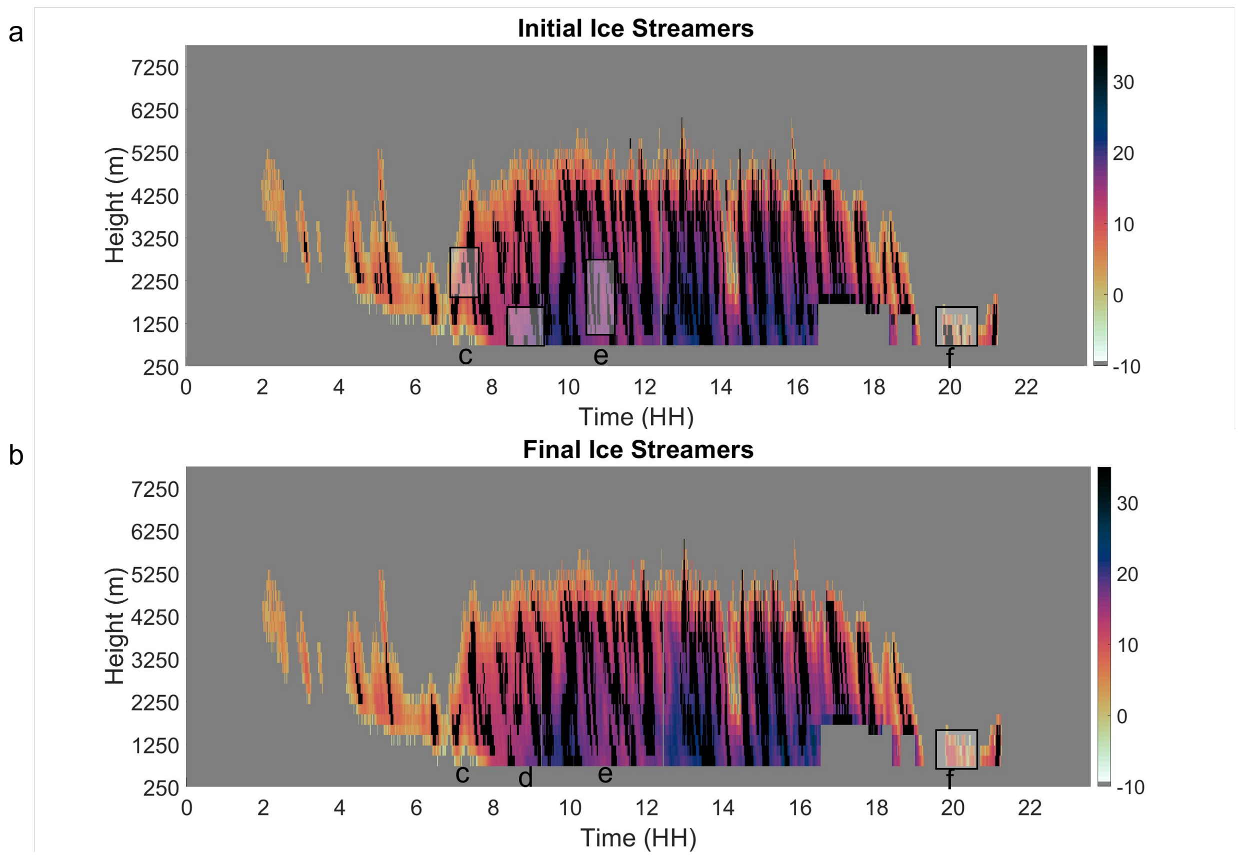

Figure 2.6: (a). The pre-filtered ice streamers and (b) the post-filtering ice streamers have small differences. (c),(d) has ice streamer which meet neither the height nor length in time requirements. The large ice streamer in (e) is not 1000 m in height and the others do not meet the height or time requirement. (f) does not exceed 1000 m

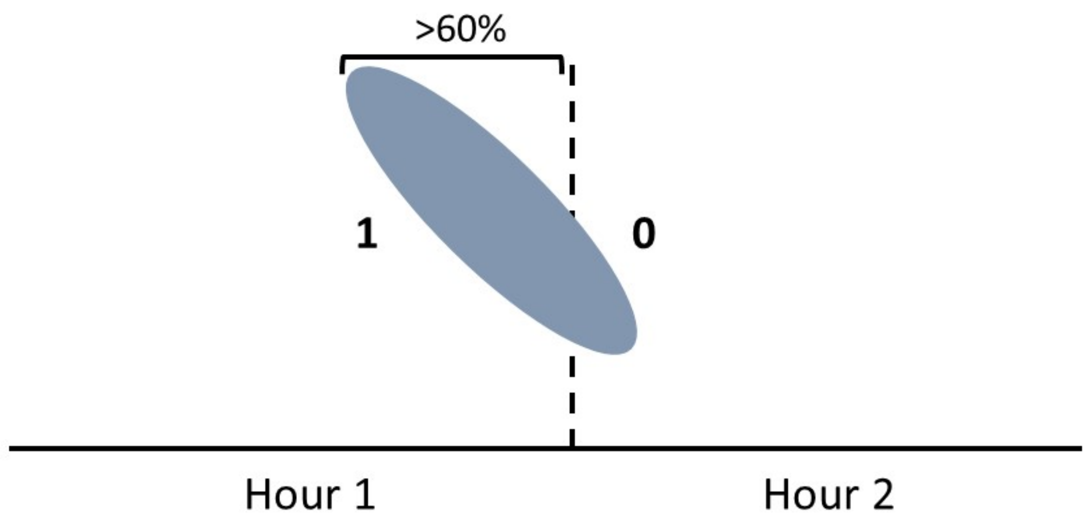

Figure 2.7: An ice streamer, the grey oval, crosses the hour into hour 2, and at least 60% of the ice streamer is within hour 1, so the ice streamer is counted as totally occurring in hour 1 and a value of 1 is assigned to the count for hour 1 only.

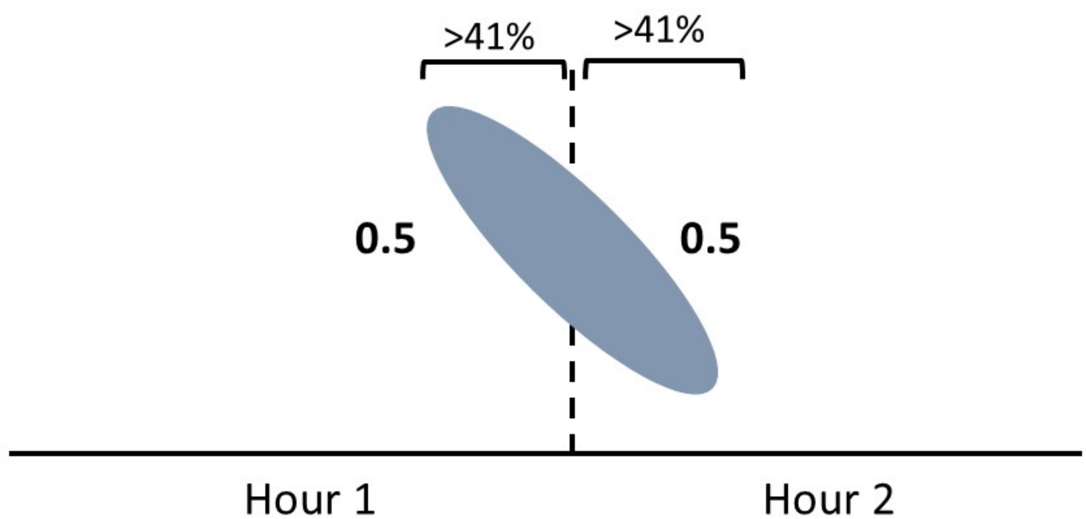

Figure 2.8: As in Figure 2.7, except the ice streamer has less than 60% within any one hour, but more than 41% in hour 1 and in hour 2. The ice streamer is counted as being partially in both hours and a value of 0.5 is assigned to the counts for hour 1 and hour 2.

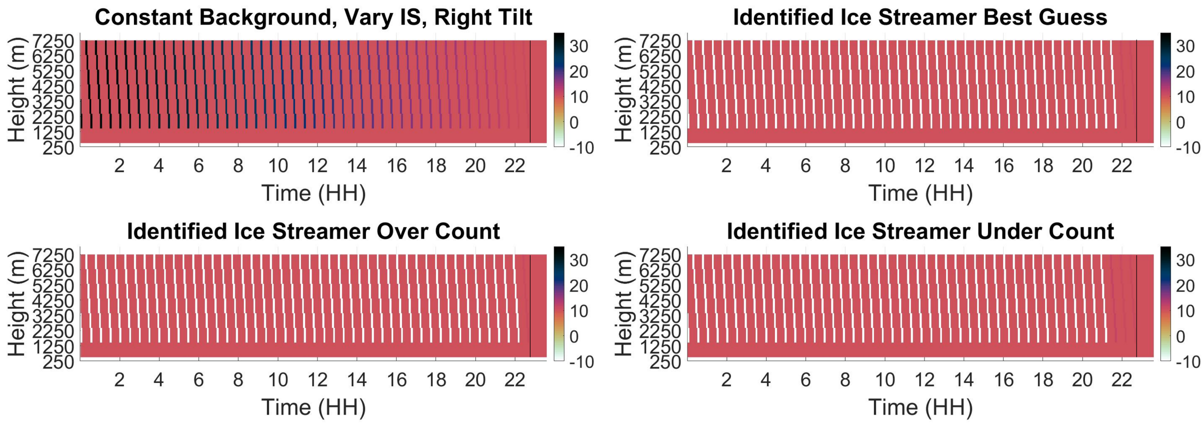

Figure 2.9: Idealized example using a constant background value of 10 dBZ and varying the ice streamer values starting at 33 dBZ (left edge of each panel) and decreasing by 0.5 dB each ice streamer to a minimum value of 10.5 dBZ (2303 UTC, after this time the ice streamer would be equal to the background). Identified ice streamers are shown in white. The black line in each panel denotes the edge of the last ice streamer in the input data from (a). In this example, compared to (b) best guess, (c) over count has one more ice streamer identified and (d) under count has one fewer.

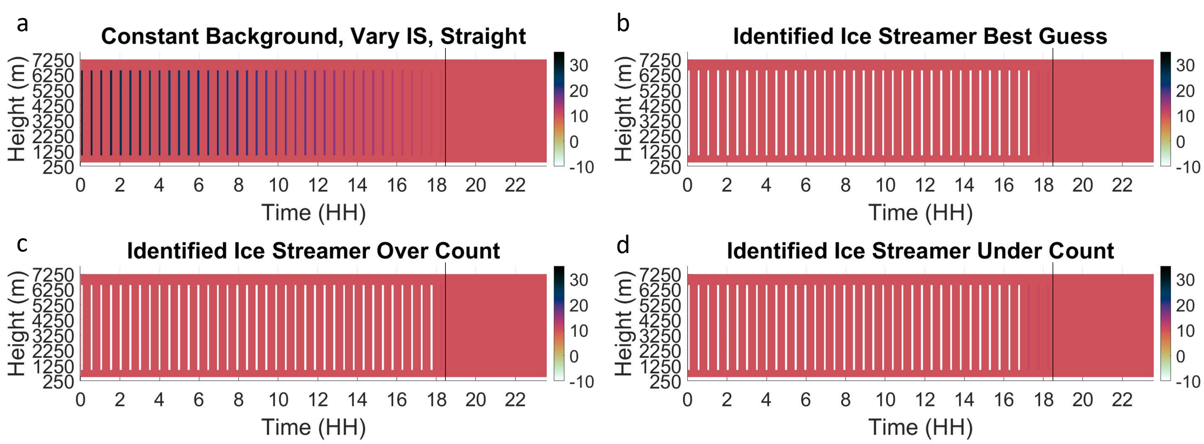

Figure 2.10: Idealized example using a constant background value of 10 dBZ and varying the ice streamer values starting at 33 dBZ (left edge of each panel) and decreasing by 0.5 dB each ice streamer to a minimum value of 10.5 dBZ (1830 UTC, after this time the ice streamer would be equal to the background). The black line in each panel denotes the edge of the last ice streamer in the input data from (a). Identified ice streamers are shown in white. In this example, compared to (b) best guess, (c) over count has one more ice streamer identified and (d) under count has one fewer.

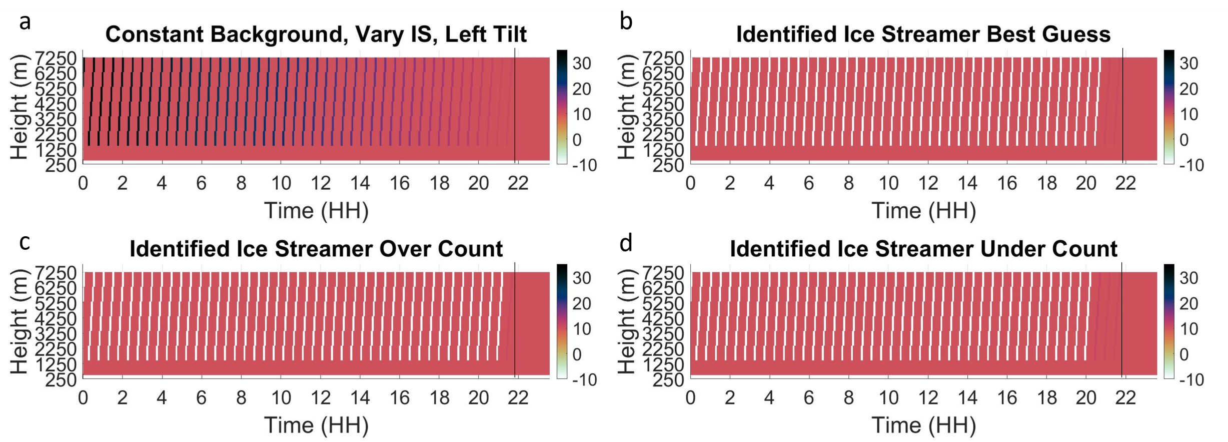

Figure 2.11: Idealized example using a constant background value of 10 dBZ and varying the ice streamer values starting at 33 dBZ (left edge of each panel) and decreasing by 0.5 dB each ice streamer to a minimum value of 10.5 dBZ (1830 UTC, after this time the ice streamer would be equal to the background). The black line in each panel denotes the edge of the last ice streamer in the input data from (a). Identified ice streamers are shown in white. In this example, compared to (b) best guess, (c) over count has one more ice streamer identified and (d) under count has one fewer.

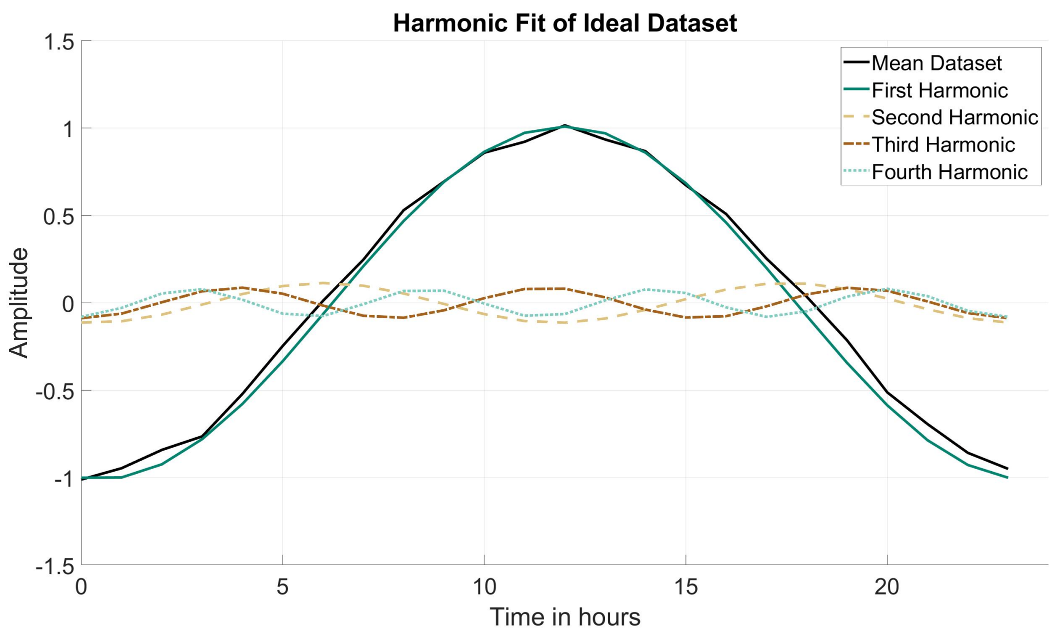

Figure 2.12: Demonstration of harmonic fit calculation. First four harmonic fits calculated for the idealized test data set based on a the mean of a set of sine waves with Gaussian noise and an amplitude of 1 centered on 12 UTC (black line). As expected, the first harmonic (solid blue line) is shown as the best fit to the data set.

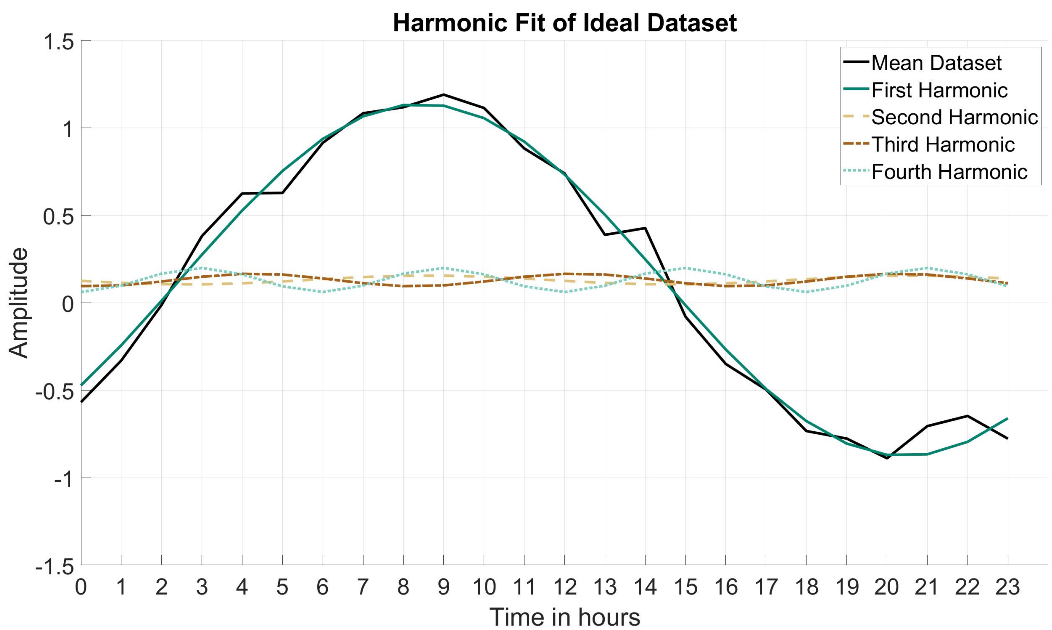

Figure 2.13: Demonstration of harmonic fit calculation. First four harmonic fits calculated for the idealized test data set based on a the mean of a set of sine waves with Gaussian noise and an amplitude of 1 centered on 8 UTC (black line). As expected, the first harmonic (solid blue line) is shown as the best fit to the data set.

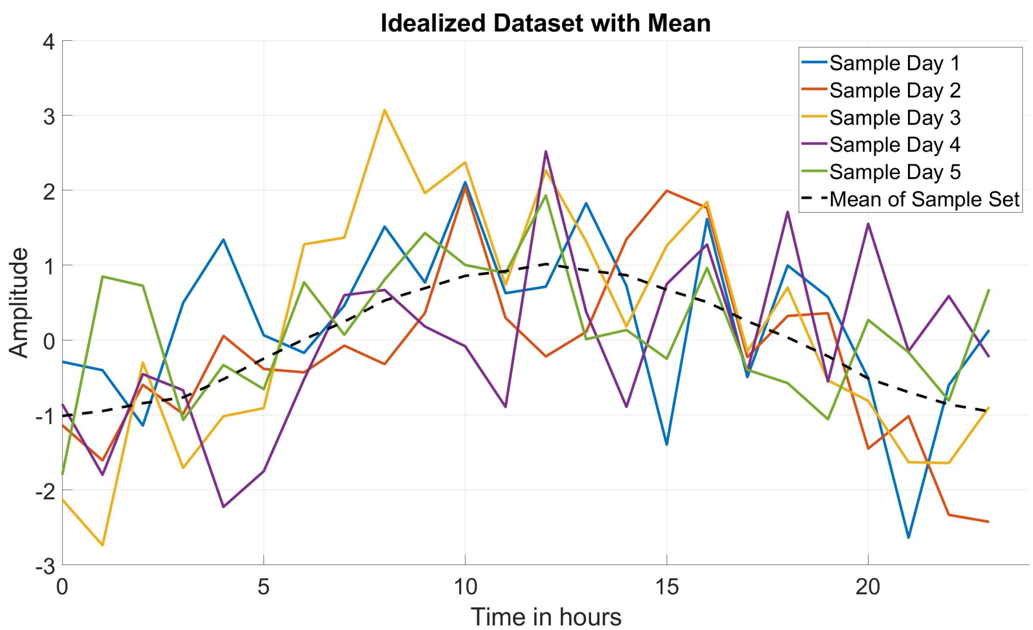

Figure 2.14: Examples from the idealized data set based on a sine wave with Gaussian noise used to test the Monte Carlo calculations. A sample of 5 individual days are shown in solid lines and the mean value of the 1300 days is shown as black dotted line. These data represent the "real" data for testing.

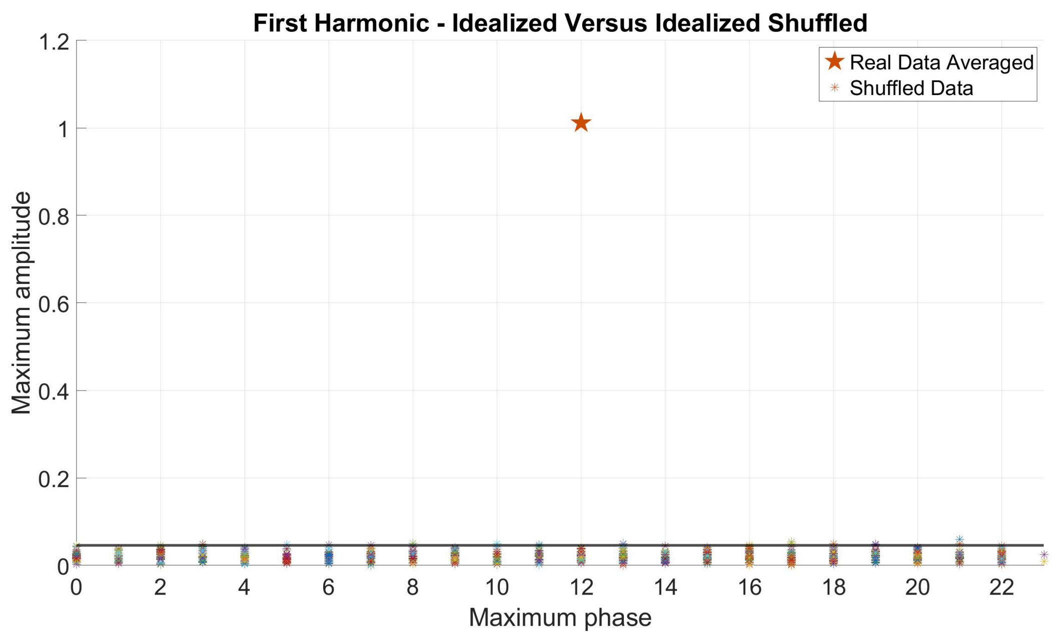

Figure 2.15: The idealized "real" data set was shuffled 10,000 times for the Monte Carlo simulation and the first harmonic fit for average of each shuffle was found and each maximum amplitude and phase is plotted as an X. The maximum amplitude and phase of the "real" idealized data set's first harmonic is plotted as an star. The 95% for the shuffled data is shown as a dotted black line. For the first harmonic, the amplitude and phase of the idealized "real" data is > 95%.

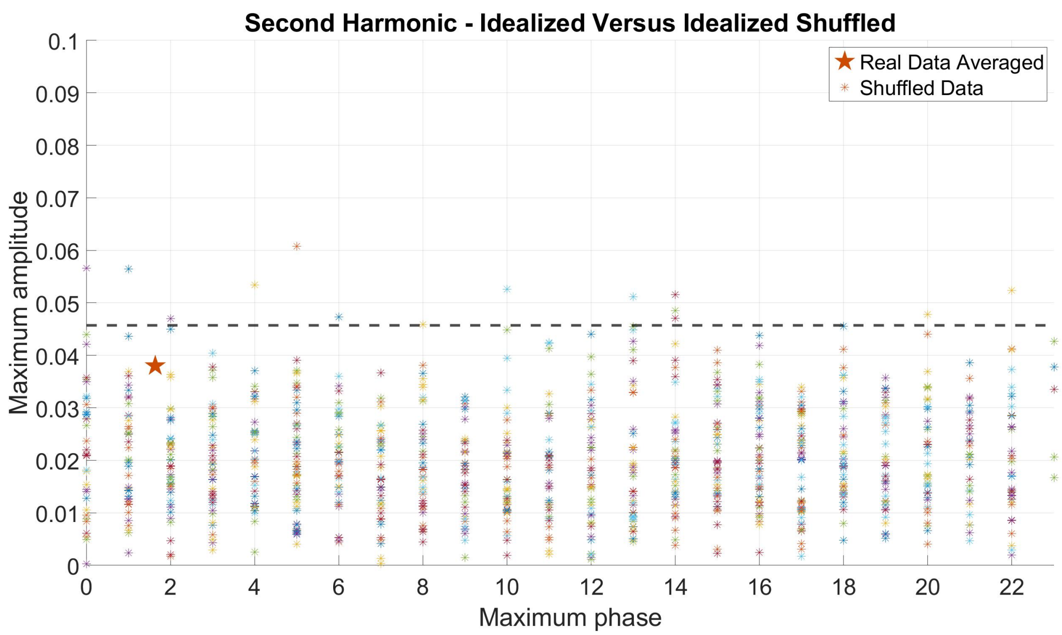

Figure 2.16: The idealized "real" data set was shuffled 10,000 times for the Monte Carlo simulation and the second harmonic fit for average of each shuffle was found and each maximum amplitude and phase is plotted as an X. The maximum amplitude and phase of the "real" idealized data set's second harmonic is plotted as an star. The 95% for the shuffled data is shown as a dotted black line. For the second harmonic, the amplitude and phase of the idealized "real" data is < 95%.

CHAPTER

3

RESULTS

3.1 Ice Streamer and Echo Characteristics

The ice streamers detected using the Micro Rain Radar data are those that are associated with sufficiently rigorous generating cells to produce precipitation-sized ice particles. Based on previous work, we expect that many ice streamers originate with reflectivity values below the minimum detectable sensitivity of the Micro Rain Radar and at higher altitudes than we can detect them. Hence, our quantification of ice streamer characteristics likely represents underestimates of ice streamer frequencies, vertical extent, and maximum altitude as compared to what a more sensitive radar such as an airborne downward-looking cloud radar data set would identify. There are 14,877 hours with echo that are examined, which provides a large sample size within a variety of winter storm structures at Stony Brook, NY.

3.1.1 Winter Storm Echo Characteristics

Winter storms tend to have lower CAPE and instability which yields lower echo tops compared to a summer thunderstorms. Echo top statistics are shown in Figure 3.1. A subset of hourly echo top distributions is shown in Figure 3.2. The local maxima in the distributions in Figure 3.2 at 4.4 km and 6.2 km altitude are an artifact of radar gate spacing settings. For periods when the gate spacing is 150 m, the maximum observable height is 4.7 km altitude, when the gate spacing is 200 m it is 6.2 km altitude, and when the gate spacing is 250 m it is 7.8 km altitude. With these limitations, 50% of the time the echo tops are below 4.5 km. Likely, most of the time we are not detecting the actual top of the ice streamer because of a combination of limitations of minimum sensitivity and radar settings.

The distance from the top of the observed echo to the top of each ice streamer was calculated and is shown in Figure 3.4. Ice streamers are found within 1 km of the Micro Rain Radar detected echo top 85% of the time. Hence we are in effect "catching" ice streamers formed from generating cells at altitudes higher than either the radar can detect or beyond the maximum Micro Rain Radar observable altitude. Given the limitations of the Micro Rain Radar observations, the average depth of the echo for each hour (Fig. 3.3) is an underestimate, and is below 2.8 km 50% of the time and below 4.6 km 85% of the time. The mean depth is similar between hours, varying only by 0.2 km. The filtering in Section 2.2.2 removed any areas of rain, and the figure shows only the depth of snow portions of the echo, so the large variation in the depth of echo is expected since there are storms with melting layer heights at different altitudes as well as storms that contain only frozen precipitation all the way to the surface.

3.2 Ice Streamer Counts

The ice streamer detection algorithm was applied to the echo data set as described in Section 2.2.2 for the best, overcount, and undercount estimate values. The ice streamer counts for each hour shown in Figure 3.5 are the total ice streamer counts from the entire Micro Rain Radar data set for each estimate type and UTC hour and confirms that the best, overcount and undercount estimates of the ice streamers for each hour maintains a consistent count of ice streamers relative to each other. The example shown in Figure 3.6, illustrates that best count does filter out a number of features that are not true ice streamers and keeps ice streamers that are missed with the undercount value. Within Figure 3.6, the time period from 2-8 UTC shows the largest difference between the three counting methods. The overcount method has 5 ice streamers more than the undercount method and 2 more than the best count method.

The ice streamer counts are normalized to a frequency per hour (Fig. 3.7) by dividing the counts for an hour by the number of hours of echo for the hour or the day. It is clear that ice streamers are a common phenomenon within echo, occurring more than 70% of the time in the best estimate and over 59% of the time in the undercount. During the winter at Stony Brook, NY the sunrise is typically near 1130 UTC and sunset is 2130 UTC (NOAA 2021). In Figure 3.7 this is a slight uptick in ice streamer frequency from 0800 UTC to 1300 UTC which spans several hours pre-dawn until just after sunrise. In the next section, we will examine whether this uptick constitutes evidence of a diurnal cycle using several variations of Monte Carlo significance tests.

3.3 Statistical Testing for Diurnal Cycle

To test the hypothesis that ice streamers have a diurnal cycle, Monte Carlo tests were performed as described in Section 2.3.1.The Monte Carlo test was completed using the normalized ice streamer counts. The normalized Monte Carlo test results could be multiplied by the counts of echo per hour and compared to the raw observed counts. This would give the same results in the statistical tests. The 10,000 iterations of shuffled data are used for the analysis in the harmonic fits and comparison of means for 6-hour time periods. The Monte Carlo testing is done for the best, undercount and overcount estimates separately. Key variables derived from shuffled data are compared to the real data to determine if the real data has diurnal cycle that passes the 95th percentile significance test. To account for uncertainty in the counting methodology, the 95th percentile significance test will not be considered to be met unless it passes for all three estimates.

3.3.1 Harmonic Fits

Harmonic fits to time series are useful for analysis of whether a diurnal cycle is present (e.g. Wallace 1975; Dai et al. 1999; Collier and Bowman 2004). The first four harmonic fits to ice streamer frequency per hour data for the real data are computed and shown in (Fig. 3.8, 3.9, and 3.10). The first harmonic, shown with the solid line in all three figures, fits the original data set the most closely with a peak amplitude centered at 10 UTC for all three estimates, best, undercount and overcount.

Summary data from the harmonic fit Monte Carlo tests are displayed in Table 3.1. In Figure 3.11 the shuffled maximum amplitudes for each iteration of the Monte Carlo on the best estimate data set are shown as well as the 95th percentile amplitude and the actual data set's maximum amplitude.

The best, undercount and overcounts of ice streamers have a first harmonic maximum amplitude greater than than 95th percentile of the maximum amplitudes of the shuffled data when rounded to the nearest 100^{ths} place (Fig. 3.12 and 3.13). This means that the amplitudes of the first harmonic have only a 1 in 20 chance of being random. Despite passing this statistical test, we do not think this constitutes practical significance. The amplitude of the first harmonic is so small, < 5% of the scale of the diurnal cycle, it much smaller than large effect discussed by Keeler et al. Keeler et al. (2017) do not have a directly comparable ice streamer frequency from their model, but their median vertical air motions of 1.64 m/s at night compared to 1.19 m/s during the day suggest an increase in strength of updrafts in generating cells of about 30% at night compared to during the day. Our methods will more readily detect stronger as compared to weaker generating cells.

3.3.2 Comparison of 6-Hour Means

In order to further examine the diurnal pattern of variations in ice streamer frequency at Stony Brook, NY during the winter we have defined two cases for contrasting 6-hour periods. The difference between the averages for these set 6-hour periods for both the shuffled data and the observed data will assess the strength and significance of a potential diurnal cycle in terms of a simple metric that does not require a harmonic fit to a sinusoidal curve. Test A contrasts a day period at 13-19 UTC (0800 to 1400 local time) and night period at 00-06 UTC (1900 to 0100 local time) (Fig. 3.14). Test B contrasts 6-hour periods spanning sunrise from 7-13 UTC (0200 to 0800 local time) and spanning sunset 19-01 UTC (1400 to 2000 local time) (Fig. 3.15). Table 3.3 shows the Test A means for the day and night periods and the Test B means for spanning sunrise and spanning sunset periods of the observed data set for the three ice streamer estimates. Consistent with the peak amplitude of ice streamer frequency at 10 UTC, there is a larger difference between the spanning sunrise and spanning sunset periods than for the day and night periods. The histograms of the distributions of the absolute value of differences for the shuffled data for Test A are shown in Figures 3.16, 3.17, and 3.18 and for Test B in Figures 3.19, 3.20, and 3.21.

In Test A, the differences between the observed night and day 6-hour means are all less than 0.014 per hour (Table 3.4, Fig. 3.16, 3.17, and 3.18) and much less than the 95th percentile values. In contrast, the differences between the observed 6-hour periods spanning sunrise and sunset (Test B) are much larger. All three counting methods (over, best, and under) have observed mean differences that are larger than the 95th percentile of the shuffled data (Table 3.4, Fig. 3.19, 3.20, and 3.21). This constitutes evidence of practical significance for a difference between the counts of ice steamers between the 6-hour period spanning sunrise and spanning sunset.

Table 3.1: Maximum amplitudes for the first and second harmonics for the real data set and the 95th percentile of the shuffled data set. Values correspond to calculations using overcount, best count, and undercount estimates for the real data. The amplitudes from the real data that exceed > 95% of shuffled data are in bold.

	Real Data		Shuffled Data	
	First Harmonic	Second Harmonic	First Harmonic	Second Harmonic
Overcount	**0.0373**	0.0287	0.3680	0.0364
Best Count	**0.0371**	0.0162	0.0366	0.0364
Undercount	**0.0453**	0.0017	0.0363	0.0359

Table 3.2: The P-Values for the first and second harmonics for the real data set compared to the Monte Carlo data. P-Values are based on the number of shuffles greater than the maximum amplitude of the real data. Values correspond to calculations using overcount, best count, and undercount estimates for the real data. The P-Values which are < 0.05 are in bold.

	First Harmonic	Second Harmonic
Overcount	**0.0465**	0.1632
Best Count	**0.0465**	0.5412
Undercount	**0.0089**	0.9938

Table 3.3: Ice streamer frequency mean values (fraction per hour) for the 6-hour periods for the real data for Test A for 6 hours during the day (13 UTC to 19 UTC, 0800 to 1400 local time) and 6 hours during the night (0 UTC to 6 UTC, 1900 to 0100 local time) and for Test B for 6 hours crossing sunrise and spanning overnight to early morning (7 UTC to 13 UTC, 0200 to 0800 local time) and 6 hours crossing sunset corresponding to late afternoon to early evening (19 UTC to 1 UTC, 1400 to 2000 local time). Values correspond to calculations using overcount, best count, and undercount estimates for the real data.

	Test A		Test B	
	During Day	During Night	Spanning sunrise	Spanning sunset
Overcount	0.7066	0.7203	0.6493	0.7620
Best Count	0.6632	0.6764	0.6494	0.7122
Undercount	0.5880	0.5949	0.5652	0.6368

Table 3.4: Absolute values of mean differences (fractions per hour) between 6 hours periods for Test A Night/Day, and Test B- Sunrise/Sunset for the real data compared to shuffled data 95th and 99th percentiles. The amplitudes from the real data that exceed > 95% of shuffled data are in bold.

	Test A real	Test A 95th	Test A 99th	Test B real	Test B 95th	Test B 99th
Overcount	0.0137	0.0564	0.0738	**0.1127**	0.057	0.073
Best Count	0.0132	0.0553	0.0732	**0.0628**	0.0565	0.0747
Undercount	0.0069	0.0543	0.0732	**0.0716**	0.0557	0.0735

Table 3.5: The P-Values for Test A and Test B for the real data set compared to the Monte Carlo data. P-Values are based on the number of shuffles greater than the maximum amplitude of the real data. Values correspond to calculations using overcount, best count, and undercount estimates for the real data. The P-Values which are < 0.05 are in bold.

	Test A	Test B
Overcount	0.6306	**0.0000**
Best Count	0.6431	**0.0229**
Undercount	0.8044	**0.0096**

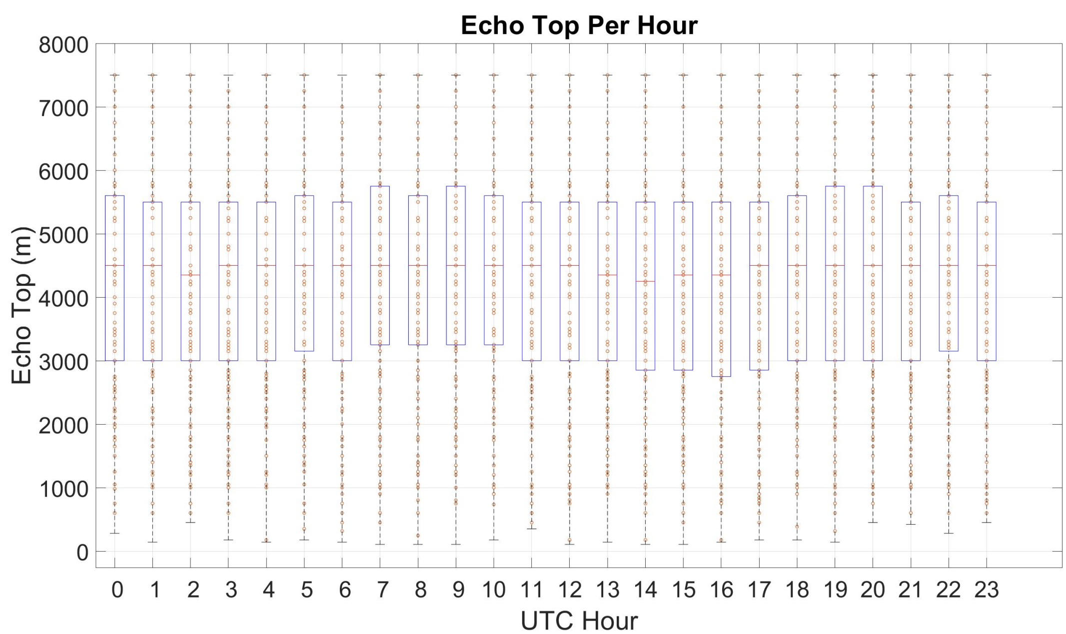

Figure 3.1: Echo top characteristics. The median is shown as the red line in each box. 75th and 25th quartiles plotted with the maximum and minimum shown as the whiskers for each plot. The orange circles are the individual echo tops for each hour.

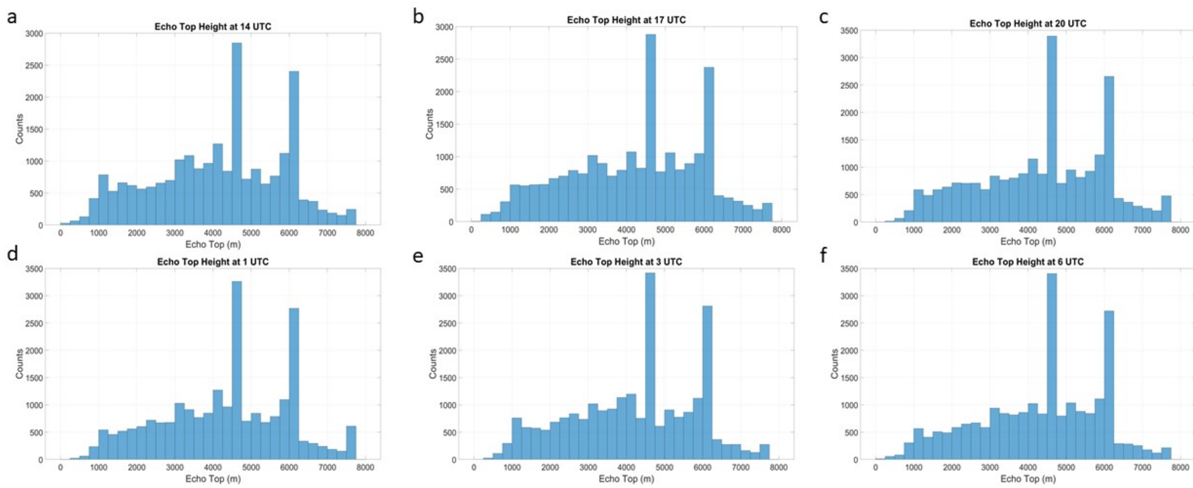

Figure 3.2: The distribution for the echo top at three times during the day (14, 17, 20 UTC) and three times during the night (1, 3, and 6 UTC), binned at 250 m. The hours chosen represent three times during the day (a-c) and three times during the night(d-f).

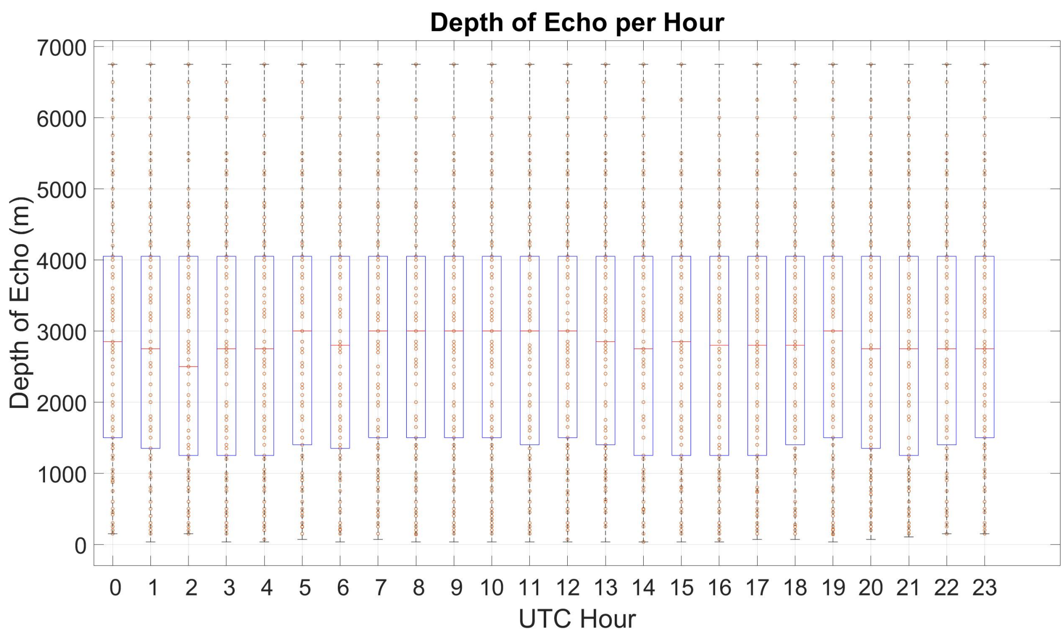

Figure 3.3: Echo depth characteristics. The median is shown as the red line in each box. 75^{th} and 25^{th} quartiles plotted with the maximum and minimum shown as the whiskers for each plot. The orange circles are individual depth of echo for each hour.

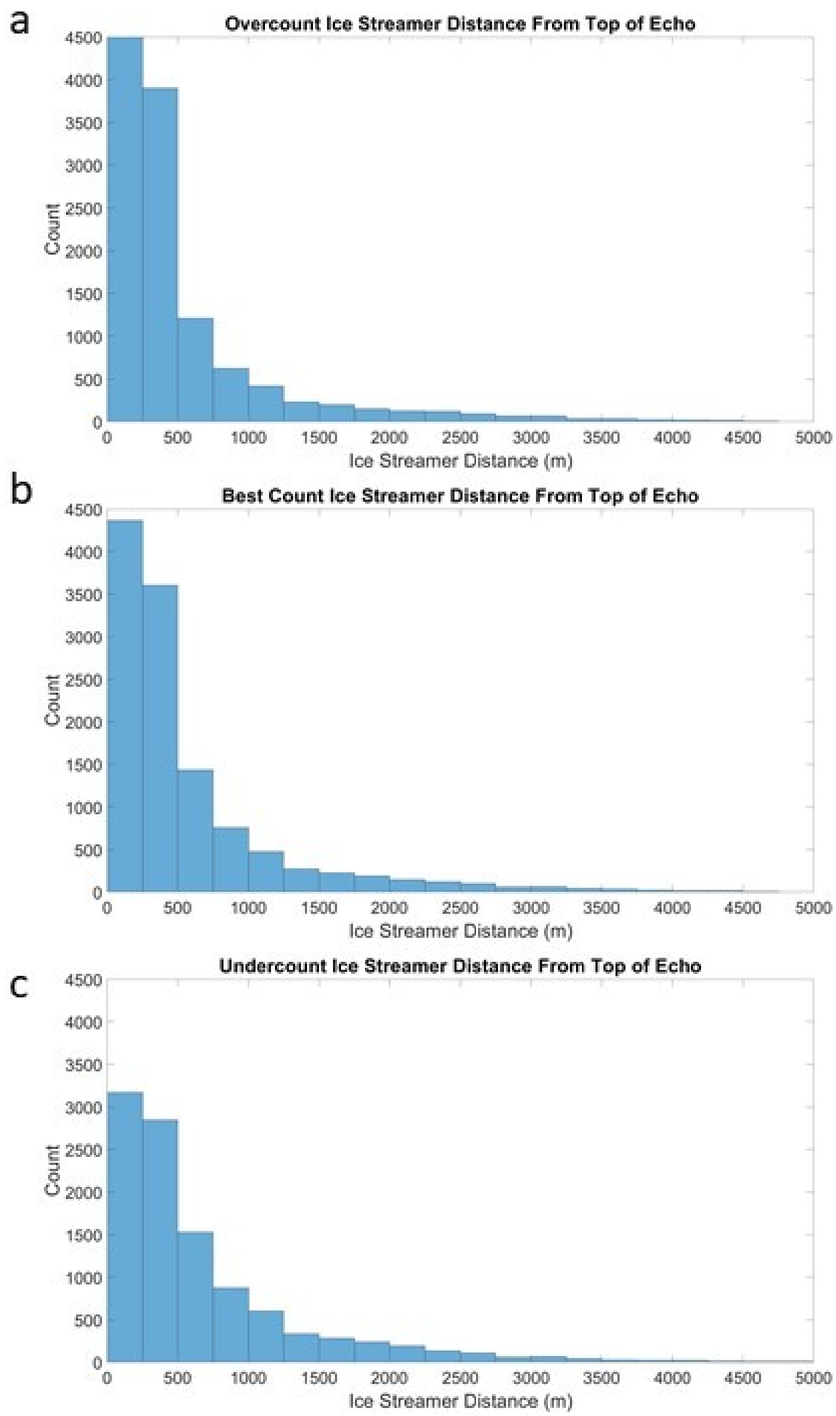

Figure 3.4: The distribution of the distance from the top of an identified ice streamer where the data is binned at 250 m. Overcount case (a), best count (b) and undercount (c).

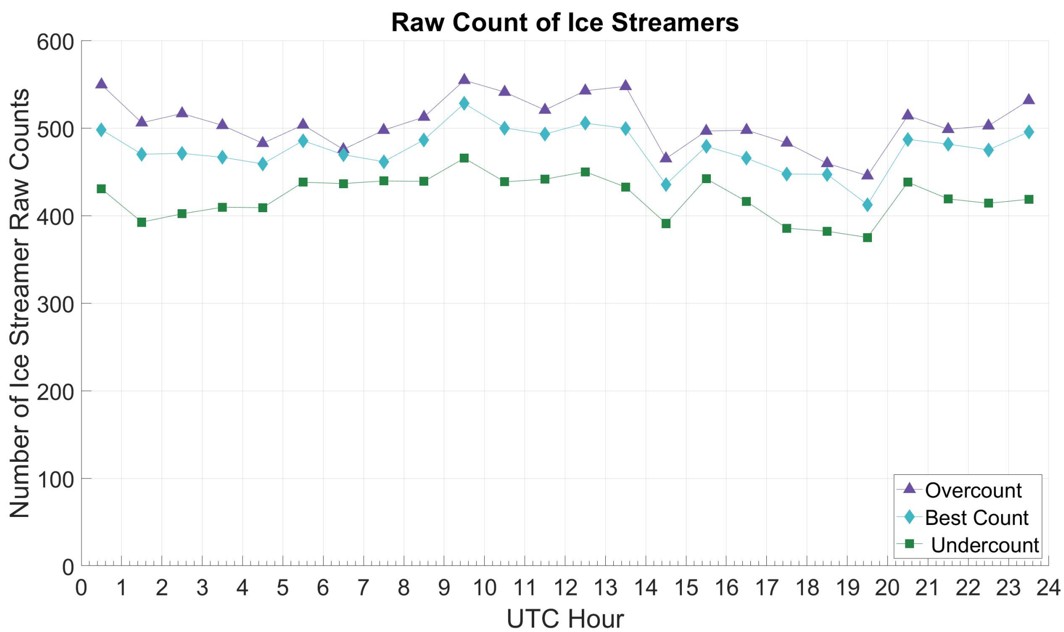

Figure 3.5: The total count of ice streamers for each hour from the entire data set for the overcount method, purple triangle best count method, blue diamond, and undercount method, green square.

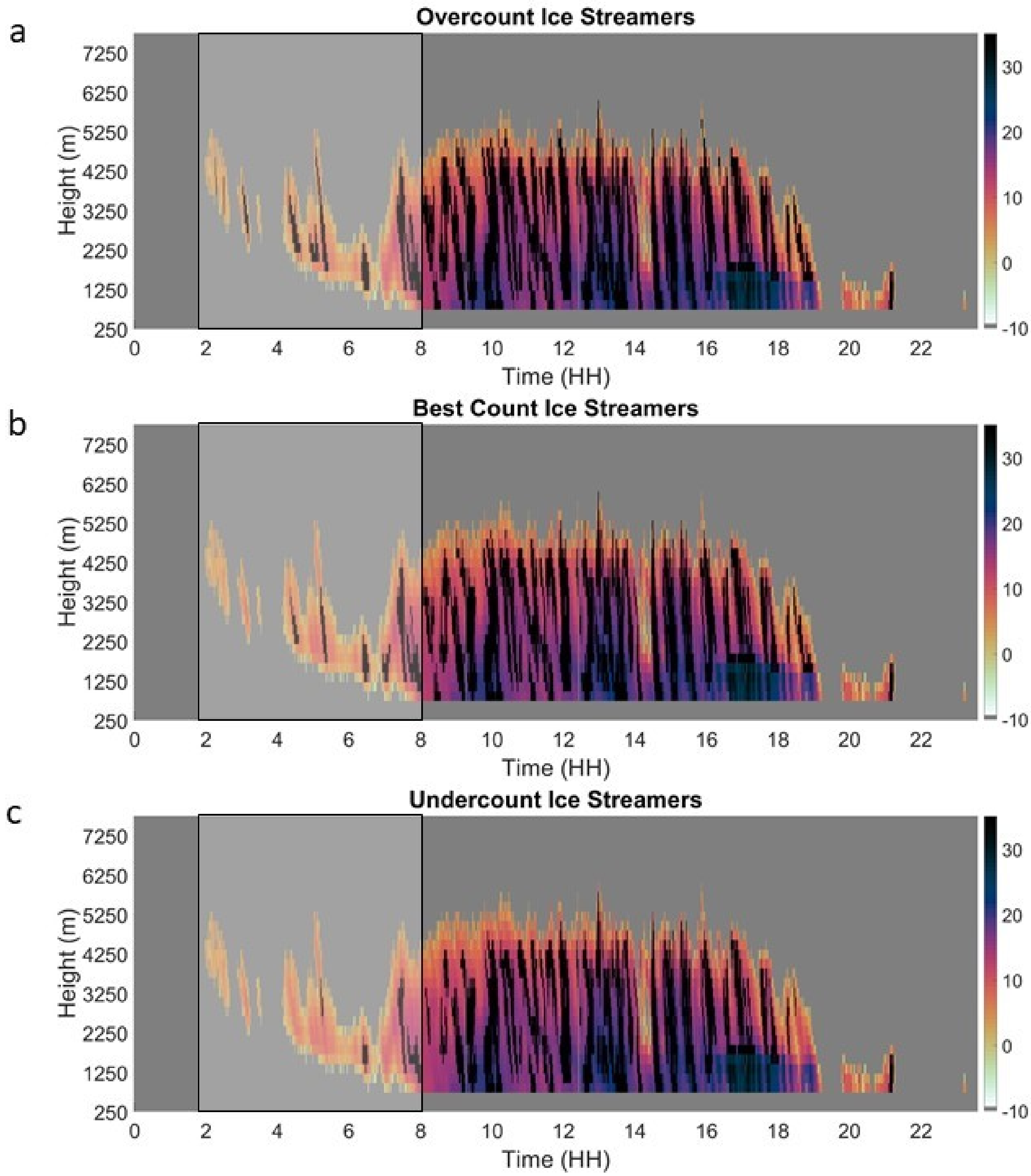

Figure 3.6: Ice streamer algorithm applied to an example day, 21 January 2012, for the overcount (a), best count (b), and undercount (c) methods. The ice streamers shown as black lines on the reflectivity image. Time is in UTC on the x-axis. The differences in the three filters is shown mostly clearly in the white semi-transparent box where the overcount method detects 8 ice streamers, best count 6 ice streamers, and undercount 4 ice streamers.

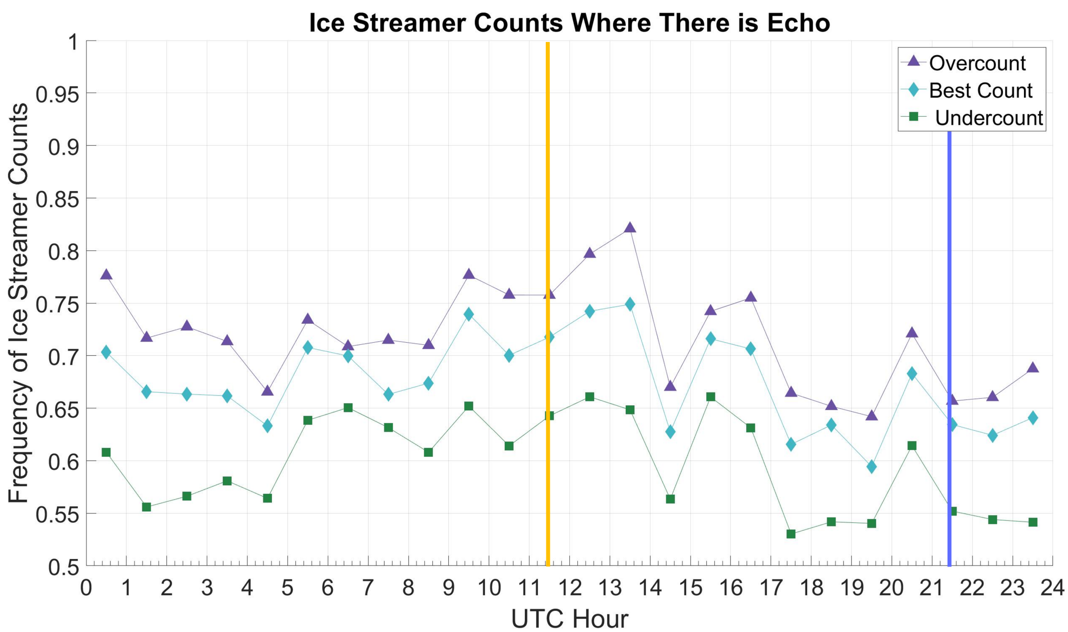

Figure 3.7: The ice streamer counts divided by instances of echo in each hour plotted for each counting method. The mean for the overcount frequency is 0.72, best count 0.67, and undercount is 0.60. Sunset is shown as the blue line at 2130 UTC and sunrise the solid orange line at 1130 UTC.

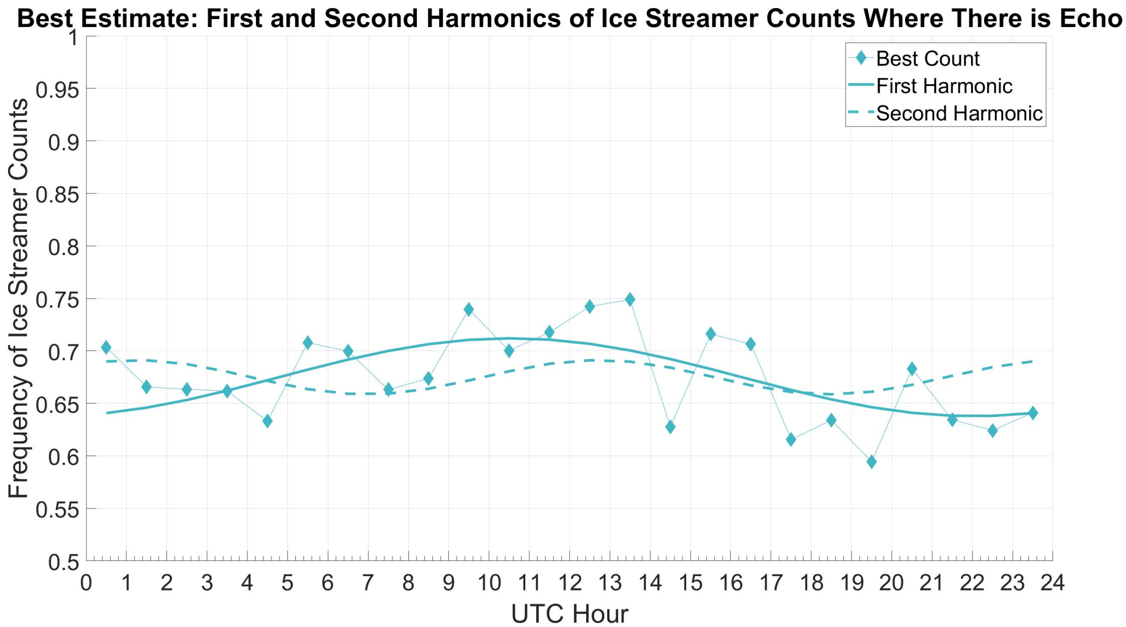

Figure 3.8: The sinusoidal fits for the first two harmonics are plotted against the best count method, shown as the blue diamonds.

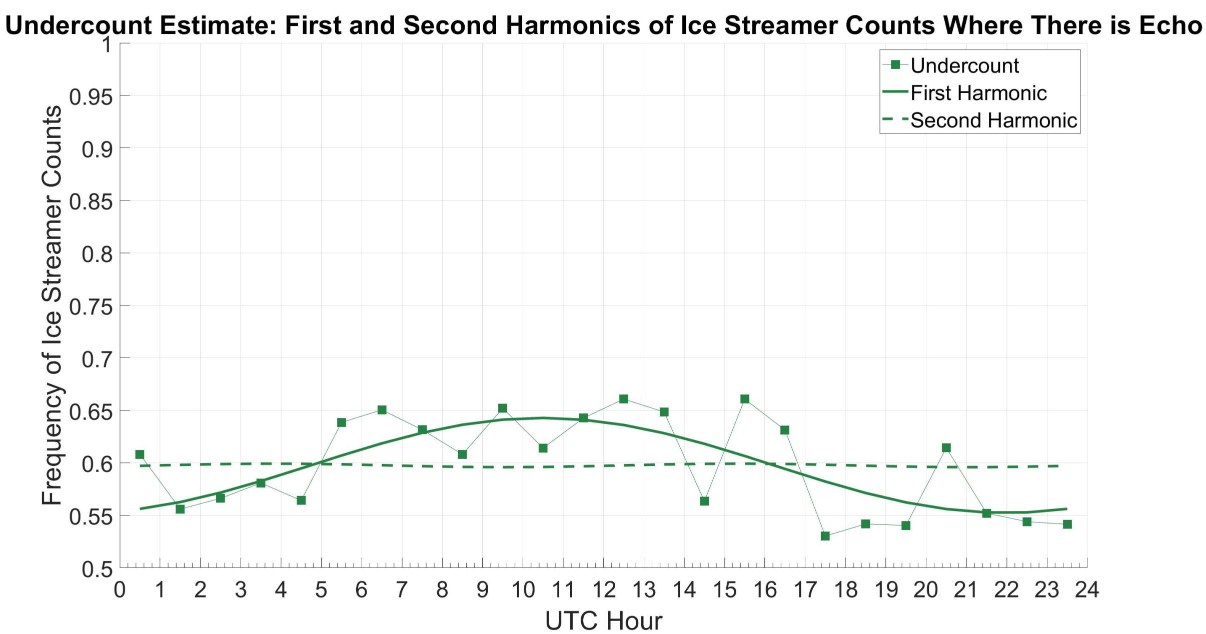

Figure 3.9: The sinusoidal fits for the first two harmonics are plotted against the low count method, shown as the green squares.

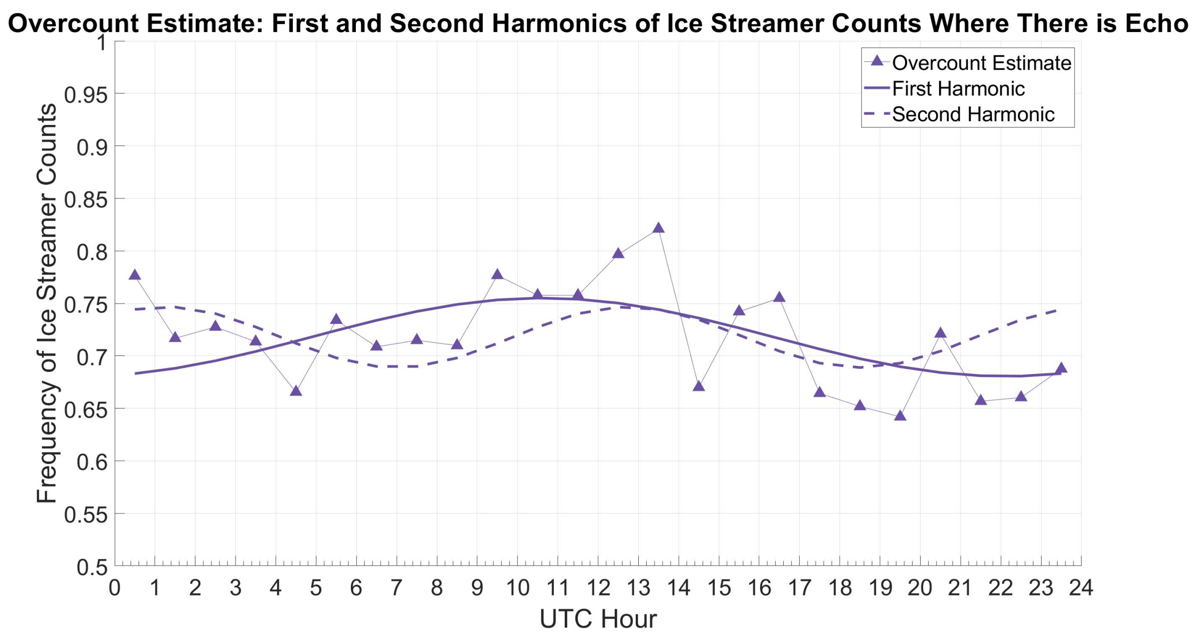

Figure 3.10: The sinusoidal fits for the first two harmonics are plotted against the overcount method, shown as the purple triangles.

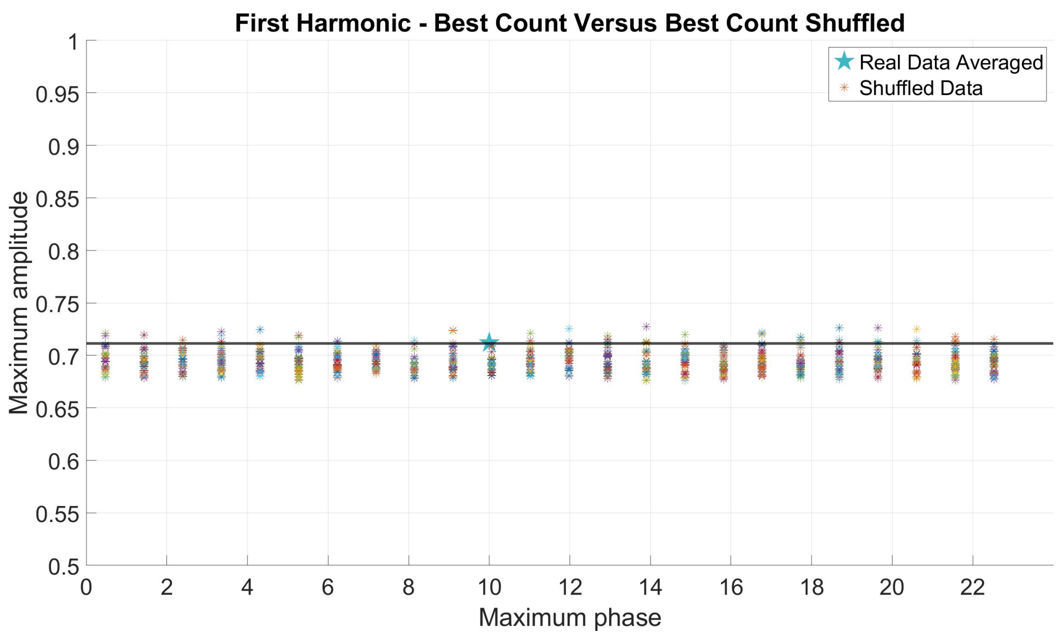

Figure 3.11: The maximum amplitude and phase of the first harmonic for the best count method (blue star), is plotted with the maximum amplitude of the first harmonic of the average of each iteration of Monte Carlo, colored asterisks. The 95$^{\text{th}}$ percentile of the shuffled amplitudes is plotted as the black line.

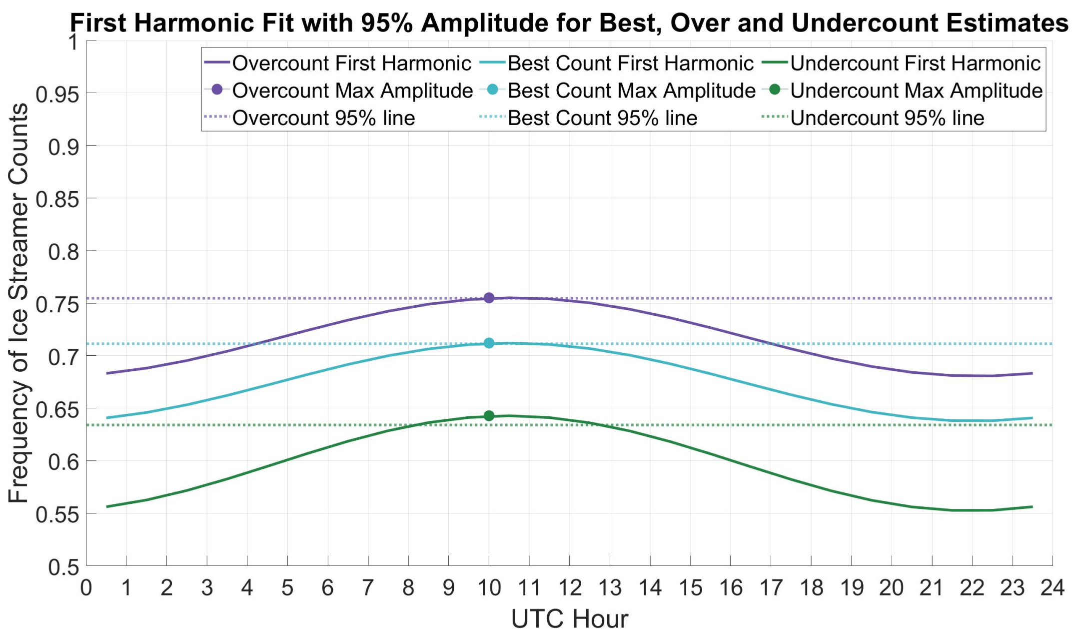

Figure 3.12: Summary of first harmonic fits to actual data and 95$^{\text{th}}$ percentiles from shuffled data for the overcount (purple), best count (blue), and undercount (green). The first harmonic of the observed data is shown for each method as a solid colored line. The maximum amplitude of the first harmonic of the observed data is plotted as a solid circle. The 95$^{\text{th}}$ percentile of the maximum amplitudes of each Monte Carlo iteration is shown as a dotted line.

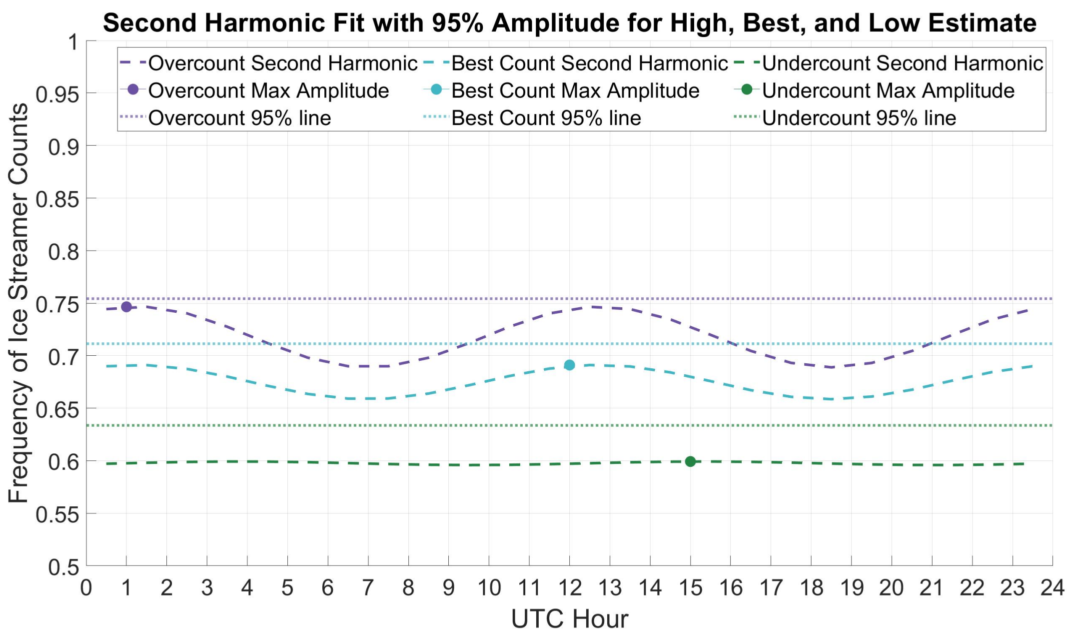

Figure 3.13: Summary of second harmonic fits to actual data and 95th percentiles from shuffled data for the overcount (purple), best count (blue), and undercount (green). The second harmonic of the observed data is shown for each method as a dashed colored line. The maximum amplitude and phase of the second harmonic of the observed data is plotted as a solid circle. The 95th percentile of the maximum amplitudes of each Monte Carlo iteration is shown as a dotted line.

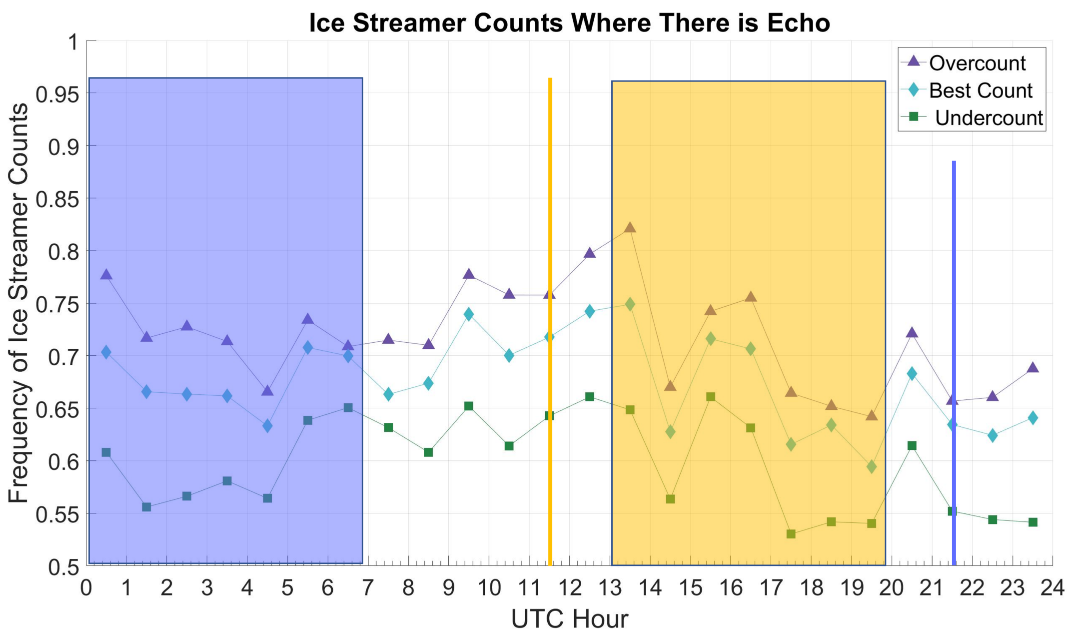

Figure 3.14: Time periods used for Test A- Day/Night version of 6-hour mean differences statistical test. Blue box corresponds to night period from 0 to 6 UTC (1900 to 0100 local time) and orange box corresponds to day period from 13 to 19 UTC (0800 to 1400 local time), Sunset is indicated by blue line at 2130 UTC and sunrise by orange line at 1130 UTC.

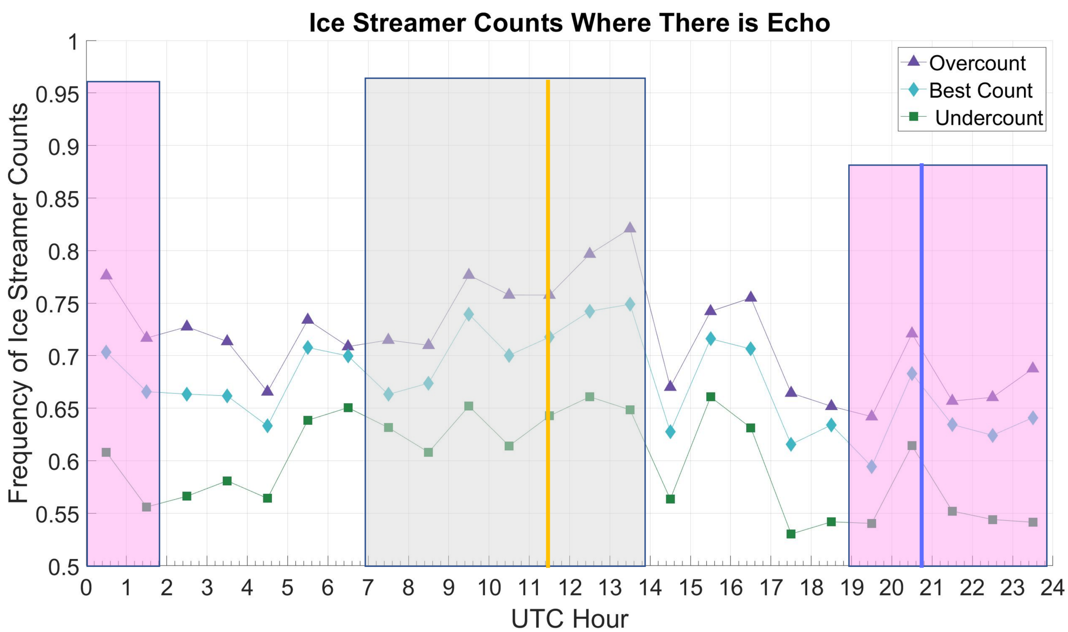

Figure 3.15: Time periods used for Test B version of 6-hour mean differences statistical test. Gray box corresponds to overnight to early morning period spanning sunrise from 7 to 13 UTC (0200 to 0800 local time) and pink box (in two parts) corresponds to late afternoon to early evening period spanning sunset from 19 to 01 UTC (1400 to 2000 local time). Sunset is indicated by blue line at 2130 UTC and sunrise by orange line at 1130 UTC.

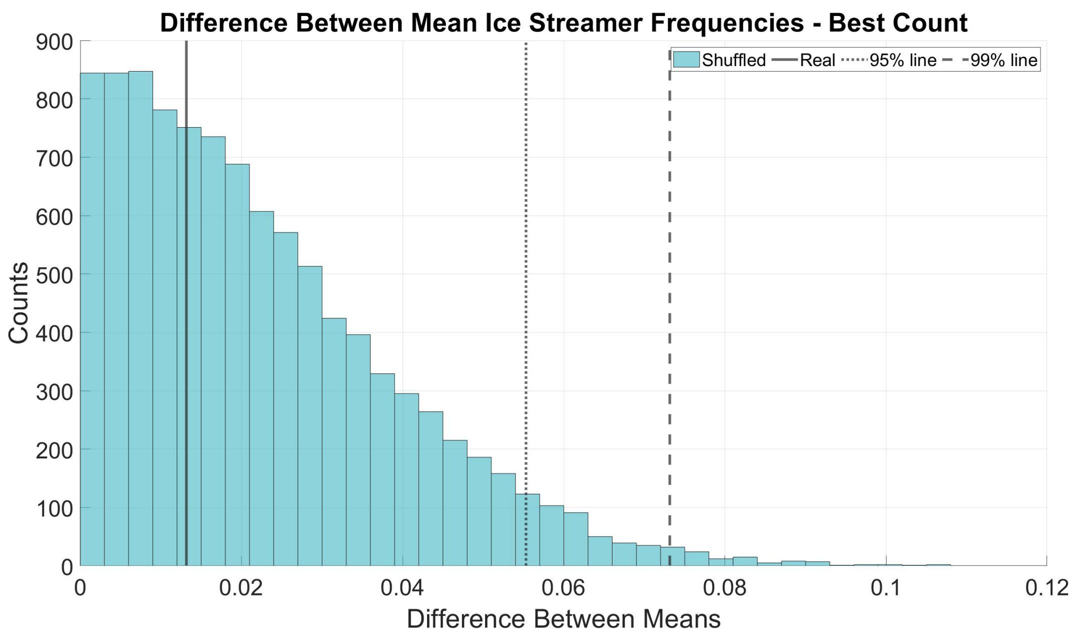

Figure 3.16: Test A - Day/Night best estimate distribution of the difference between the six hour mean for the day (13 to 19 UTC, 0800 to 1400 local time) and the 6 hour mean for the night (0 to 6 UTC, 1900 to 0100 local time) of the shuffled Monte Carlo data. The 95th percentile and 99th percentile of the differences are the dotted and dashed lines. The difference between the actual 6 hour mean for the day and 6 hour mean for the night of the observed data is the solid line.

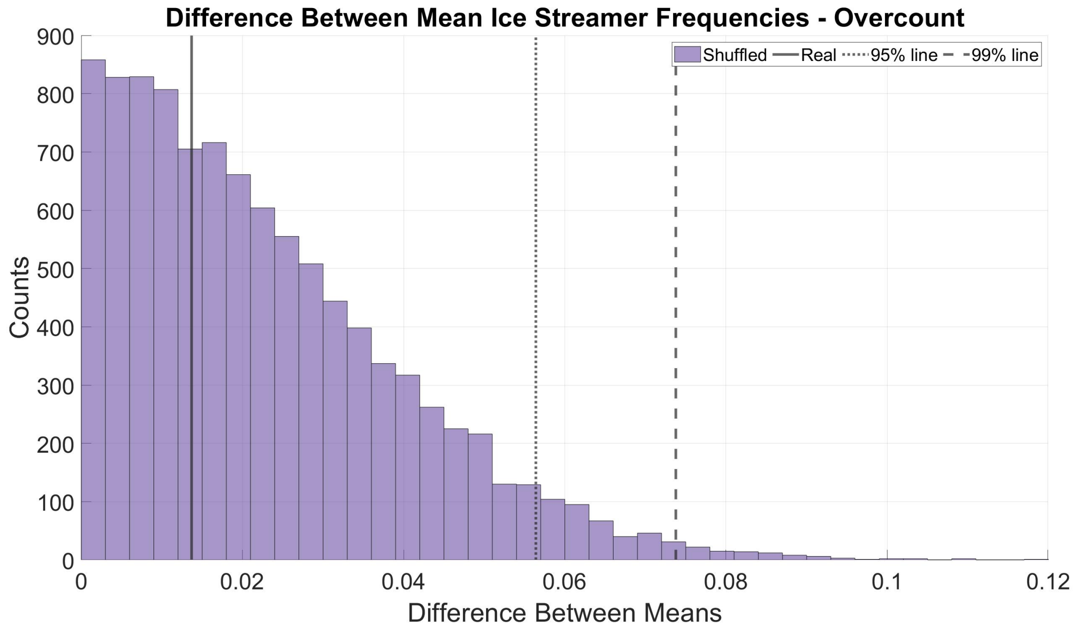

Figure 3.17: As in Fig. 3.16 except for Test A - Day/Night overcount estimate distribution.

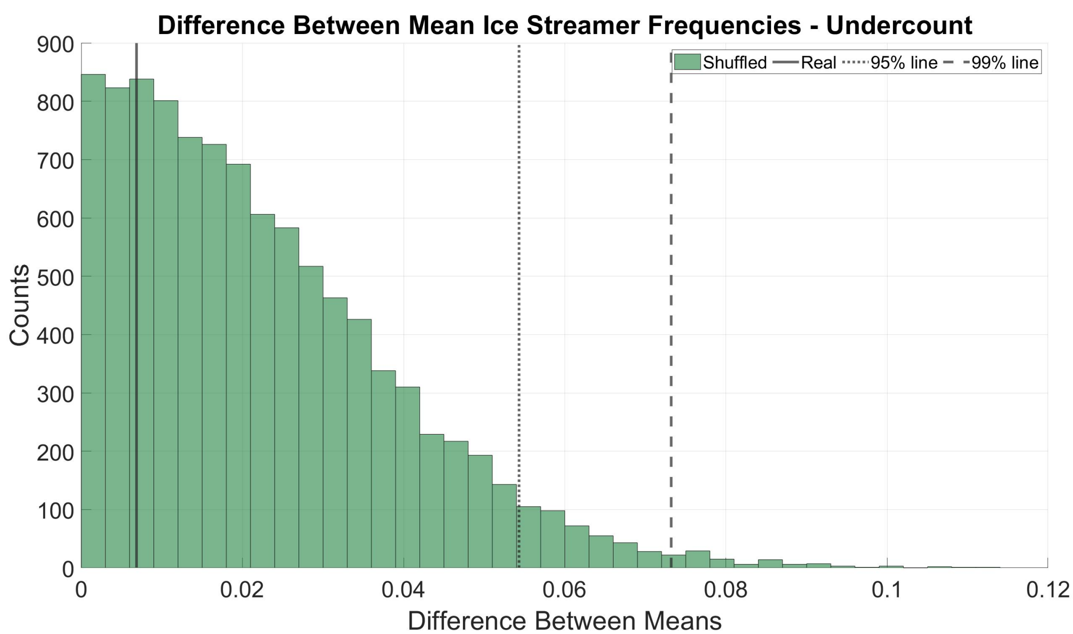

Figure 3.18: As in Fig. 3.16 except for Test A - Day/Night undercount estimate distribution.

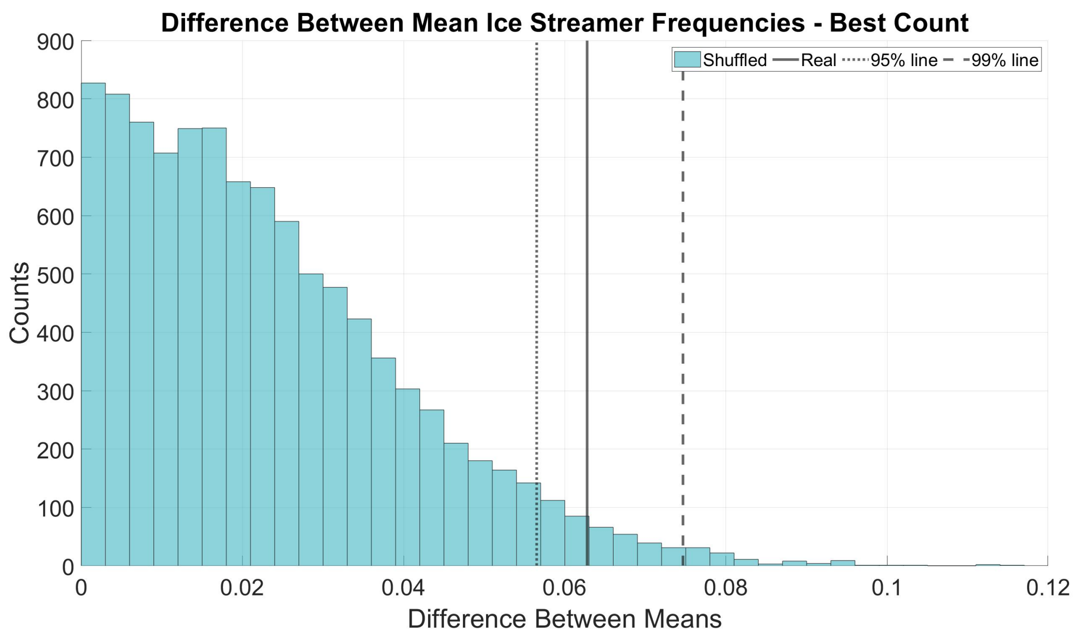

Figure 3.19: Test B - Sunrise/Sunset best estimate distribution of the difference between the six hour mean spanning sunrise (7 to 13 UTC, 0200 to 0800 local time) and the 6 hour mean spanning sunset (19 to 01 UTC, 1400 to 2000 local time) of the shuffled Monte Carlo data. The 95th percentile and 99th percentile of the differences are the dotted and dashed lines. The difference between the actual 6 hour mean spanning sunrise and 6 hour mean spanning sunset for the observed data is the solid line.

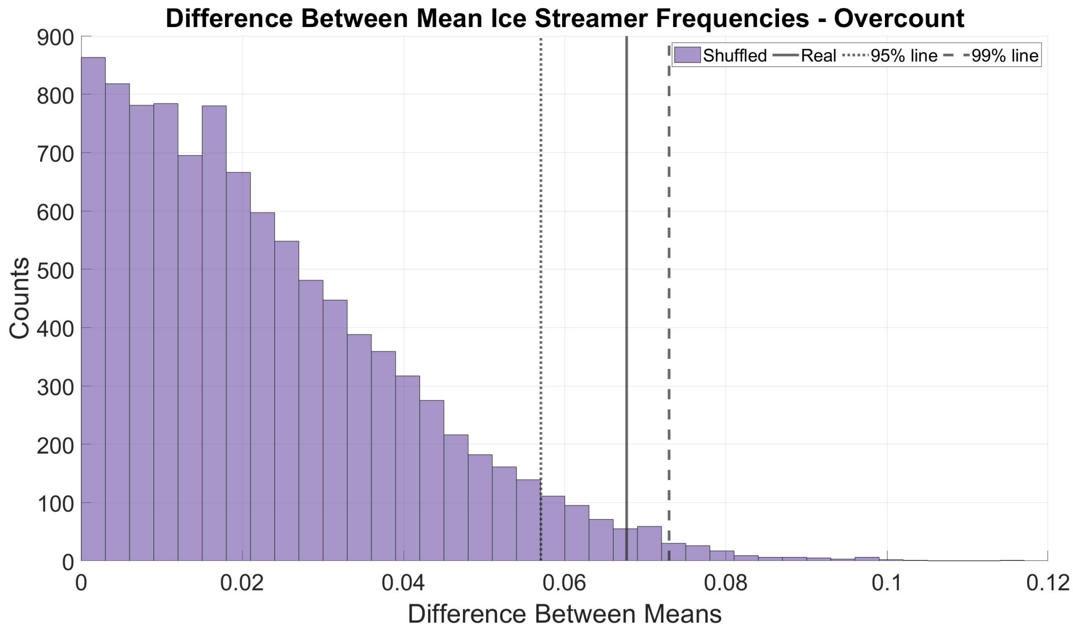

Figure 3.20: As in Fig. 3.19 except for Test B - Sunrise/Sunset overcount estimate distribution.

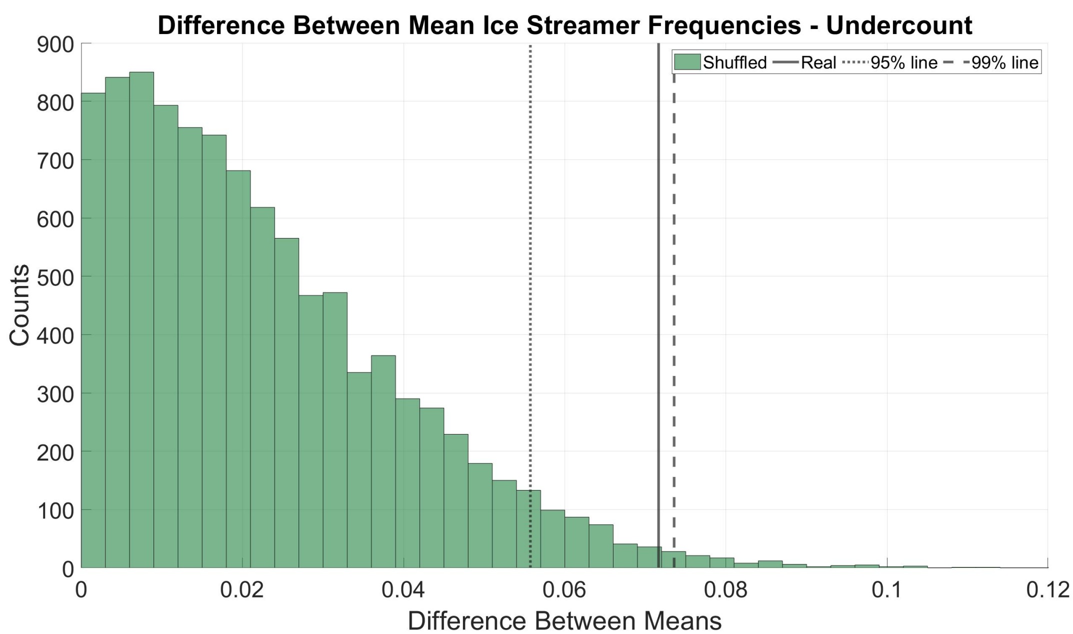

Figure 3.21: As in Fig. 3.19 except for Test B - Sunrise/Sunset undercount estimate distribution.

CHAPTER

4

CONCLUSIONS

4.1 Summary

4.1.1 Prevalence of Ice Streamers

Despite the many observational studies of winter season storms over the decades, prior to this analysis no one had systematically quantified the overall occurrence of generating cells or if there is a diurnal cycle in their frequency. As a proxy for generating cells, we use precipitation radar detectable ice streamers (ice trails from generating cells) which are sometimes referred to as fall streaks. This study aimed to quantify ice streamer prevalence within winter storms by examining a 10 year data set of vertically-pointing Micro Rain Radar data from Stony Brook, NY, a coastal site in northeast United States. After quality control steps, there were 14,877 hours of echo which was examined for ice streamers.

The localized regions of higher reflectivity associated with ice streamers are associated with locally higher snowfall rates compared to background reflectivity and background snowfall rates (Houze et al. 1981; Matejka et al. 1980; Herzegh and Hobbs 1980; Crosier et al. 2014; Evans et al. 2005; Plummer et al. 2014). The aircraft study of Plummer et al. (2014) found that ice water contents were 2 to 3 times larger inside as compared to outside of generating cells. The small spatial scales of generating cells, typically 1-3 km in horizontal and vertical extent (e.g. Gunn et al. 1954; Langleben 1956; Wexler and Atlas 1959; Syrett et al. 1995; Evans et al. 2005; Kumjian et al. 2014; Plummer et al. 2014; Rosenow et al. 2014; Rauber et al. 2015) means these features are not explicitly represented in NOAA and ECMWF global operational forecast models which currently have grid spacings of 28 km and 31 km respectively. The 3 km grid spacing of NOAA's HRRR regional model corresponds to the peak generating cell size found in literature. Regional mesoscale models would need to be run similar to Keeler et al.'s idealized runs with 100 m horizontal and 50 m vertical grid spacing to explicitly resolve the overturning circulations within generating cells.

The key findings of this study are that ice streamers occur about 67% of the time in winter storms at Stony Brook, NY and that there is weak evidence for a diurnal cycle of low amplitude in their occurrence. Since the vertically-pointing weather radar we use does not detect upper levels of cloud, the best estimate average ice streamer occurrence of 67% is likely an underestimate.

The 67% average prevalence of ice streamers in winter storms has several implications. Excluding representation of generating cells in forecast models will likely lead to decreased snowfall accumulations compared to including them. Additionally, the high average prevalence means there is not a lot room for increased frequency at a particular time of day.

4.1.2 Is There Clear Evidence of a Diurnal Cycle in Ice Streamers Related to Long Wave Cooling at Night?

In formulating the testable hypothesis for the NSF proposal that is examined in this study,

> ice streamers observed by vertically-pointing radar data are 2x more common at night when a cloud top radiative cooling instability is present than during the day,

it was presumed that ice streamers had a low enough average prevalence that a 2x frequency during the night as compared to during the day was possible. This hypothesis by the proposal PIs turned out to be incorrect.

Even for a process without any diurnal variation, real data will not show a perfectly uniform distribution over 24 hours. Figure 3.7 has a slight uptick in the frequency of ice streamers near dawn which is suggestive of a potential diurnal cycle. We examined the hourly frequency of occurrence of ice streamers using Monte Carlo 95$^{\text{th}}$ percentile significance tests on several metrics of the time series, harmonic fits and the differences between

6-hour averages and with three estimate of ice streamer frequency, best, overcount and undercount.

Harmonic fits are often used to establish the presence of a diurnal cycle (e.g. Wallace 1975). Harmonic fits applied to the ice streamer frequencies do not establish a practically significant diurnal cycle. Technically, the amplitudes of the first harmonic fits pass the 95^{th} percentile statistical test, but the magnitude of the amplitudes, < 5% (Table 3.1), is very small and seems inconsistent with discussion in the Keeler et al. papers of more vigorous generating cells overnight.

As an alternate method to assess a potential diurnal cycle, mean values of ice streamer frequencies were computed for 6-hour periods in day versus night and spanning sunrise versus spanning sunset and compared. It is unexpected that the detected differences in the diurnal cycle of practical significance are for the periods spanning sunrise versus spanning sunset as compared to the day to night differences since the Keeler et al. papers propose more convective overturning during the night as primarily a radiative cooling effect at cloud top. The radiative cooling effect at cloud top would be strongest overnight *before* sunrise, not spanning sunrise. The radiative balance at cloud top has a fast reaction to the start of SW fluxes at sunrise, likely no more than 10s of minutes. Keeler et al. contrasted day and night in their modeling studies but did not explore the sunrise and sunset transitions. Both observations and modeling over these transition periods are likely needed to unravel the relative importance of processes and feedbacks yielding generating cells near cloud top.

4.1.3 Potential Reasons for Differences from Keeler et al. Results

The testable hypothesis was motivated by the idealized modeling work of Keeler et al. (Keeler et al. 2016a,b, 2017), who examined the relative roles of different processes in the initiation and maintenance of generating cells near cloud top. They found that cloud-top radiative instability had a larger role than either diabatic heating or potential instability. Their comparisons of night-time longwave only to day-time longwave+shortwave conditions found stronger updrafts and higher precipitation ice mixing ratios at night. These differences are expected to yield notably higher frequencies of precipitation radar detectable ice streamers during the night as compared to the day.

The Keeler et al. idealized modeling is based on a storm observed on 14-15 February 2010 centered over Illinois and Indiana. In evaluating the fidelity of the model, Keeler et al. (2016a) compared to aircraft observations obtained at night to their nighttime radiation simulation and found reasonable correspondence. But the daytime radiation simulation was not similarly evaluated since no daytime observations were available for their modeled storm. Keeler et al. (2016b) examined the role of differential thermal advection and found that it stabilized the near cloud top layer in their particular modeled storm. But they caveated that they could not rule out differential thermal advection as a relevant source of destabilization in all cyclones.

Keeler et al. inferred that the stronger nighttime radiative instability was responsible for the stronger updrafts and ice precipitation mixing ratio in generating cells as compared to during the day. It is possible that the differences in their nighttime versus daytime radiation balances are larger than actual. Our study only counted ice streamers but was not able to assess their strength in terms of ice precipitation mixing ratio or vertical velocity. Since radar reflectivity is a function of number, size, density, and shape of snow particles, there are too many uncertainties to convert to a reliable snow water content.

Overall typical temperatures in winter season northeast coastal storms are higher as compared to those in the Midwest. The 8 km altitude cloud top heights in the Keeler et al. simulations are comparable to typical cloud top heights observed by cloud radar at Stony Brook, NY (M. Oue, personal communication). The average Micro Rain Radar echo top height is 4 km altitude. The average 4 km altitude temperature from winter season NWS soundings at Upton, NY (KOKX) is -12° C with a standard deviation of 7.5 deg C (K. Burris, personal communication). Within the shallow cloud portion of the 14-15 February 2010 storm modeled by Keeler et al., 3 km altitude temperatures were -21° C to -29° C (Rosenow et al. 2014). Equilibrium vapor pressure increases as temperature increases. For a given RH with respect to ice greater than 100%, particles can grow faster by vapor deposition at higher temperatures as compared to at lower temperatures. The lack of evidence for a diurnal cycle in ice streamers in a multi-year sample of observations from Stony Brook, NY may be because of a cloud top temperature sensitivity to the difference in generating cell strength in conditions of longwave versus longwave+shortware radiation. The cloud top temperature sensitivity of their findings was not addressed by Keeler et al. and could be explored in future idealized modeling studies.

4.2 Future Work

A key product of this analysis is a large sample size (almost 15,000 hours) of ice streamer occurrence within winter storms at Stony Brook, NY. This information can be used as context for existing operational observations to deduce further findings. The NWS operational upper air sounding at KOKX is ~20 km away from the Micro Rain Radar site at Stony Brook University. While the upper air soundings are usually only twice daily, over a 10+ year period with about 600 days of multi-hour continuous echo there are likely several hundred soundings within +/- 1 hour of storm echo that could be analyzed.

Information from thermodynamic profiles in the context of precipitation echo depth and the presence or absence of ice streamers will help to clarify the roles of different sources of instability to generating cells. Additionally, information from soundings can be used to deduce cloud top heights and temperatures which would complement information from the Micro Rain Radar. A better understanding of the thermodynamic conditions near storm top may lead to improved insights into precipitation ice processes in snow storms.

REFERENCES

American Meteorological Society (2021). Pseudoadiabatic lapse rate. Glossary of Meteorology.

Austin, P. M. and Bemis, A. C. (1950). A quantitative study of the "bright band" in radar precipitation echoes. *Journal of Atmospheric Sciences*, 7(2):145–151.

Beauducel, F. (2021). Harmfit: Sinusoidal harmonic curve fitting.

BIPM, IEC, IFCC, ILAC, ISO, IUPAC, IUPAP, and OIML (2020). *Guide to the expression of uncertainty in measurement — Part 6: Developing and using measurement models.* Joint Committee for Guides in Metrology.

Collier, J. C. and Bowman, K. P. (2004). Diurnal cycle of tropical precipitation in a general circulation model. *Journal of Geophysical Research: Atmospheres*, 109(D17).

Crosier, J., Choularton, T., Westbrook, C., Blyth, A., Bower, K., Connolly, P., Dearden, C., Gallagher, M., Cui, Z., and Nicol, J. (2014). Microphysical properties of cold frontal rainbands. *Quarterly Journal of the Royal Meteorological Society*, 140(681):1257–1268.

Dai, A., Giorgi, F., and Trenberth, K. E. (1999). Observed and model-simulated diurnal cycles of precipitation over the contiguous united states. *Journal of Geophysical Research: Atmospheres*, 104(D6):6377–6402.

Dixon, M. and Wiener, G. (1993). Titan: Thunderstorm identification, tracking, analysis, and nowcasting—a radar-based methodology. *Journal of atmospheric and oceanic technology*, 10(6):785–797.

Douglas, R. H., Gunn, K. L. S., and Marshall, J. S. (1957). Pattern in the vertical of snow generation. *Journal of the Atmospheric Sciences*, 14(2):95–114. Publisher: American Meteorological Society Section: Journal of the Atmospheric Sciences.

Endries, J., Perry, L. B., Yuter, S. E., Seimon, A., Andrade-Flores, M., Winkelmann, R., N. Quispe, M. R., Montoya, N., Velarde, F., and Arias, S. (2018). Radar observed characteristics of precipitation in the tropical high andes of southern peru and bolivia. *Journal of Applied Meteorology and Climatology*, 57(7):1441 – 1458.

Evans, A. G., Locatelli, J. D., Stoelinga, M. T., and Hobbs, P. V. (2005). The IMPROVE-1 Storm of 1–2 February 2001. Part II: Cloud Structures and the Growth of Precipitation. *Journal of the Atmospheric Sciences*, 62(10):3456–3473. Publisher: American Meteorological Society Section: Journal of the Atmospheric Sciences.

Federal Emergency Management Agency (2021). Declared disasters.

Gunn, K. L. S., Langleben, M. P., Dennis, A. S., and Power, B. A. (1954). Radar evidence of a generating level for snow. *Journal of the Atmospheric Sciences*, 11(1):20–26. Publisher: American Meteorological Society Section: Journal of the Atmospheric Sciences.

Herzegh, P. H. and Hobbs, P. V. (1980). The mesoscale and microscale structure and organization of clouds and precipitation in midlatitude cyclones. ii: Warm-frontal clouds. *Journal of Atmospheric Sciences*, 37(3):597–611.

Houze, R. A., Rutledge, S. A., Matejka, T. J., and Hobbs, P. V. (1981). The mesoscale and microscale structure and organization of clouds and precipitation in midlatitude cyclones. iii: Air motions and precipitation growth in a warm-frontal rainband. *Journal of Atmospheric Sciences*, 38(3):639–649.

Keeler, J. M., Jewett, B. F., Rauber, R. M., McFarquhar, G. M., Rasmussen, R. M., Xue, L., Liu, C., and Thompson, G. (2016a). Dynamics of cloud-top generating cells in winter cyclones. part i: Idealized simulations in the context of field observations. *Journal of the Atmospheric Sciences*, 73(4):1507–1527.

Keeler, J. M., Jewett, B. F., Rauber, R. M., McFarquhar, G. M., Rasmussen, R. M., Xue, L., Liu, C., and Thompson, G. (2016b). Dynamics of cloud-top generating cells in winter cyclones. part ii: Radiative and instability forcing. *Journal of the Atmospheric Sciences*, 73(4):1529–1553. Publisher: American Meteorological Society Section: Journal of the Atmospheric Sciences.

Keeler, J. M., Rauber, R. M., Jewett, B. F., McFarquhar, G. M., Rasmussen, R. M., Xue, L., Liu, C., and Thompson, G. (2017). Dynamics of cloud-top generating cells in winter cyclones. part iii: Shear and convective organization. *Journal of the Atmospheric Sciences*, 74(9):2879–2897.

Kober, K. and Tafferner, A. (2009). Tracking and nowcasting of convective cells using remote sensing data from radar and satellite. *Meteorologische Zeitschrift*, 1:75–84.

Kumjian, M. R., Rutledge, S. A., Rasmussen, R. M., Kennedy, P. C., and Dixon, M. (2014). High-resolution polarimetric radar observations of snow-generating cells. *Journal of Applied Meteorology and Climatology*, 53(6):1636–1658. Publisher: American Meteorological Society Section: Journal of Applied Meteorology and Climatology.

Langleben, M. P. (1956). The plan pattern of snow echoes at the generating level. *Journal of the Atmospheric Sciences*, 13(6):554–560. Publisher: American Meteorological Society Section: Journal of the Atmospheric Sciences.

Lerche, I. and Mudford, B. S. (2005). How many monte carlo simulations does one need to do? *Energy exploration & exploitation*, 23(6):405–427.

Maahn, M. and Kollias, P. (2012). Improved micro rain radar snow measurements using doppler spectra post-processing. *Atmospheric Measurement Techniques*, 5(11):2661–2673.

Mallafré, M. C., Ribas, T. R., Botija, M. d. C. L., and Sánchez, J. L. (2009). Improving hail identification in the ebro valley region using radar observations: Probability equations and warning thresholds. *Atmospheric research*, 93(1-3):474–482.

Marshall, J. S. (1953). Precipitation trajectories and patterns. *Journal of the Atmospheric Sciences*, 10(1):25–29. Publisher: American Meteorological Society Section: Journal of the Atmospheric Sciences.

Matejka, T. J., Houze Jr, R. A., and Hobbs, P. V. (1980). Microphysics and dynamics of clouds associated with mesoscale rainbands in extratropical cyclones. *Quarterly Journal of the Royal Meteorological Society*, 106(447):29–56.

MATLAB Regionprops function (2020). Matlab regionprops function. The MathWorks, Natick, MA, USA.

Matrosov, S. Y. (2007). Modeling Backscatter Properties of Snowfall at Millimeter Wavelengths. *Journal of the Atmospheric Sciences*, 64(5):1727–1736. Publisher: American Meteorological Society.

METEK (2017). Micro-rain-radar mrr-2 and mrr-pro a tutorial. METEK.

Ni, X., Liu, C., Cecil, D. J., and Zhang, Q. (2017). On the detection of hail using satellite passive microwave radiometers and precipitation radar. *Journal of Applied Meteorology and Climatology*, 56(10):2693–2709.

NOAA (2021). Noaa solar calculator. Earth System Research Laboratories.

North, B. V., Curtis, D., and Sham, P. C. (2002). A note on the calculation of empirical p values from monte carlo procedures. *American journal of human genetics*, 71(2):439.

Peters, G., Fischer, B., Münster, H., Clemens, M., and Wagner, A. (2005). Profiles of raindrop size distributions as retrieved by microrain radars. *Journal of applied meteorology*, 44(12):1930–1949.

Plummer, D. M., McFarquhar, G. M., Rauber, R. M., Jewett, B. F., and Leon, D. C. (2014). Structure and statistical analysis of the microphysical properties of generating cells in the comma head region of continental winter cyclones. *Journal of the Atmospheric Sciences*, 71(11):4181–4203. Publisher: American Meteorological Society Section: Journal of the Atmospheric Sciences.

Plummer, D. M., McFarquhar, G. M., Rauber, R. M., Jewett, B. F., and Leon, D. C. (2015). Microphysical properties of convectively generated fall streaks within the stratiform comma head region of continental winter cyclones. *Journal of the Atmospheric Sciences*, 72(6):2465–2483.

Rasmussen, R., Dixon, M., Vasiloff, S., Hage, F., Knight, S., Vivekanandan, J., and Xu, M. (2003). Snow Nowcasting Using a Real-Time Correlation of Radar Reflectivity with Snow Gauge Accumulation. *Journal of Applied Meteorology and Climatology*, 42(1):20–36. Publisher: American Meteorological Society Section: Journal of Applied Meteorology and Climatology.

Rauber, R. M., Macomber, M. K., Plummer, D. M., Rosenow, A. A., McFarquhar, G. M., Jewett, B. F., Leon, D., and Keeler, J. M. (2014). Finescale radar and airmass structure of the comma head of a continental winter cyclone: The role of three airstreams. *Monthly Weather Review*, 142(11):4207–4229. Publisher: American Meteorological Society Section: Monthly Weather Review.

Rauber, R. M., Plummer, D. M., Macomber, M. K., Rosenow, A. A., McFarquhar, G. M., Jewett, B. F., Leon, D., Owens, N., and Keeler, J. M. (2015). The role of cloud-top generating cells and boundary layer circulations in the finescale radar structure of a winter cyclone over the great lakes. *Monthly Weather Review*, 143(6):2291–2318.

Rosenow, A. A., Plummer, D. M., Rauber, R. M., McFarquhar, G. M., Jewett, B. F., and Leon, D. (2014). Vertical velocity and physical structure of generating cells and convection in the comma head region of continental winter cyclones. *Journal of the Atmospheric Sciences*, 71(5):1538–1558.

Schultz, D. M., Bosart, L. F., Colle, B. A., Davies, H. C., Dearden, C., Keyser, D., Martius, O., Roebber, P. J., Steenburgh, W. J., Volkert, H., and Winters, A. C. (2019). Extratropical Cyclones: A Century of Research on Meteorology Centerpiece. *Meteorological Monographs*, 59(1):16.1–16.56. Publisher: American Meteorological Society Section: Meteorological Monographs.

Skripniková, K. and Řezáčová, D. (2014). Radar-based hail detection. *Atmospheric Research*, 144:175–185.

Syrett, W. J., Albrecht, B. A., and Clothiaux, E. E. (1995). Vertical cloud structure in a midlatitude cyclone from a 94-ghz radar. *Monthly Weather Review*, 123(12):3393–3407. Publisher: American Meteorological Society Section: Monthly Weather Review.

Wallace, J. M. (1975). Diurnal variations in precipitation and thunderstorm frequency over the conterminous united states. *Monthly Weather Review*, 103(5):406–419.

Warren, R. A. and Protat, A. (2019). Should interpolation of radar reflectivity be performed in z or db z? *Journal of Atmospheric and Oceanic Technology*, 36(6):1143–1156.

Wexler, R. (1955). Radar analysis of precipitation streamers observed 25 february 1954. *Journal of the Atmospheric Sciences*, 12(4):391–393. Publisher: American Meteorological Society Section: Journal of the Atmospheric Sciences.

Wexler, R. and Atlas, D. (1959). Precipitation generating cells. *Journal of the Atmospheric Sciences*, 16(3):327–332. Publisher: American Meteorological Society Section: Journal of the Atmospheric Sciences.

Wood, R., Bretherton, C., Leon, D., Clarke, A., Zuidema, P., Allen, G., and Coe, H. (2011). An aircraft case study of the spatial transition from closed to open mesoscale cellular convection over the southeast pacific. *Atmospheric Chemistry and Physics*, 11(5):2341–2370.

Yuter, S. E., Houze, R. A., Smith, E. A., Wilheit, T. T., and Zipser, E. (2005). Physical characterization of tropical oceanic convection observed in kwajex. *Journal of Applied Meteorology and Climatology*, 44(4):385–415.

APPENDIX

APPENDIX

A

ADDITIONAL FIGURES

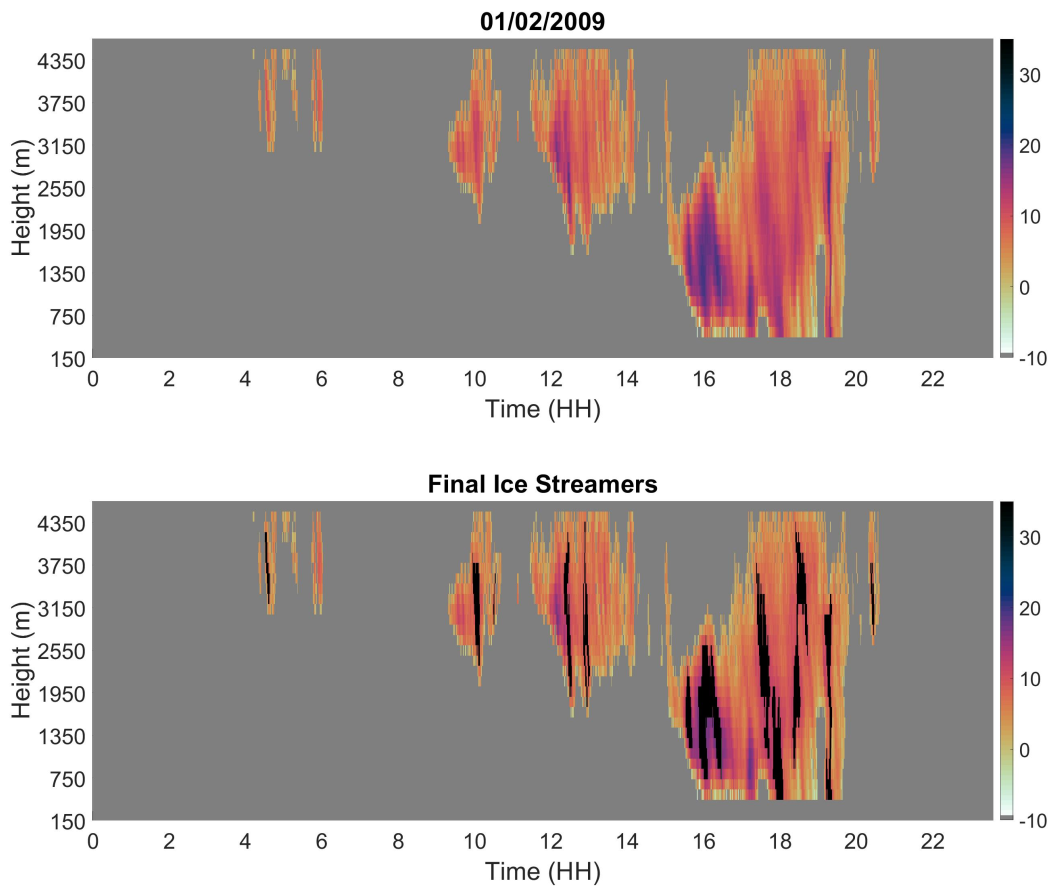

Figure A.1: Test case for ice streamer algorithm testing from a winter storm at Stony Brook, NY on 01/02/2009. (top) input radar reflectivity in dBZ, (bottom) reflectivity with identified ice streamers shown in black.

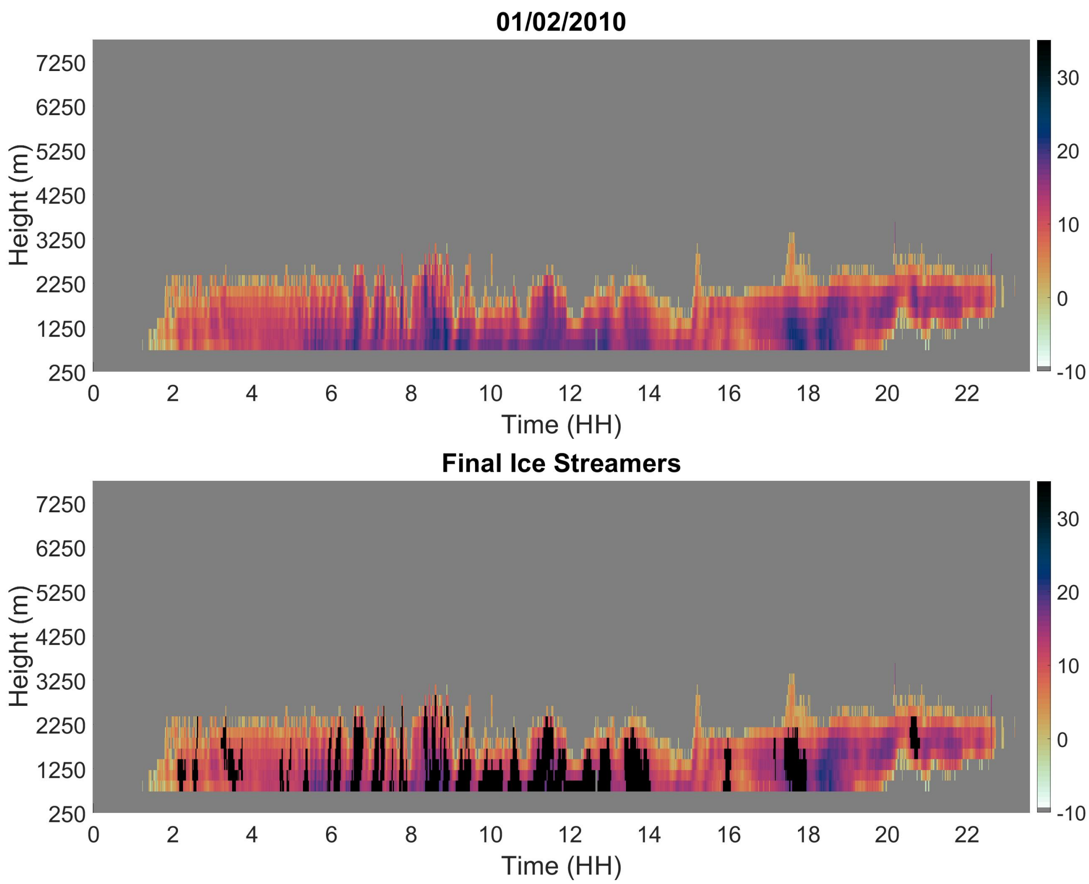

Figure A.2: Test case for ice streamer algorithm testing from a winter storm at Stony Brook, NY on 01/02/2010. (top) input radar reflectivity in dBZ, (bottom) reflectivity with identified ice streamers shown in black.

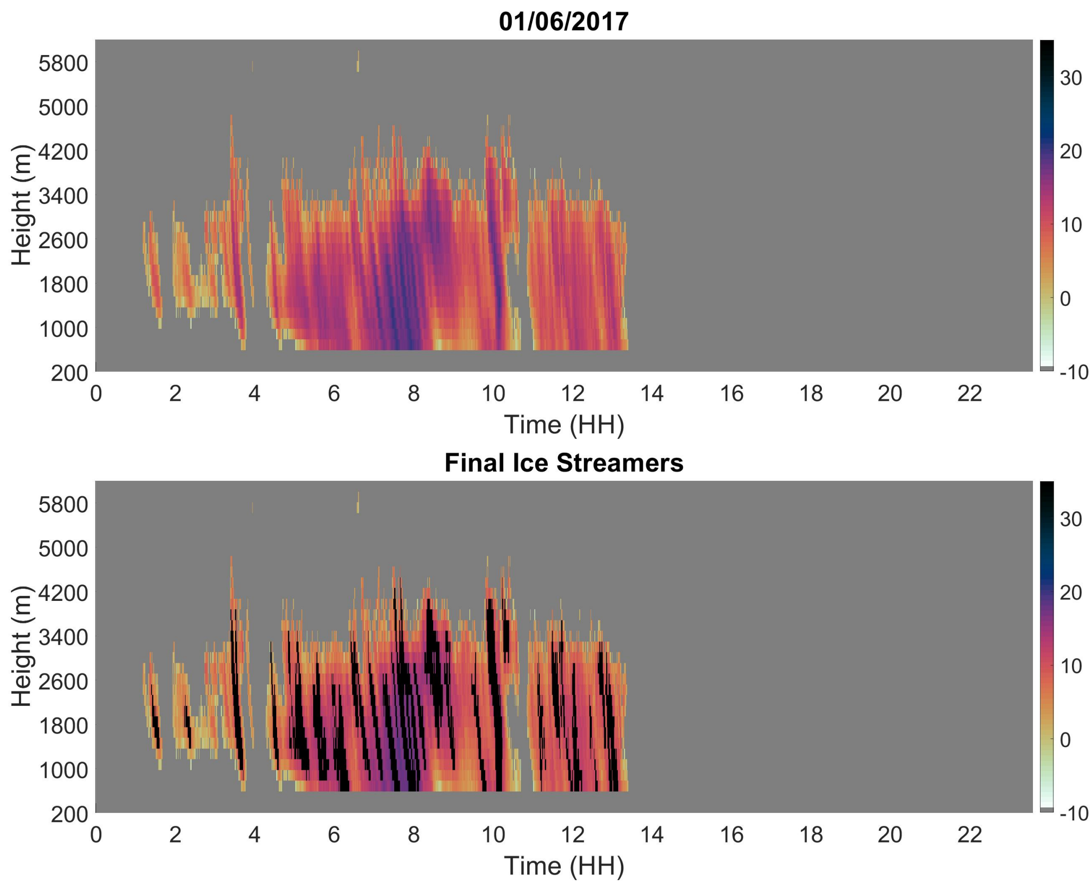

Figure A.3: Test case for ice streamer algorithm testing from a winter storm at Stony Brook, NY on 01/06/2017. (top) input radar reflectivity in dBZ, (bottom) reflectivity with identified ice streamers shown in black.

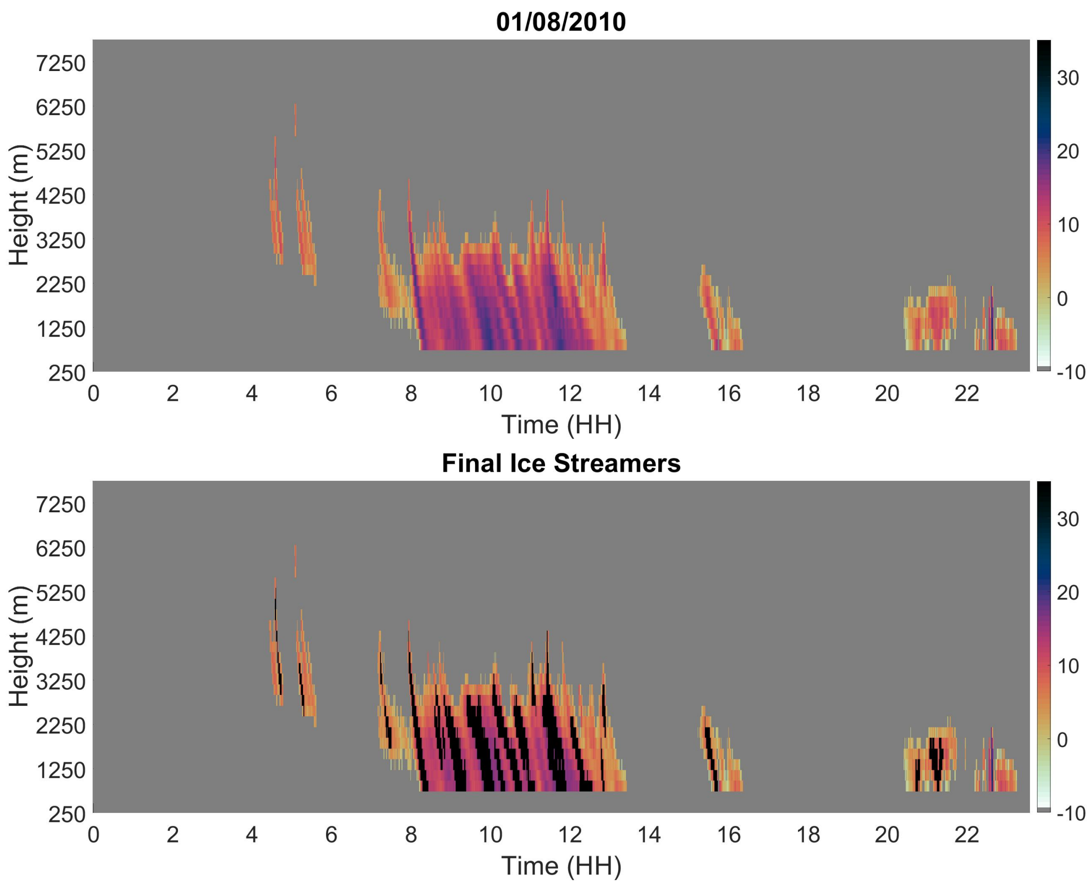

Figure A.4: Test case for ice streamer algorithm testing from a winter storm at Stony Brook, NY on 01/08/2010. (top) input radar reflectivity in dBZ, (bottom) reflectivity with identified ice streamers shown in black.

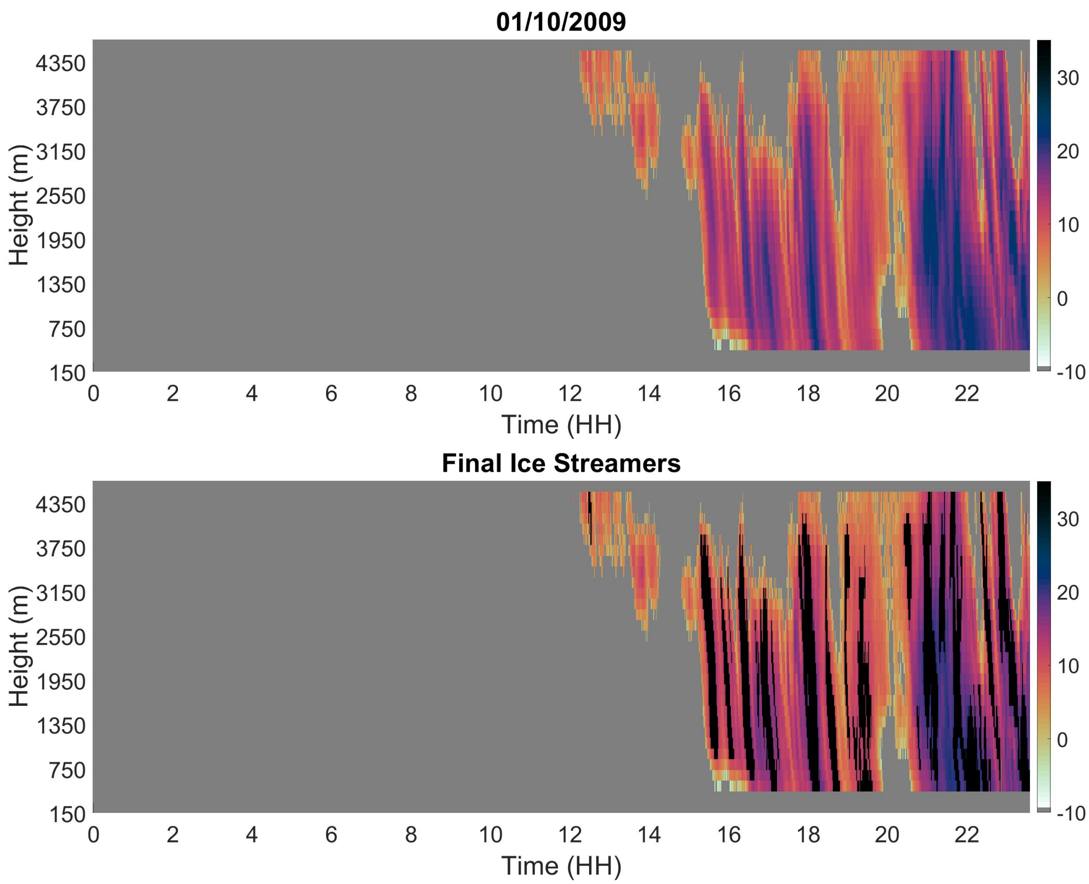

Figure A.5: Test case for ice streamer algorithm testing from a winter storm at Stony Brook, NY on 01/10/2009. (top) input radar reflectivity in dBZ, (bottom) reflectivity with identified ice streamers shown in black.

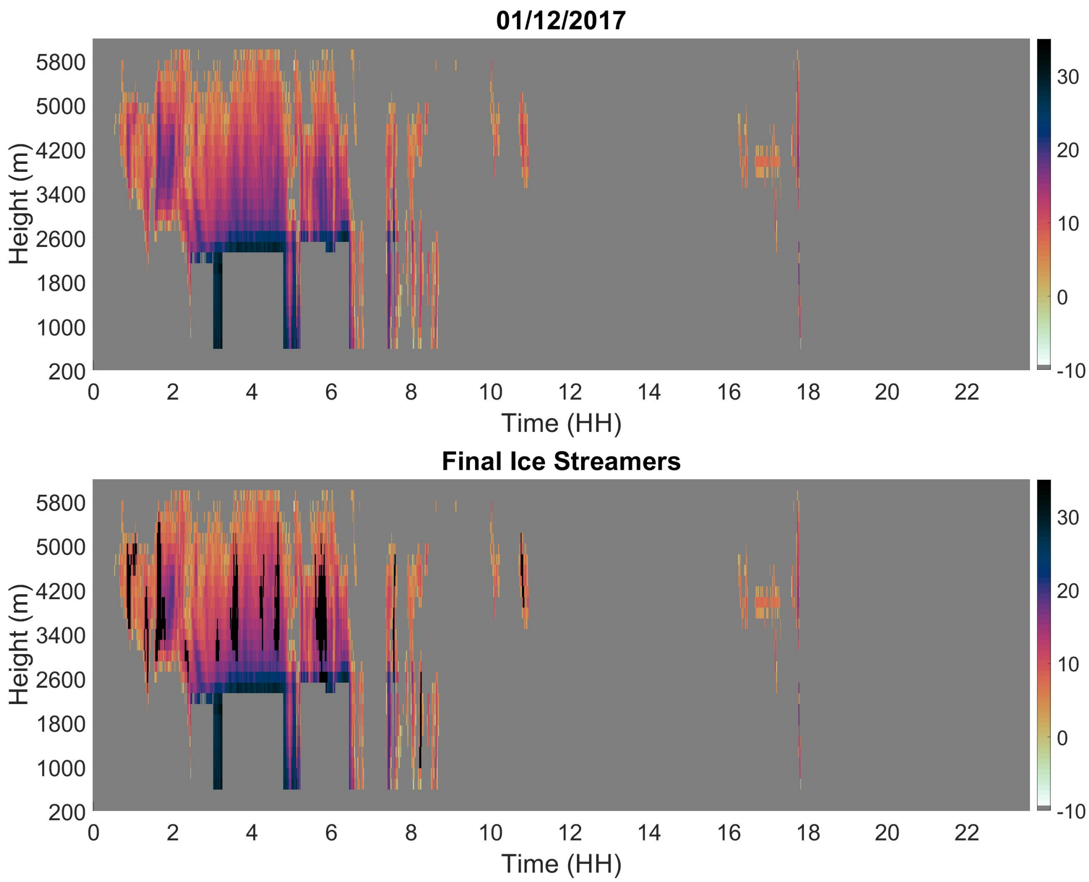

Figure A.6: Test case for ice streamer algorithm testing from a winter storm at Stony Brook, NY on 01/12/2017. (top) input radar reflectivity in dBZ, (bottom) reflectivity with identified ice streamers shown in black.

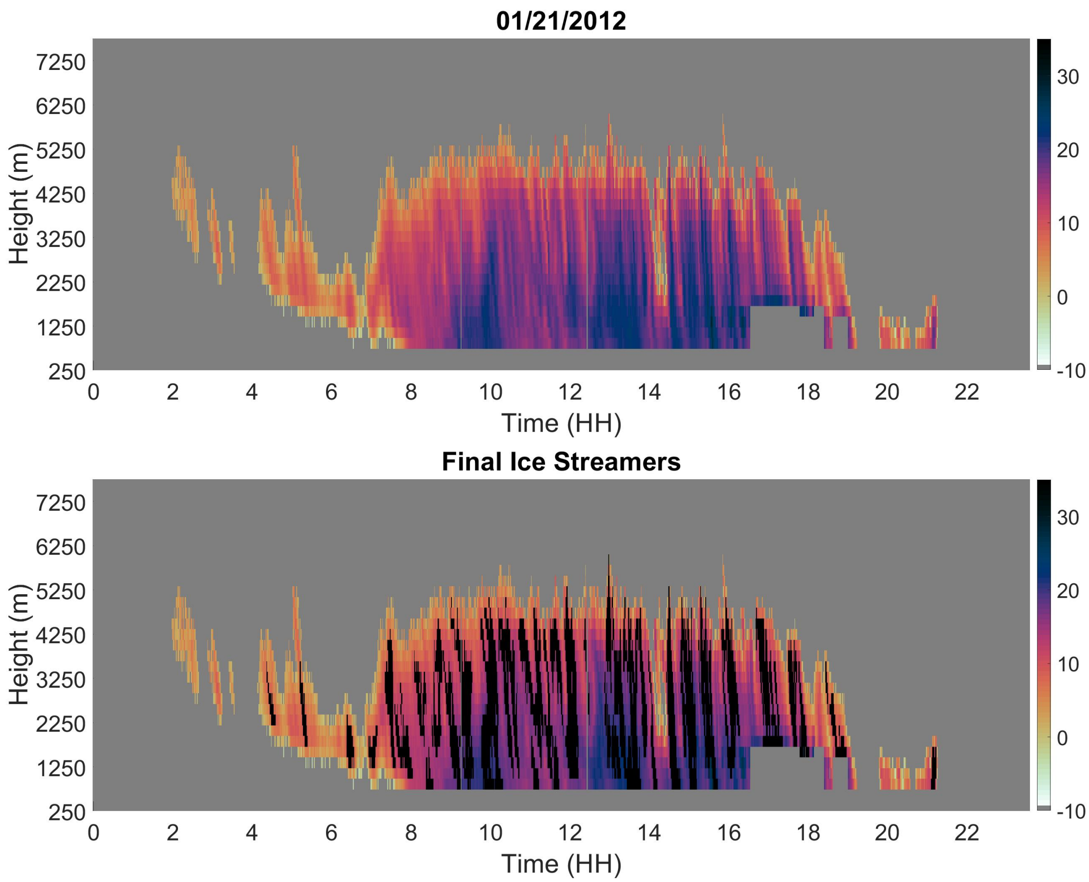

Figure A.7: Test case for ice streamer algorithm testing from a winter storm at Stony Brook, NY on 01/21/2012. (top) input radar reflectivity in dBZ, (bottom) reflectivity with identified ice streamers shown in black.

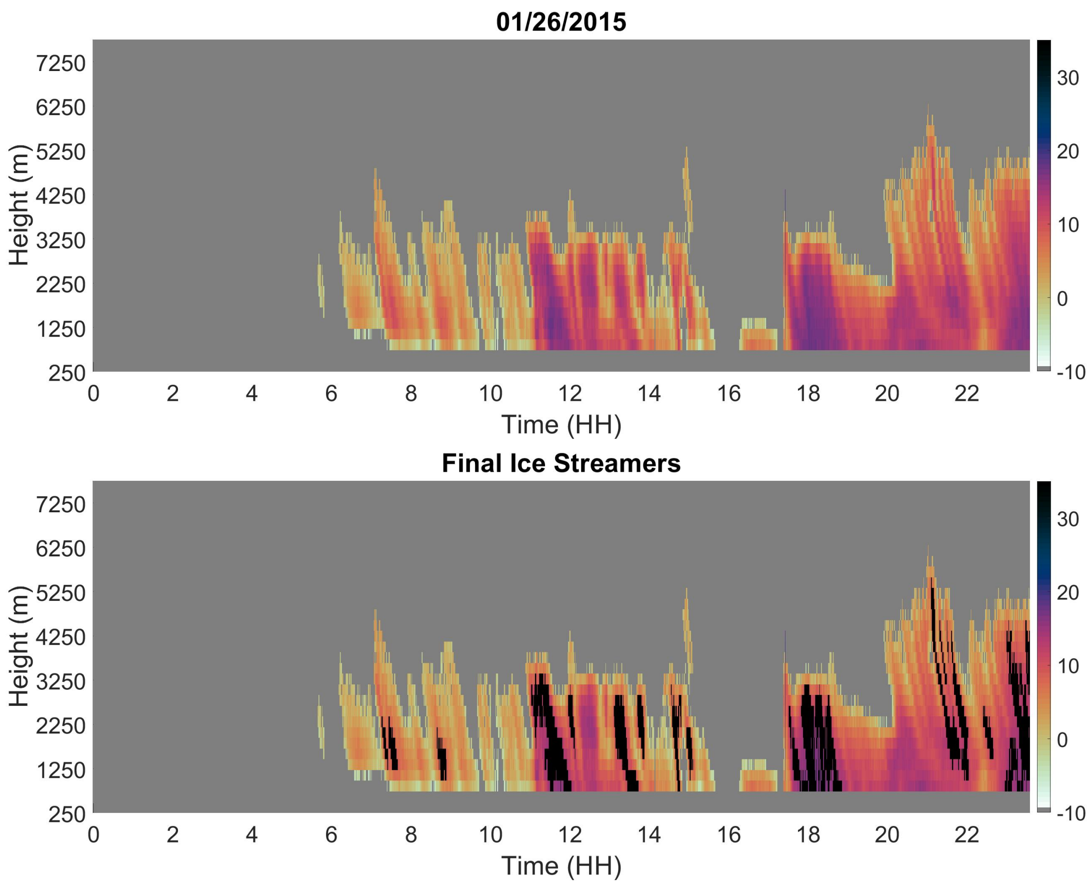

Figure A.8: Test case for ice streamer algorithm testing from a winter storm at Stony Brook, NY on 01/26/2015. (top) input radar reflectivity in dBZ, (bottom) reflectivity with identified ice streamers shown in black.

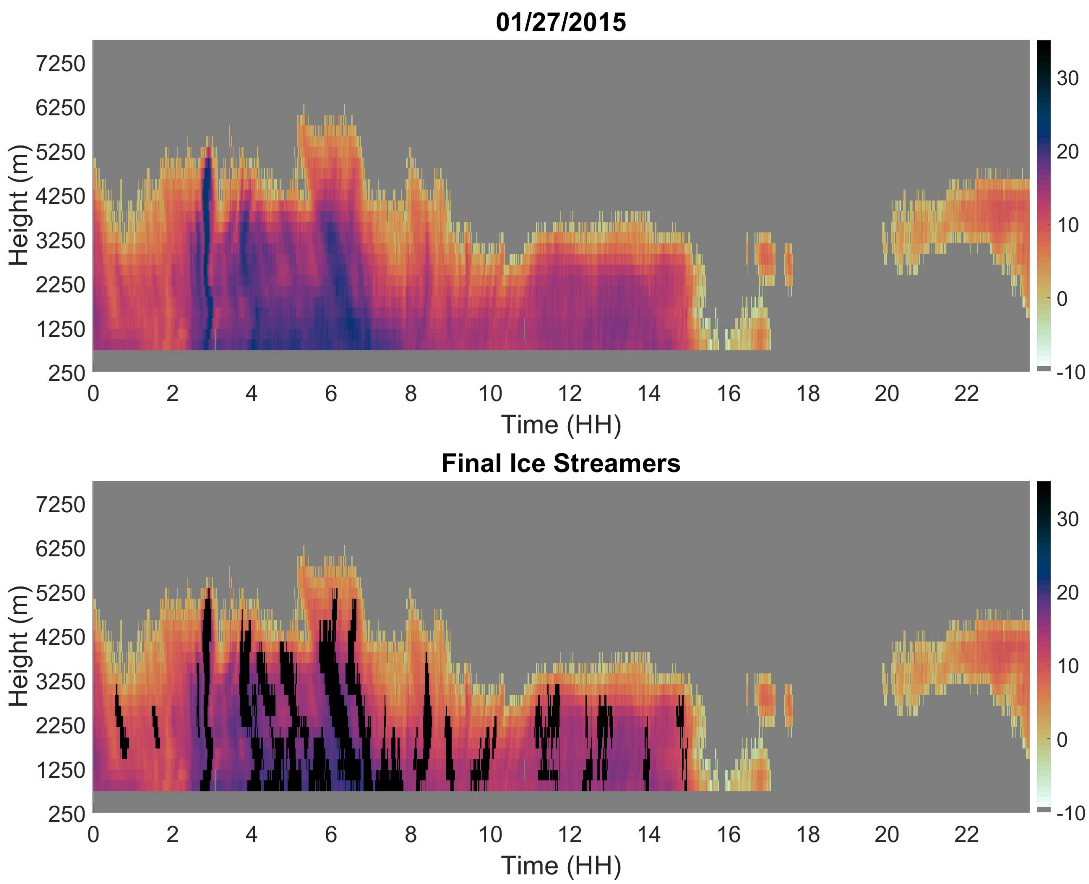

Figure A.9: Test case for ice streamer algorithm testing from a winter storm at Stony Brook, NY on 01/27/2015. (top) input radar reflectivity in dBZ, (bottom) reflectivity with identified ice streamers shown in black.

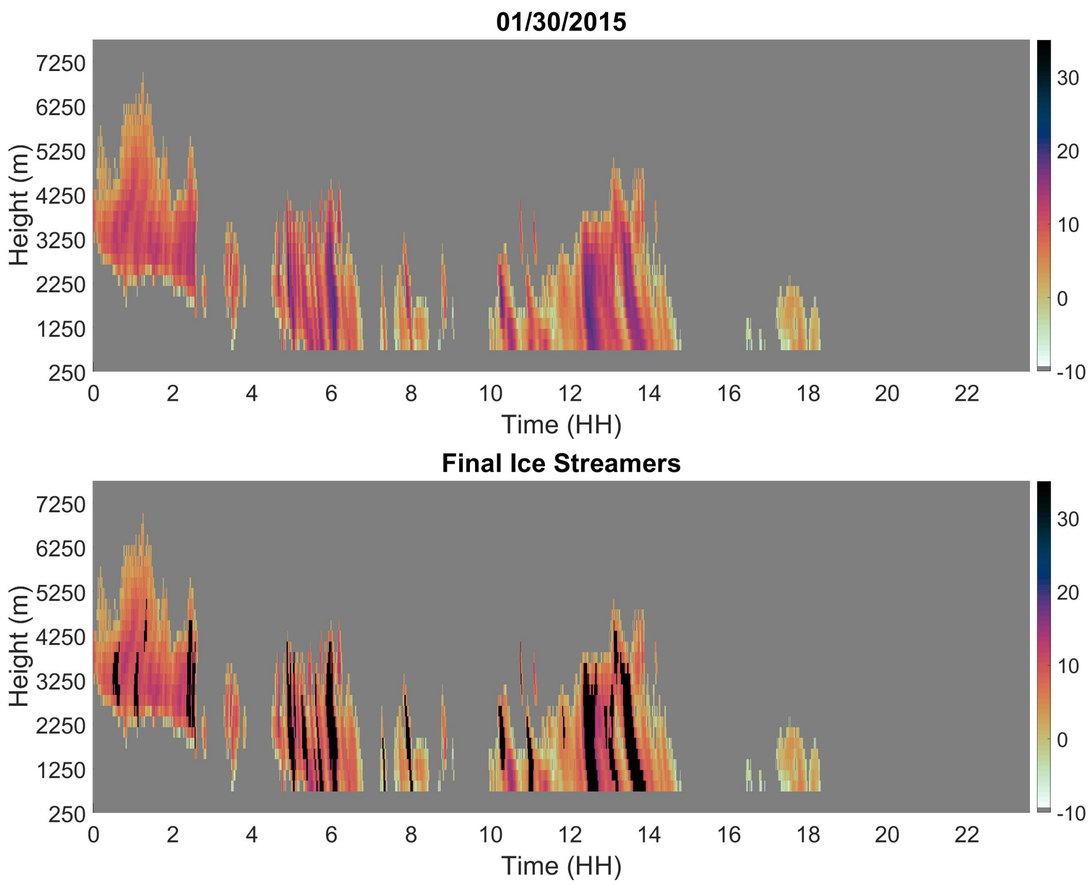

Figure A.10: Test case for ice streamer algorithm testing from a winter storm at Stony Brook, NY on 01/30/2015. (top) input radar reflectivity in dBZ, (bottom) reflectivity with identified ice streamers shown in black.

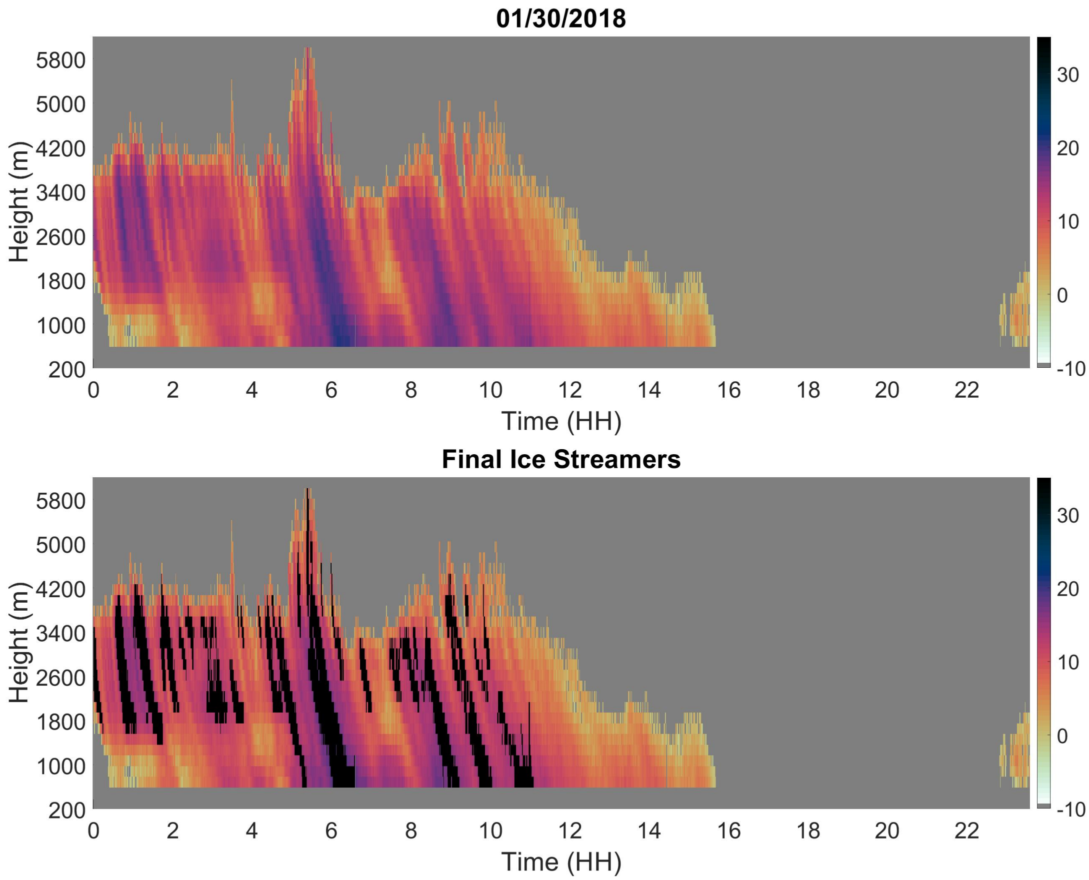

Figure A.11: Test case for ice streamer algorithm testing from a winter storm at Stony Brook, NY on 01/30/2018. (top) input radar reflectivity in dBZ, (bottom) reflectivity with identified ice streamers shown in black.

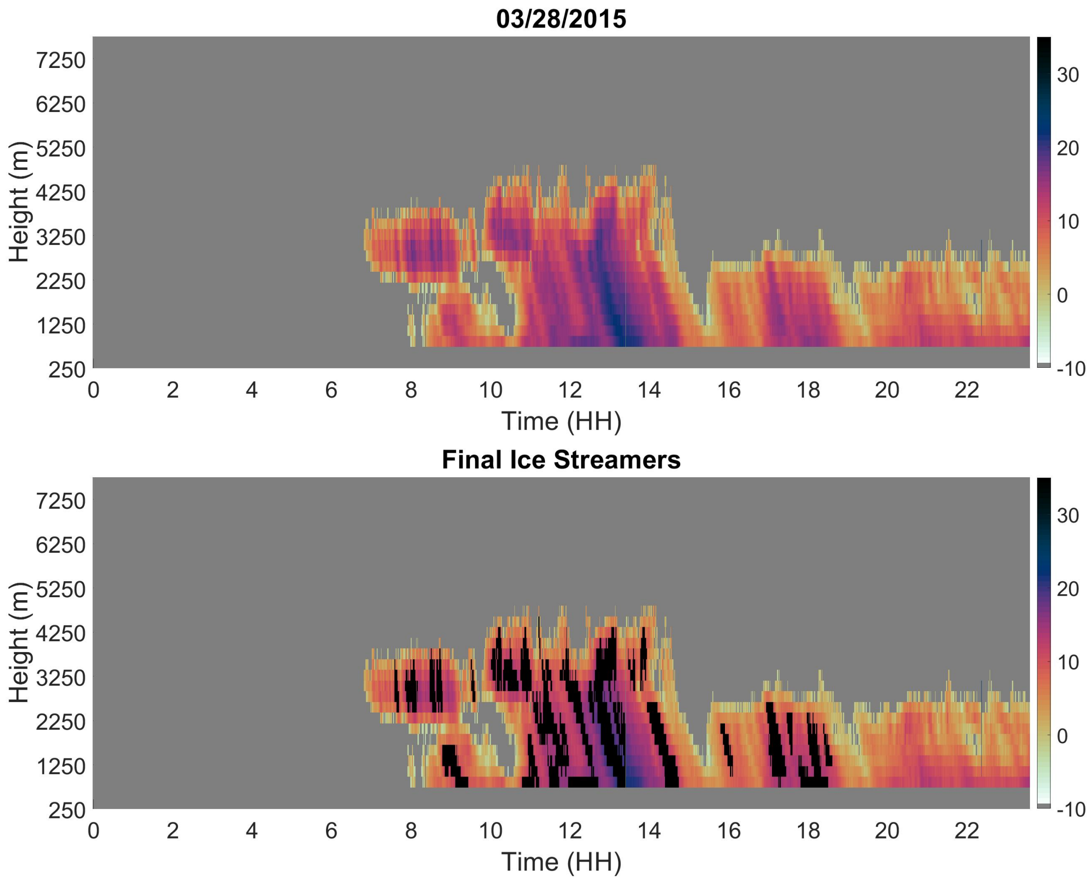

Figure A.12: Test case for ice streamer algorithm testing from a winter storm at Stony Brook, NY on 03/28/2015. (top) input radar reflectivity in dBZ, (bottom) reflectivity with identified ice streamers shown in black.

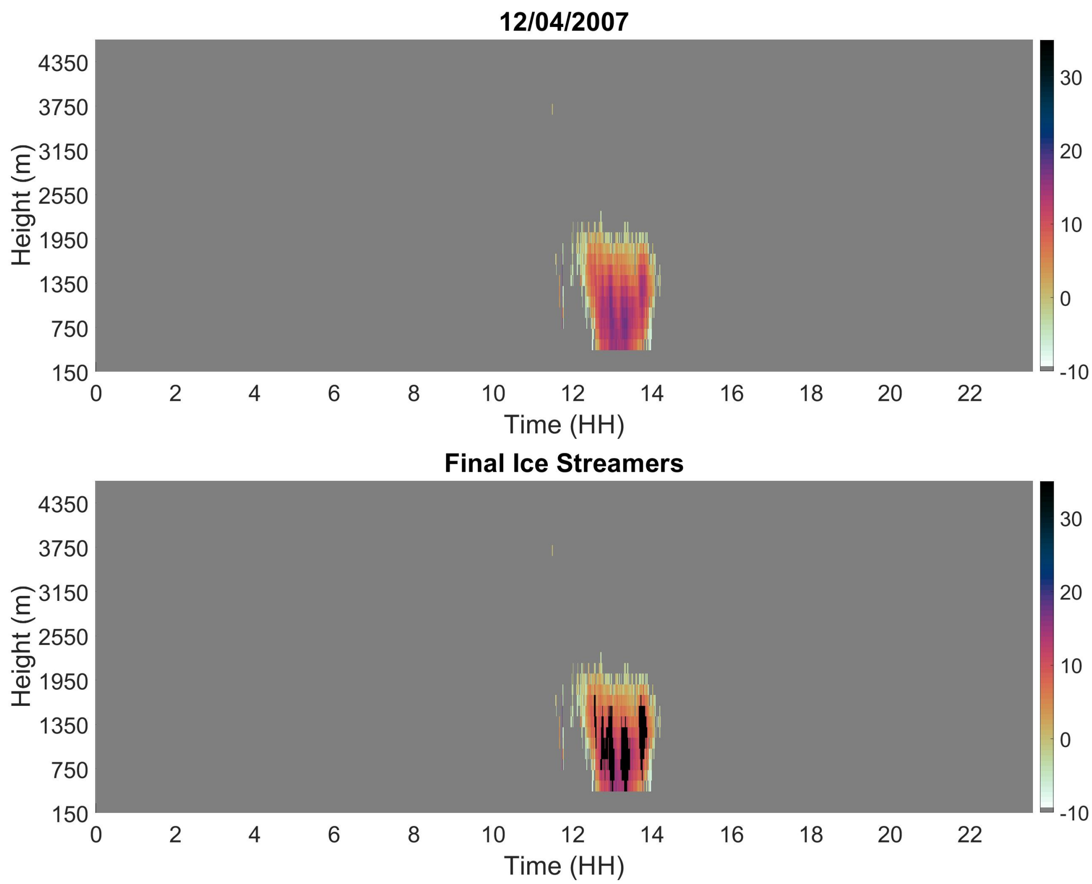

Figure A.13: Test case for ice streamer algorithm testing from a winter storm at Stony Brook, NY on 12/04/2007. (top) input radar reflectivity in dBZ, (bottom) reflectivity with identified ice streamers shown in black.

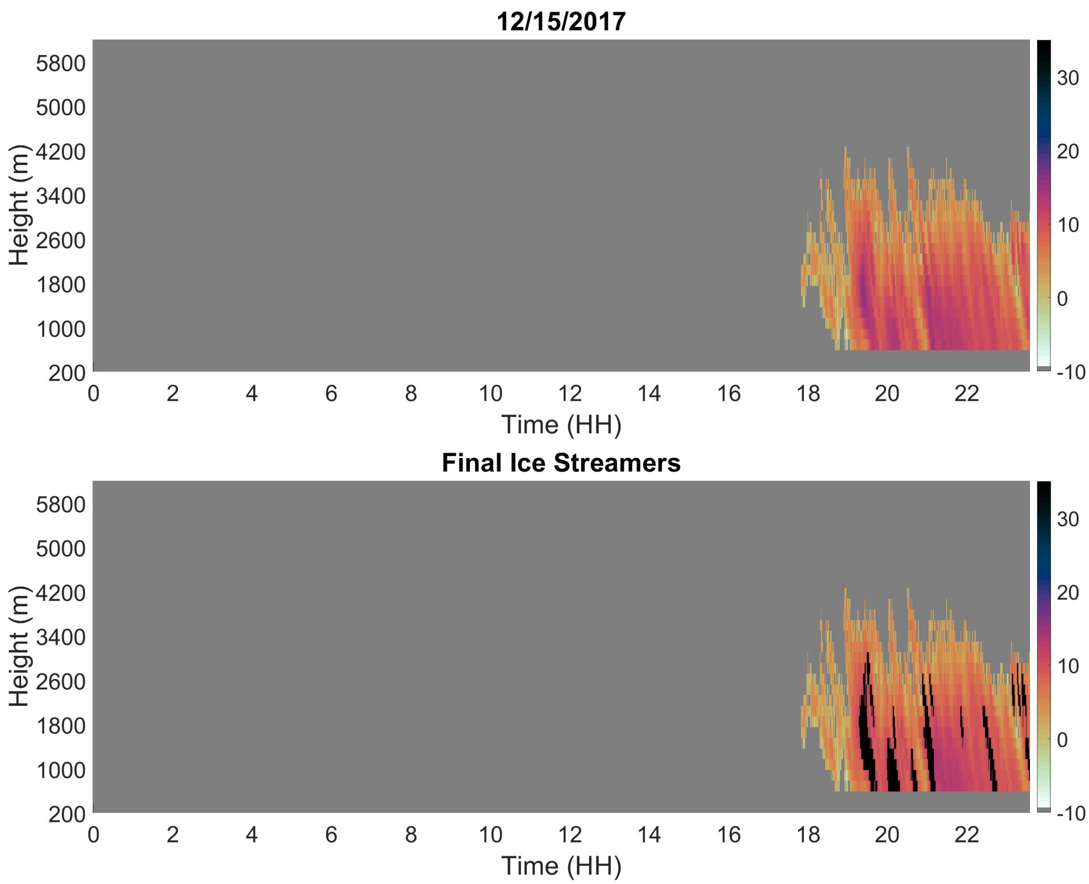

Figure A.14: Test case for ice streamer algorithm testing from a winter storm at Stony Brook, NY on 12/15/2017. (top) input radar reflectivity in dBZ, (bottom) reflectivity with identified ice streamers shown in black.

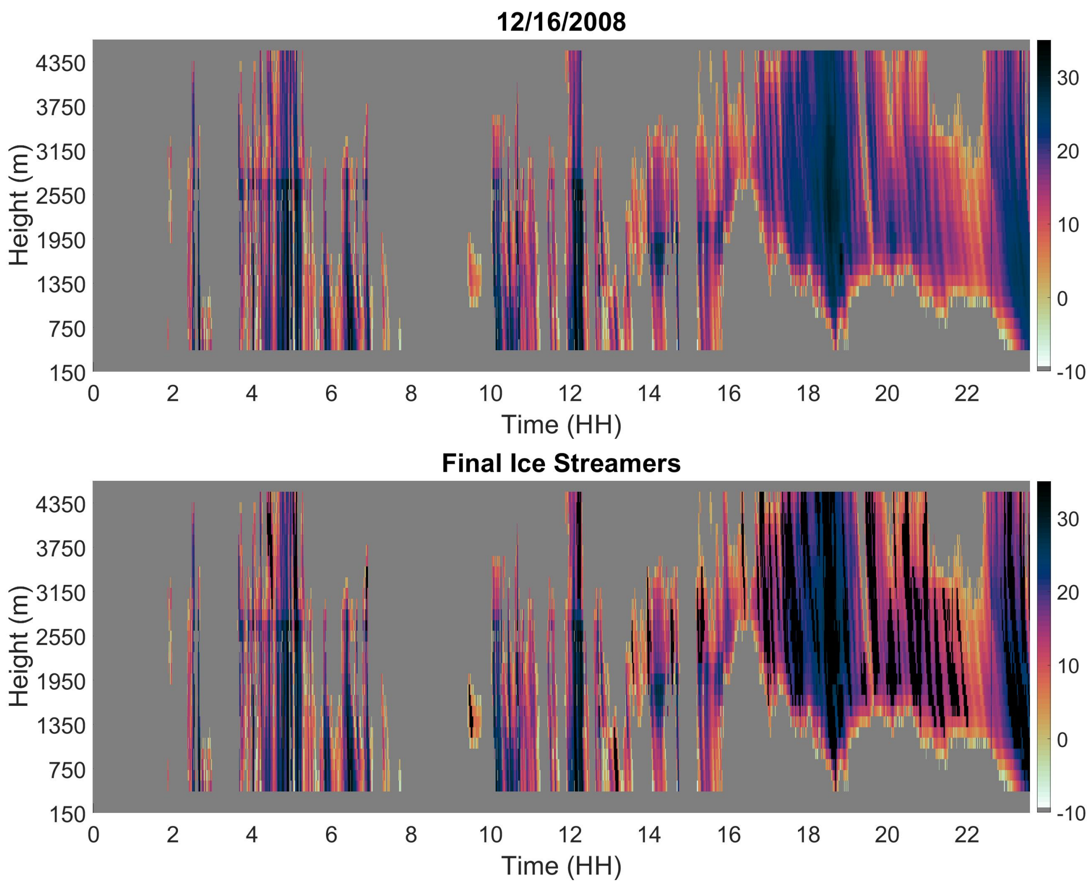

Figure A.15: Test case for ice streamer algorithm testing from a winter storm at Stony Brook, NY on 12/16/2008. (top) input radar reflectivity in dBZ, (bottom) reflectivity with identified ice streamers shown in black.

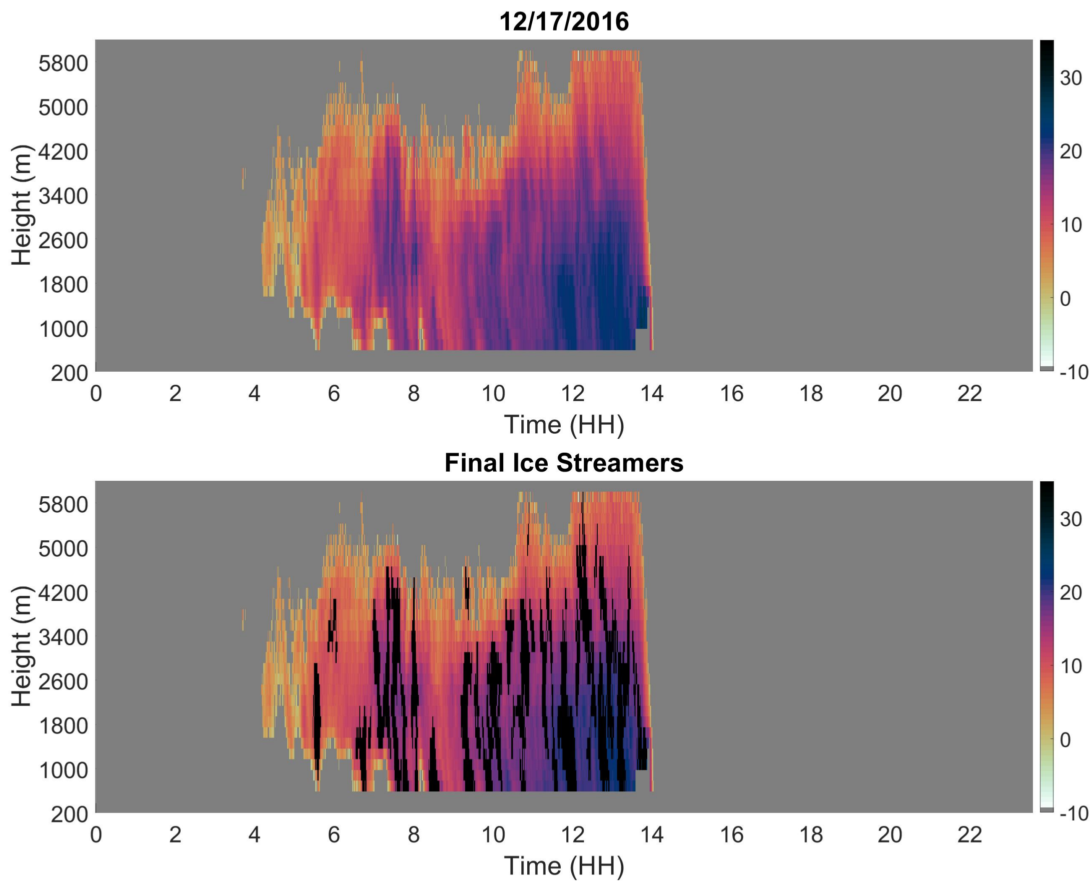

Figure A.16: Test case for ice streamer algorithm testing from a winter storm at Stony Brook, NY on 12/17/2016. (top) input radar reflectivity in dBZ, (bottom) reflectivity with identified ice streamers shown in black.

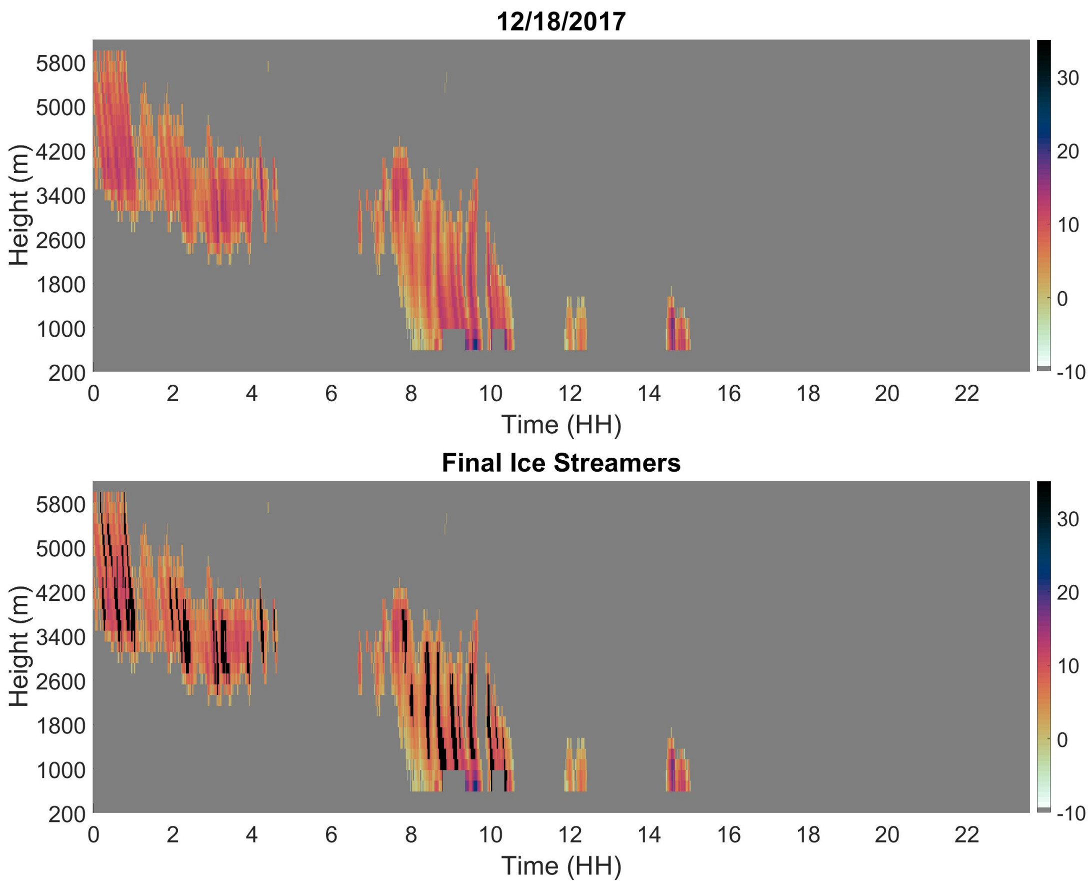

Figure A.17: Test case for ice streamer algorithm testing from a winter storm at Stony Brook, NY on 12/18/2017. (top) input radar reflectivity in dBZ, (bottom) reflectivity with identified ice streamers shown in black.

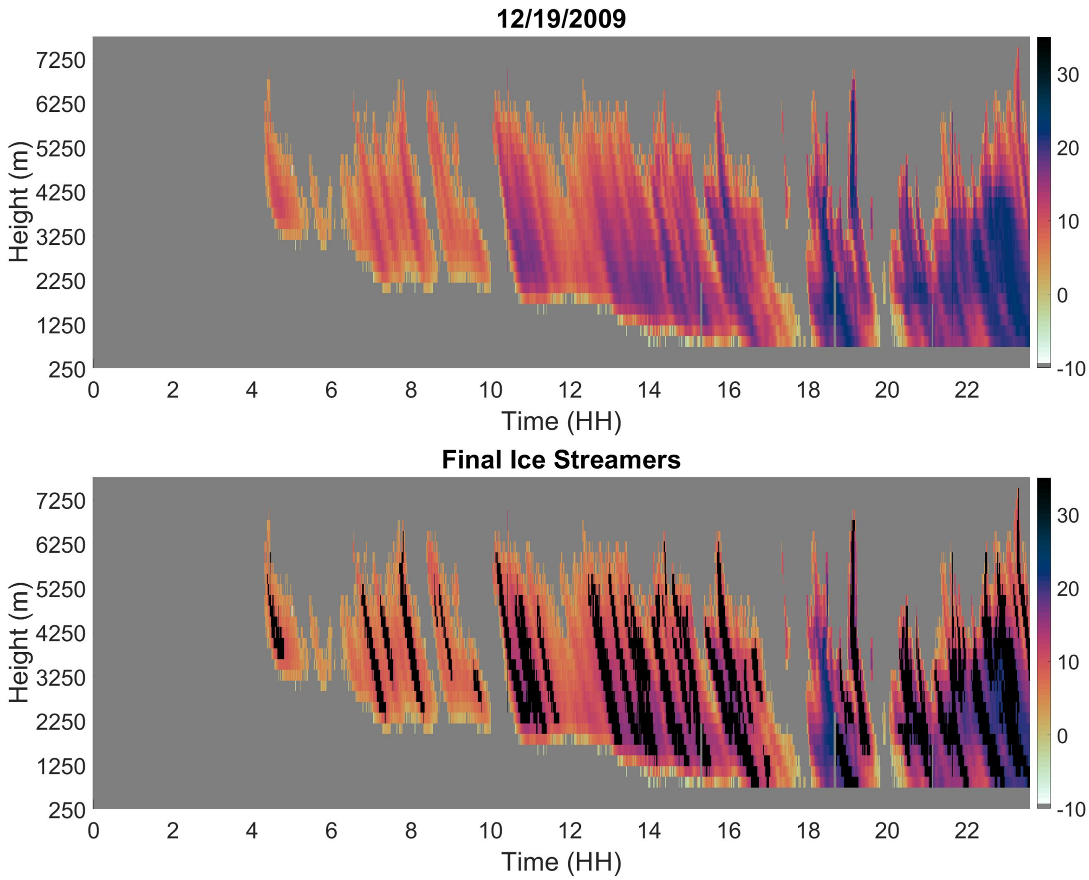

Figure A.18: Test case for ice streamer algorithm testing from a winter storm at Stony Brook, NY on 12/19/2009. (top) input radar reflectivity in dBZ, (bottom) reflectivity with identified ice streamers shown in black.

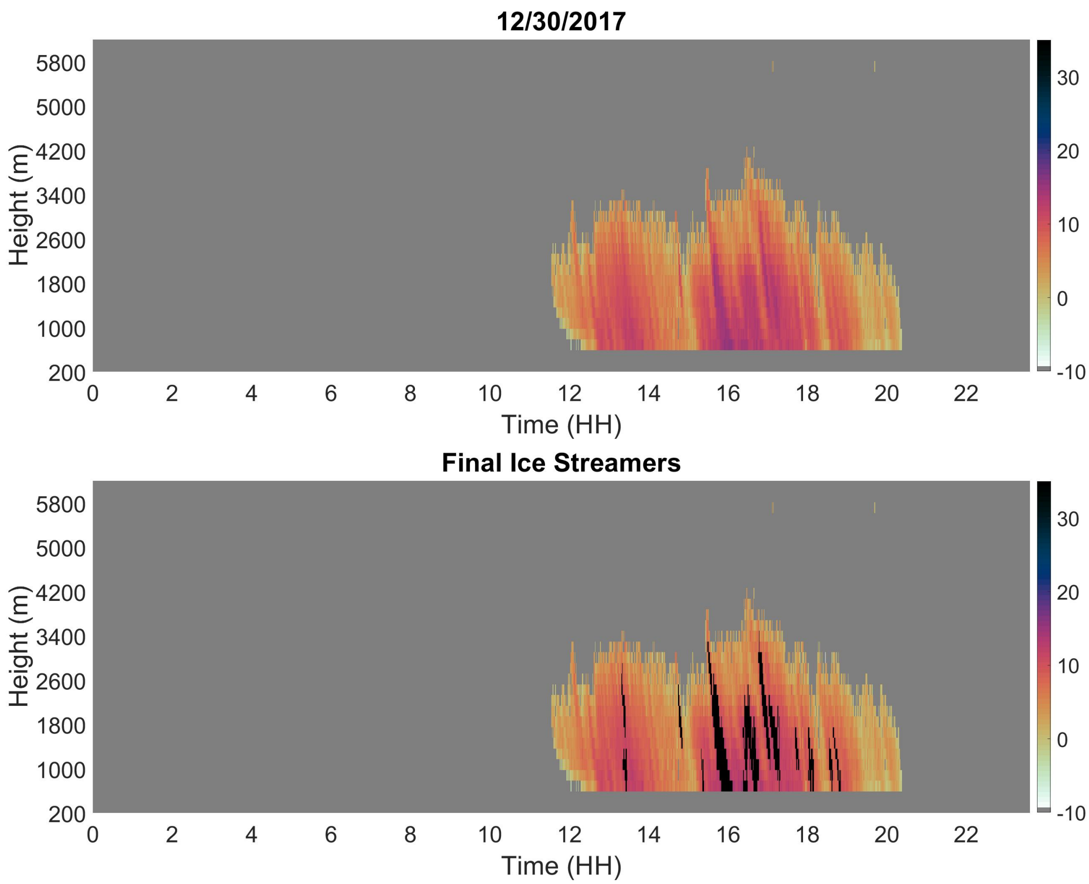

Figure A.19: Test case for ice streamer algorithm testing from a winter storm at Stony Brook, NY on 12/30/2017. (top) input radar reflectivity in dBZ, (bottom) reflectivity with identified ice streamers shown in black.

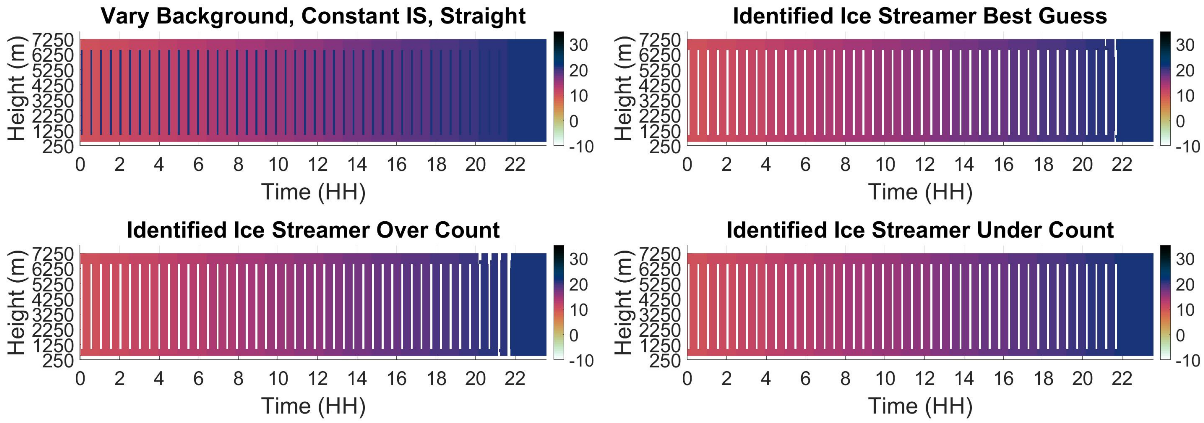

Figure A.20: Idealized example with a gradient in background reflectivity starting at 10 dBZ (left edge of each panel) and increasing by 0.25 dBZ every 30 min to a maximum value of 21.25 dBZ (22 UTC). The ice streamers all have a value of 21.25 dBZ. Identified ice streamers are shown in white. Ice streamer detection fails once the difference between the pixel and the background is less than 1 dBZ (for overcount) 0.75 dBZ (for best), and 0 dBZ (for undercount).

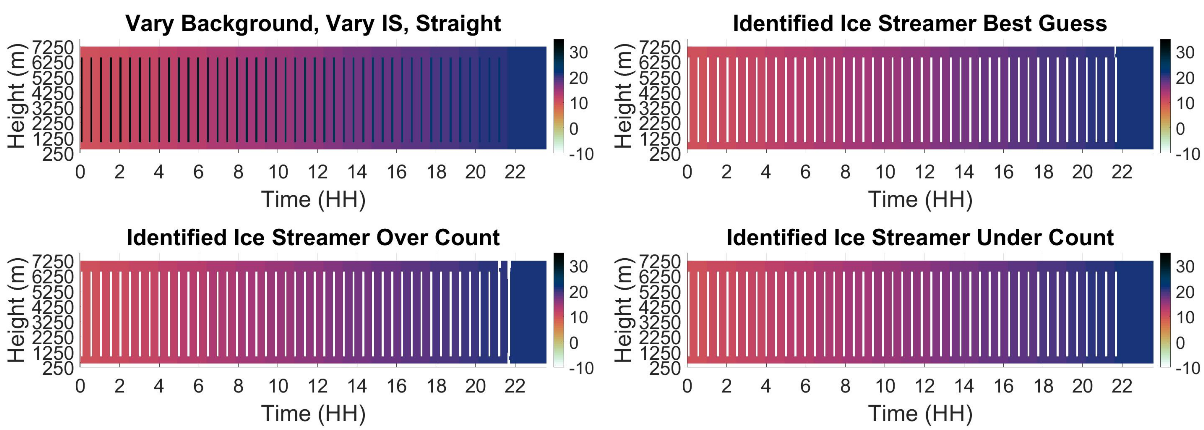

Figure A.21: Idealized case where both background and ice streamer values varied. Background dBZ started on left at 10 and increased 0.25 dB to a maximum value of 21.25 dBZ (2330 UTC). Identified ice streamers are shown in white. All ice streamer values began at 32.5 dBZ and decreased by 0.25 dB each ice streamer to a minimum value of 21 dBZ (2130 UTC)